QC
851
.B6
no.4

uary 1983
Colorado

U.S. DEPARTMENT OF COMMERCE
NOAA/ERL Wave Propagation Laboratory

STUDIES OF NOCTURNAL STABLE LAYERS AT BAO



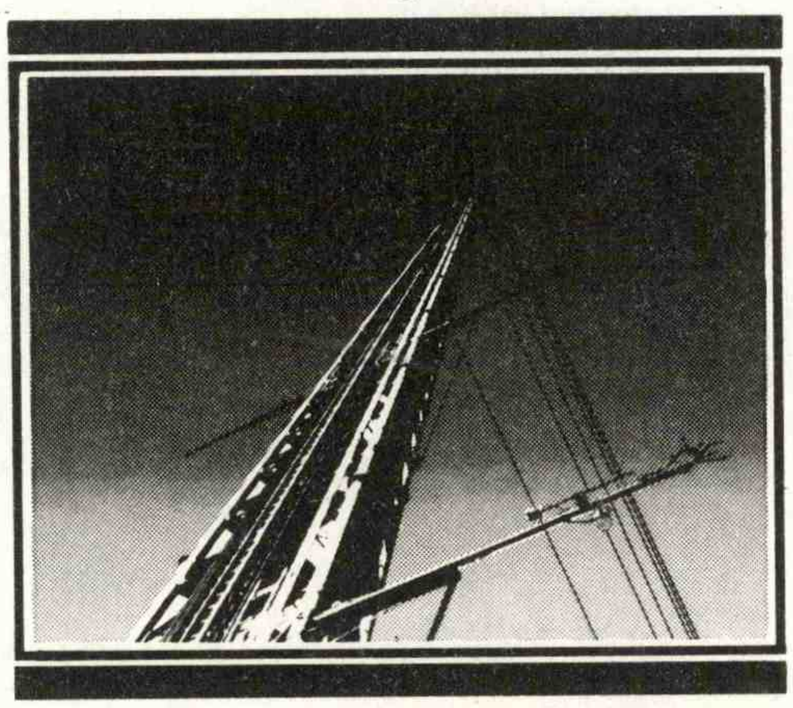
QC
851
.B6
no.4

STUDIES OF NOCTURNAL STABLE LAYERS AT BAO

J.C. Kaimal, Editor

LIBRARY
MAR 3 0 1990
N.O.A.A.
U.S. Dept. of Commerce

Report Number Four
January 1983



NOAA
Boulder Atmospheric Observatory

U.S. Department of Commerce
National Oceanic and Atmospheric Administration
Environmental Research Laboratories

A NOAA publication available from NOAA/ERL, Boulder, CO 80303.

NOTICE

Mention of a commercial company or product does not constitute an endorsement by NOAA Environmental Research Laboratories. Use for publicity or advertising purposes of information from this publication concerning proprietary products or the tests of such products is not authorized.

CONTENTS

Page

FOREWORD v

1. OBSERVATIONS OF TURBULENCE STRUCTURE IN STABLE LAYERS AT THE BOULDER ATMOSPHERIC OBSERVATORY (J.C.R. Hunt, J.C. Kaimal, J.E. Gaynor, and A. Korrell) 1

ABSTRACT 1
1.1 INTRODUCTION 2
1.2 TOPOGRAPHIC AND SYNOPTIC CONDITIONS OF THE EXPERIMENTS . . 3
1.3 MEAN WIND SPEED AND STRATIFICATION DATA 6
1.4 ANALYSIS OF VELOCITY AND TEMPERATURE FLUCTUATIONS AND HEAT FLUX IN TERMS OF WAVES AND/OR TURBULENCE 10
1.5 TENTATIVE CONCLUSIONS 23
1.6 ACKNOWLEDGMENTS 26
1.7 REFERENCES 26
APPENDIX A: BACKGROUND DATA FOR OBSERVATION PERIODS 30
APPENDIX B: VARIANCES AND SCALES OF TEMPERATURE AND VELOCITY FLUCTUATIONS IN THE STABLE BOUNDARY LAYER 41
APPENDIX C: SCALES OF TEMPERATURE AND VELOCITY FLUCTUATIONS . . 44
APPENDIX D: HYPOTHESES CONCERNING INTEGRAL SCALES AND DISSIPATION SCALES IN SLOWLY VARYING TURBULENT FLOWS 47

2. WAVE AND TURBULENCE STRUCTURE IN A DISTURBED NOCTURNAL INVERSION (Lu Nai-Ping, W.D. Neff, and J.C. Kaimal) 53

ABSTRACT 53
2.1 INTRODUCTION 53
2.2 SITE CHARACTERISTICS AND INSTRUMENTATION 54
2.3 GENERAL DESCRIPTION OF CASE STUDY 55
2.3.1 Meteorological Situation 55
2.3.2 Acoustic Sounder and Mean Flow Data 56
2.3.3 Internal Wave Behavior 60
2.4 SPECTRAL ANALYSIS 61
2.4.1 Spectra Under Steady Conditions 61
2.4.2 Disturbed Cases 62
2.5 INTERPRETATION 66
2.5.1 Effects at the Frontal Interface, 0100-0140 MST . . 66
2.5.2 Trends/Steps in the Data, 0420-0540 MST 68
2.5.3 Strong Disturbances in the Inversion, 0320-0440 MST 68
2.6 CONCLUSIONS 71
2.7 ACKNOWLEDGMENT 71
2.8 REFERENCES 72

3. A STUDY OF MULTIPLE STABLE LAYERS IN THE NOCTURNAL LOWER ATMOSPHERE (Li Xing-sheng, J.E. Gaynor, and J.C. Kaimal) 75

ABSTRACT 75
3.1 INTRODUCTION 75
3.2 FORMATION OF MULTIPLE LAYERS 76
3.3 A CASE STUDY 77
3.4 EDDY KINETIC ENERGY AND THE DISTRIBUTION OF TURBULENT FLUXES OF HEAT AND MOMENTUM 82
3.5 TEMPERATURE BUDGET PROFILE 85
3.6 CONCLUSIONS 89
3.7 ACKNOWLEDGMENTS 89
3.8 REFERENCES 90

4. A METHOD FOR MEASURING THE PHASE SPEED AND AZIMUTH OF GRAVITY WAVES IN THE BOUNDARY LAYER USING AN OPTICAL TRIANGLE (Li Xing-sheng, Lu Nai-ping, J.E. Gaynor, and J.C. Kaimal) . . . 93

ABSTRACT 93
4.1 INTRODUCTION 93
4.2 MEASUREMENTS AND COMPUTATIONS 94
4.3 RESULTS 99
4.4 CONCLUSIONS 105
4.5 ACKNOWLEDGMENTS 106
4.6 REFERENCES 106

5. RICHARDSON NUMBER COMPUTATIONS IN THE PLANETARY BOUNDARY LAYER (R.J. Zamora) 109

ABSTRACT 109
5.1 INTRODUCTION 109
5.2 GOVERNING EQUATIONS 111
5.2.1 Dry Atmosphere 111
5.2.2 Moist Atmosphere 112
5.3 COMPUTATIONAL SCHEME 114
5.3.1 Instrumentation and Calibration 114
5.3.2 The Algorithm 116
5.4 ERROR ANALYSIS 117
5.5 ANALYSIS 117
5.6 CONCLUSIONS 127
5.7 ACKNOWLEDGMENTS 128
5.8 REFERENCES 128

FOREWORD

This report, the fourth in the Boulder Atmospheric Observatory (BAO) series, brings together in one volume five studies of the nocturnal stable layer. The work was conducted in the Wave Propagation Laboratory during 1981 and 1982. Impetus for the first four of these studies came from visiting scientists who found in data collected at BAO a unique source of information on mean and turbulent characteristics of stable layers. The structure of turbulence in nocturnal stable layers, unlike that of daytime convective boundary layers, cannot be described in simple universal terms. Stable layers are almost always in a state of evolution. At BAO, the problem is even more challenging because of the rolling terrain, the drainage flow from the Rocky Mountains, and the frequent presence of gravity waves and elevated inversion layers. To the scientist eager to unravel these complexities, the BAO records offer conditions of unending variety. Each paper in this report explores a different aspect of the nocturnal stable layer. It is our hope that this collected work will stimulate comments from other workers in the field and lead to new insights into the structure of the stable atmosphere.

J.C. Kaimal, Editor
Atmospheric Studies Program Area
Wave Propagation Laboratory

1. OBSERVATIONS OF TURBULENCE STRUCTURE IN STABLE LAYERS AT THE BOULDER ATMOSPHERIC OBSERVATORY

J.C.R. Hunt
Department of Applied Mathematics
and Theoretical Physics
University of Cambridge
Cambridge CB39EW, United Kingdom

J.C. Kaimal, J.E. Gaynor, and A. Korrell
NOAA/ERL/Wave Propagation Laboratory
Boulder, Colorado 80303

ABSTRACT. Three days of measurements in stable conditions (Monin-Obukhov length L between 15 and 300 m) at the Boulder Atmospheric Observatory (BAO) tower are presented. Winds came off the Rocky Mountains on 2 days and off the plains on the other day. Vertical profiles of the mean horizontal velocity U, and the Brunt-Väisälä frequency N, and of the variances, fluxes, spectra, cospectra, quadspectra, and correlations are examined in this study. New theoretical arguments are developed for relating variances to scales of temperature θ and vertical velocity w fluctuations and to scales of heat and momentum fluxes in the stable boundary layer. Some tentative conclusions drawn from this study are the following:

(1) In terrain, even gently rolling as it is at BAO (slopes <7%), the profiles of dU/dz and $d\bar{\theta}/dz$ are significantly different from those over level ground. For example, in stable conditions, $z(dU/dz)$ and $z(d\bar{\theta}/dz)$ often do not increase with height z.

(2) The presence of coherent wave motions cannot be detected from U and $\bar{\theta}$ profiles. The most sensitive tests are $w\theta$ cospectra and quadspectra.

(3) Wave motions may be apparent only in the θ spectra (moderate wave conditions) or may be apparent in both w and θ spectra (strong wave conditions). Typical inertial subrange spectra are found in all cases.

(4) Whether or not waves are present, a theoretical prediction for local parameterization of temperature fluctuation σ_θ and heat flux $\overline{w\theta}$ based on σ_w, N, and $d\bar{\theta}/dz$ appears to order the data fairly well where strong uniform density gradients exist. In particular we find the dimensionless temperature fluctuation parameter $\zeta_\theta \simeq 0.8 \pm 0.25$ and thermal diffusivity parameter $F \simeq 0.2 \pm 0.1$.

(5) In the boundary layer, where $dU/dz > N$, the integral scale of the w component $L_x^{(w)}$ is found to agree (within about 50%) with the theoretical formula,

$$[L_x^{(w)}]^{-1} \simeq 0.7\ (dU/dz)/\sigma_w + z^{-1}.$$

(6) The large values of the cospectra of w and θ at low frequencies show that wavelike motions can transfer significant quantities of heat (or pollutant). This is probably due to small-scale mixing on a time scale of about $5\ N^{-1}$ accompanying the wave-induced, large-scale motions across the temperature gradient.

1.1 INTRODUCTION

The general aim of this paper is to present some interesting measurements, taken on the Boulder Atmospheric Observatory (BAO) 300-m tower, of the mean and fluctuating velocity and temperature in stably stratified atmospheric air flows within 300 m of the ground. This depth may or may not exceed the depth of the stable boundary layer. From the analysis of these measurements, a number of general features of these flows can be discerned; we particularly emphasize those features that are of practical importance for estimating flow and diffusion in stable conditions, both over level ground and in hilly terrain, and those features of the flow that are affected by the terrain at BAO. The BAO tower is situated in rolling terrain 30 km from the foothills of the Rocky Mountains. It is of interest to know what features of the flow are similar to those measured over the flat terrain at Kansas, Minnesota, and St. Louis, Mo. The results presented here are not chosen with the view to study the development of the boundary layer; rather we concentrate on the structure of these flows averaged over periods on the order of 20 or 60 min.

The measurements bring out some interesting features of the large-scale turbulence in and above the stable boundary layer (SBL). In the upper part of the SBL, in all kinds of terrain, there appears to be a significant amount of energy in internal wave motion mixed in with the turbulence. By use of various statistical analyses we attempt to identify these various kinds of fluctuations, to estimate the relative energies in these fluctuations, and to find out their relative contributions to the heat fluxes and to the destruction of turbulent energy by buoyancy flux and by viscous dissipation.

More than in convectively unstable or neutral flows, the dynamics of a stably stratified turbulent flow depend on the rate at which fluid elements mix with each other and change their density. If there is no such mixing, the vertical displacements of fluid elements are constrained by the amount of energy in the turbulence to lie within a distance on the order of σ_w/N of their equilibrium static height, where σ_w is the standard deviation of vertical velocity and N is the Brunt-Väisälä frequency (Pearson et al., 1983; Pearson and Britter, 1980). By measuring the vertical velocity distribution and spectra, the temperature fluctuations, and the heat flux, and by making use of the Lagrangian model of Csanady (1964) and Pearson et al., we can learn a good deal about the particle displacements and mixing. We are interested in knowing to what extent internal wave motion affects these relations. From these measurements, predictions (by means of the Lagrangian model) for vertical diffusion of plumes can be made, which we hope to test later in the forthcoming BAO diffusion experiments.

Another aspect of the turbulence structure we measure and analyze here is the effect of stable stratification on the length scales of velocity and temperature. Using an analysis (unpublished but summarized in Appendix B) based on the turbulence kinetic equation, we examine the main effects of stable stratification on the turbulence in the lower part of the boundary. Since the length scales affect the dissipation of turbulent energy and the destruction of temperature variance, there are some important dynamical and modeling consequences from our findings. Inter alia, we show that, in the lower part of the stable boundary layer, the main effect of an increase in stable stratification on the turbulent energy is not so much the loss of kinetic energy by the buoyancy flux (the usual explanation) as the larger (by a factor of 4) increase of viscous dissipation caused by the reduction in length scale associated with the increased mean velocity gradient.

1.2 TOPOGRAPHIC AND SYNOPTIC CONDITIONS OF THE EXPERIMENTS

The measurements were made on the BAO tower about 30 km east of the foothills, and about 60 km from the Continental Divide of the Rocky Mountains, where the mountains are at an effective height H ($\simeq 1.5 \times 10^3$ m) above the ground level at BAO. In stable conditions, unlike unstable conditions, the

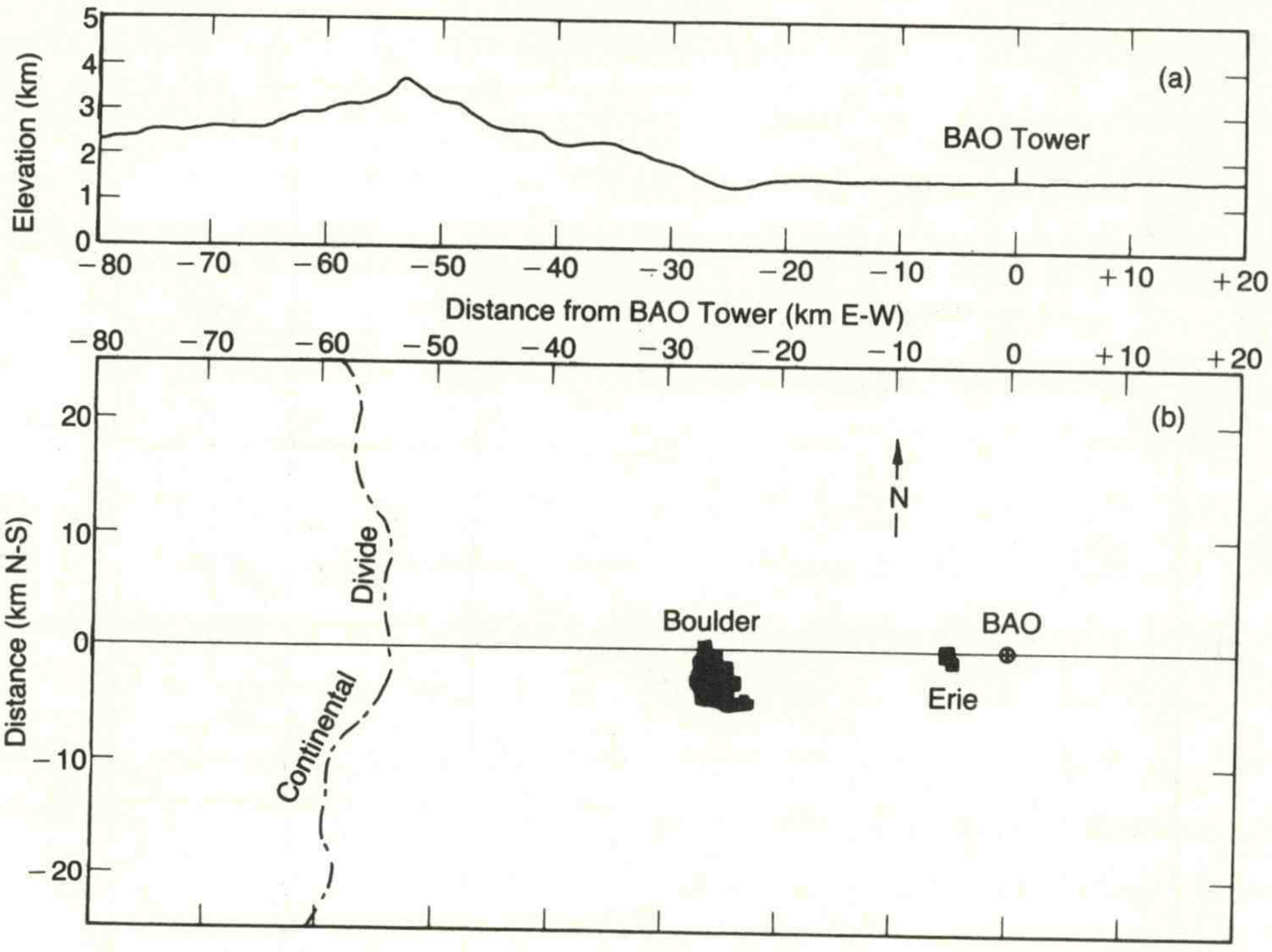


Figure 1.1.--Topography of the BAO site and surroundings: (a) E-W section through the BAO site; (b) map showing the location of BAO with respect to the Continental Divide.

effects of large hills can affect the flow many kilometers downwind or upwind; also, the flow over the local topography (where slopes are at most of order 7%) has to be considered more carefully (Kaimal et al., 1982). Details of the topography are given in Figs. 1.1 and 1.2.

Surface weather maps and rawinsonde plots bracketing the observation periods on 18 April 1978, 22 April 1978, and 15 April 1980, and upper-air soundings at Denver (30 km from BAO) are given in Appendix A.

On the second and third days analyzed, 22 April 1978 and 15 April 1980, the general air flow over 300 km around the site, and the local air flow, were from the west to northwest and were therefore coming from the mountains. The tower is at a distance of about 30 to 40 times H from the mountains.

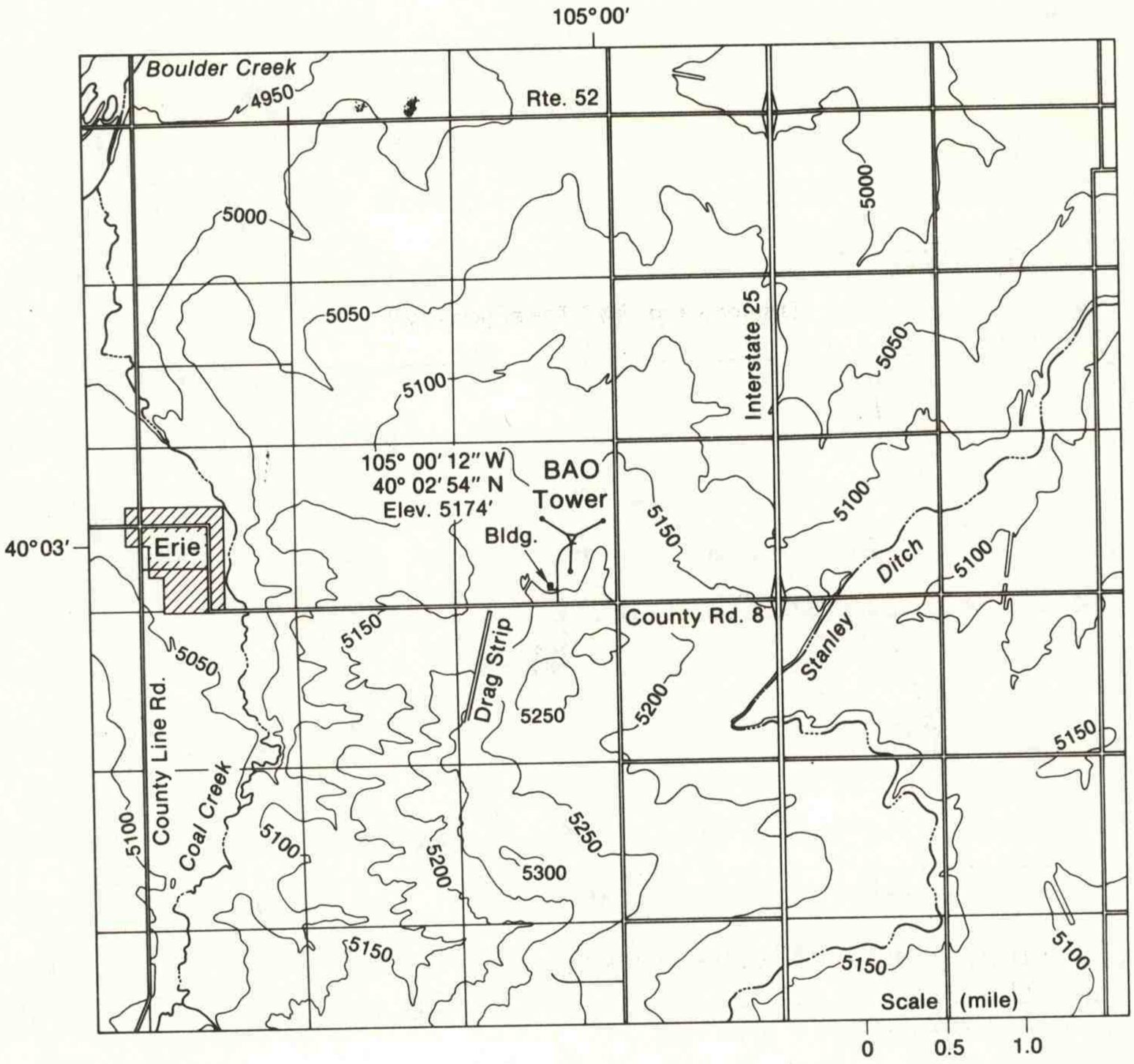


Figure 1.2.--A conventional contour map of the immediate BAO terrain (elevation in feet).

Laboratory experiments (e.g., Hunt and Snyder, 1980), calculations (e.g., Klemp and Lilly, 1975), and aircraft measurements show that the effects of the Rockies on the wind extend at least as far as this in stable conditions. So on these days we expect the air flow at BAO to have characteristics quite different from that over a plain, whereas in the unstable conditions measured by Kaimal et al. (1982) such winds behaved much as they did over the plains of Kansas or Minnesota. [It would be interesting to analyze the upper-air soundings given in Appendix A to see if and what kinds of internal gravity waves are expected; perhaps calculations such as those performed by Einaudi and Finnigan (1981) might be possible.]

1.3 MEAN WIND SPEED AND STRATIFICATION DATA

Figure 1.3 shows the vertical profiles of the mean horizontal velocity U and direction A, and the mean potential temperature gradient $d\bar{\theta}/dz$ calculated in the form of the Brunt-Väisälä frequency $N = [g(d\bar{\theta}/dz)/T_o]^{1/2}$, where T_o is the ground-level temperature and g is the acceleration due to gravity. On the first day of measurements, 18 April 1978, the wind came from between north and northeast both locally and generally. The only reason in this case to expect results different from those over a plain is because of the local terrain around the tower, which, as we shall show, is sufficiently sloping to have a measurable effect in stable conditions. On 22 April 1978 and 15 April 1980 the wind came off the mountains. (Numerical values of U and other mean and fluctuating velocity and temperature data are presented in Appendix A.)

A striking feature of the profiles of U is how only in the third case, where there was a collapsing daytime mixed layer, is the mean velocity shear dU/dz effectively confined to about 200 m. In the second case, in the middle of the night with a strong wind, there is appreciable shear all the way up to 300 m. (The value of L, the Monin-Obukhov length, is about the same at 1700 MST on the first day as between 0006 and 0436 MST on the second day). In the first case considered here, 18 April 1978, the shear is significant at the top of the tower. Only the profiles on 15 April 1980 are similar to the Minnesota profiles measured by Caughey et al. (1979), where dU/dz was usually negligible above about 100 m in strongly stable conditions.

The upper-air soundings at 1700 on 18 April and at 0500 on 19 April 1978 were too different to infer the conditions at 2100 to 2300. On 22 April 1978 there was also little change in the wind's direction or strength, but the value of N varied with height z: $N \simeq 0.007$ rad/s for $z < 0.8$ km; 0.001 rad/s for 0.8 km $< z <$ 1.5 km; and 0.037 rad/s for 1.5 km $< z <$ 3 km. On 15 April 1980 the soundings show that the direction and strength of the wind and the value of N did not change significantly up to about 4 km above the ground.

To what extent are the tower profiles affected by the local terrain when the winds are from the west, given a local upslope of about 2% to the west of the tower? The effect of a slope on U(z) depends on the shear in the approach

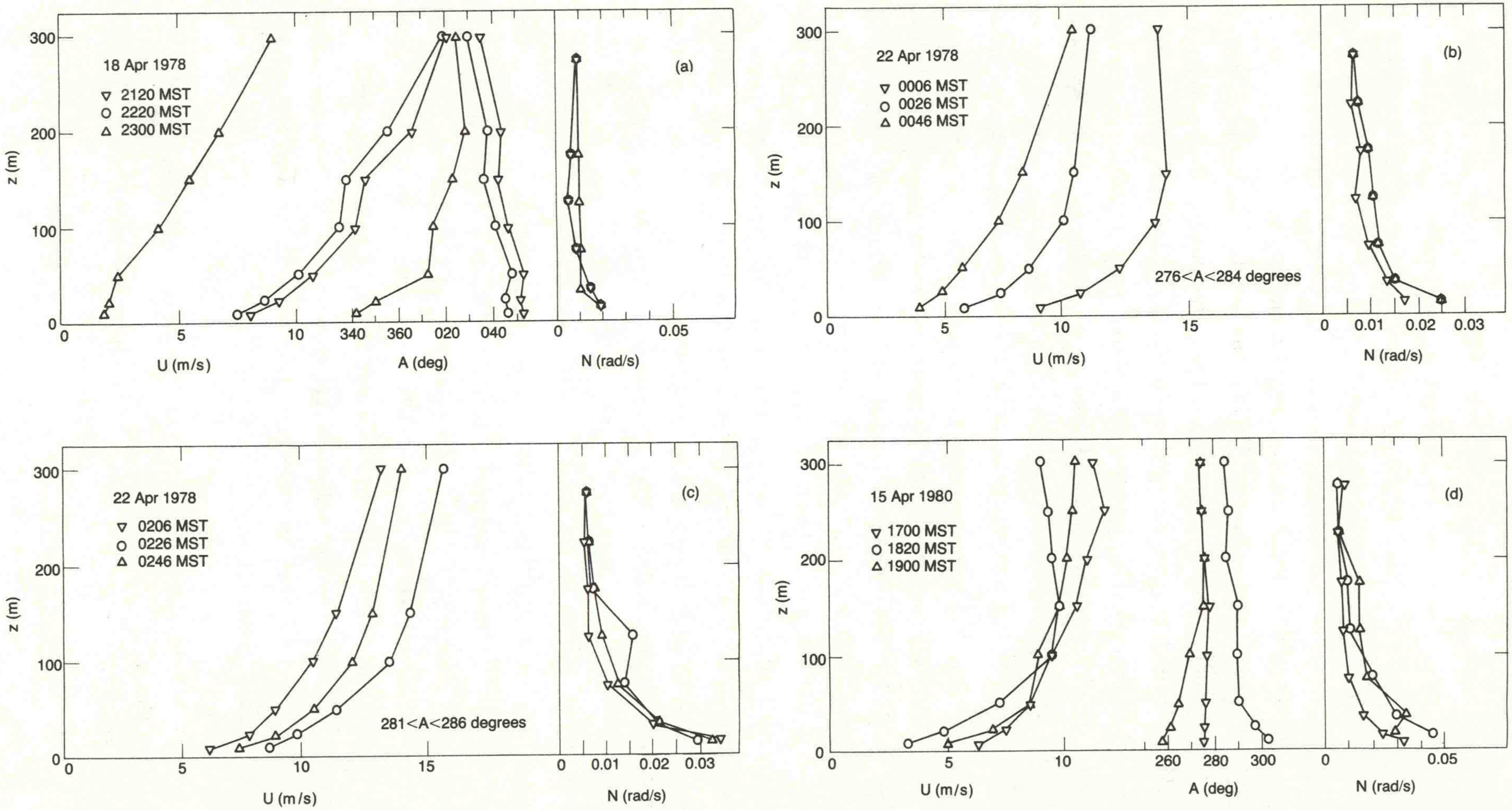


Figure 1.3.--Horizontal wind speed (U), wind direction (A), and buoyancy frequency (N) profiles based on 20-min averages: (a) 18 April 1978; (b) and (c) 22 April 1978; (d) 15 April 1980.

flow. In stable conditions the value of the velocity shear in the approach flow is far greater than its value in neutral conditions. Calculations and wind tunnel studies indicate that U(300)/U(10) is typically 50% greater in stable conditions than in neutral ones (Hunt, 1981). This can increase the local normalized speedup of the mean wind speed $\Delta U/U$ by a factor of 2 or more. One might expect $\Delta U/U(10\ m)$ to be about $0.02\ [U(300)/U(10)]^2 \simeq 0.2$. The dynamical effects of the density gradient on the flow over this slope are not large since $U(300)/[N(300) \times L_1] \gtrsim 1$ (Hunt, 1981). L_1 is the half-length of the equivalent hill (≃800 m in this case). This increase in the speedup reduces the shear over a hill or slope and perhaps explains why on 18 and 22 April 1978 $z(dU/dz)$ increases more slowly with z than is observed on level ground. The plot of $kz(dU/dz)/u_*$ as a function of z/L in Fig. 1.4a shows an increase with z, as is found over level ground, but with a smaller coefficient: $\alpha = 3.2$ rather than 5. Here k is the von Kármán's constant and u_* is the surface friction velocity. Our measurements of $z(d\overline{\theta}/dz)$ do not increase with height, unlike the measurements over level ground (Kaimal, 1973).

An important parameter for the calculation of air flow over hills is the Scorer (1949) parameter $\ell_s^{-2} = [(N/U)^2 - (d^2U/dz^2)/U]$. In many calculations it is assumed that in stable conditions ℓ_s is largely determined by (N/U) for $z > h$, h being the thickness of the stable surface layer (e.g., Smith, 1980).

The calculations of $(N/U)^2$ and $(-d^2U/dz^2)/U$ are plotted in Fig. 1.4b and show that, for the 3 days considered here, the mean velocity curvature largely determines ℓ_s for $z \lesssim 300$ m. Consequently in rolling or hilly terrain, when calculations are to be made of air flow over a specific hill or over a limited region of hills, the effects of the incident shear profile may well be as important as the dynamical effects of the stable stratification. The curvature may extend farther up into the boundary layer in stable conditions than in neutral conditions.

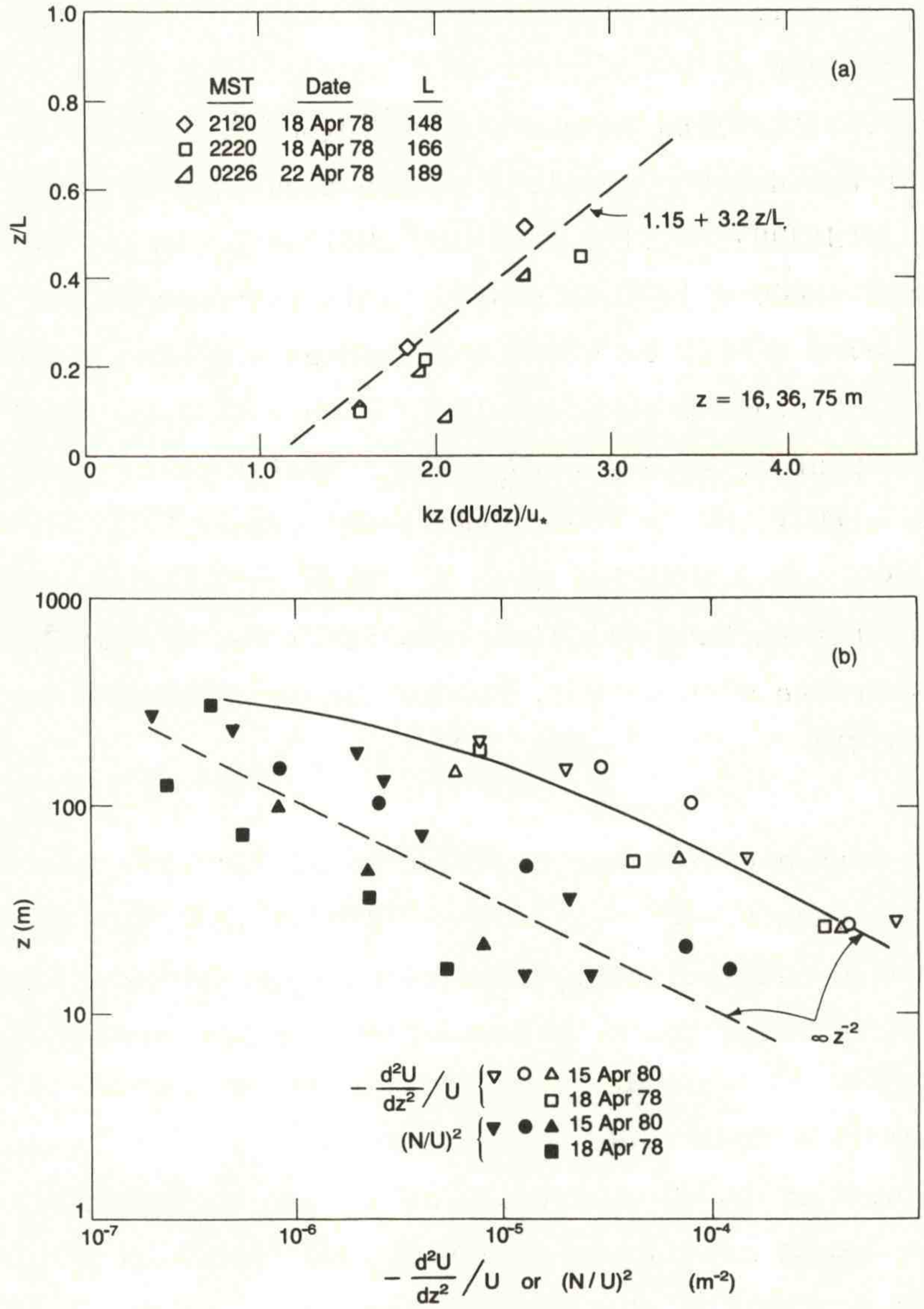


Figure 1.4.--Analysis of mean velocity and density profiles: (a) comparison of the dimensionless velocity gradient with the Monin-Obukhov similarity law for 18 April 1978 ($k = 0.4$ is assumed); (b) comparison of the profile curvature term $(-d^2U/dz^2)/U$ term with $(N/U)^2$.

1.4 ANALYSIS OF VELOCITY AND TEMPERATURE FLUCTUATIONS AND HEAT FLUX IN TERMS OF WAVES AND/OR TURBULENCE

A cursory look at Figs. 1.5-1.8 shows that the fluctuations in vertical velocity and temperature exhibit waves as well as turbulence, waves being defined in the sense of regular oscillations. (Since these were tower measurements, we could not make a more decisive test of waves by distinguishing whether these oscillations were or were not propagating relative to the mean flow.) On the days chosen here for analysis, varying amounts of wave motion relative to the turbulence are observed; the wave conditions are weak, moderate, or strong on these occasions, and are classified accordingly.

In Fig. 1.5a, vertical velocity w and temperature θ fluctuations at 10 and 150 m are plotted as functions of time for 22 April 1978. Note the strong strong wavelike behavior in w at 150 m. By contrast, in Fig. 1.5b the traces for 15 April 1980 show weak wavelike behavior. The waves are certainly organized, but their amplitude is weak.

In Figs. 1.6a,b the spectra of w and θ--$nS_w(n)$ and $nS_\theta(n)$--and the cospectra and quadspectra of $w\theta$--$nC_{w\theta}(n)$ and $nQ_{w\theta}(n)$--are plotted for the turbulence on 18 April 1978. Note that there appear to be concentrations of energy at discrete frequencies in all these spectra, a fact that can be tested by looking for discrete frequencies in autocorrelation functions. There is a much greater contribution by these wavelike fluctuations to the temperature than to the velocity spectra. The object of plotting both the cospectra and the quadspectra is to show how much heat flux is actually transferred by the low-frequency, wavelike motions. For a nearly pure sine wave with no mixing in a temperature gradient, the cospectra would be very small compared with the quadspectra. In Figs. 1.6a,b we observe that, compared with the velocity spectra, a significant portion of the heat flux is transferred by the low-frequency, wavelike motions, because $C_{w\theta}(n)$ is of the same order as $Q_{w\theta}(n)$. It is also observed that, at the frequencies where the $\overline{\theta^2}$ "energy" is large* and $S_\theta(n)$ is near its maximum, $Q_{w\theta}(n)$ has the form of a double "spike" as it rapidly swings from one sign to the other over a

---

* The drift in $\bar{\theta}$ produces about 10% of the variance.

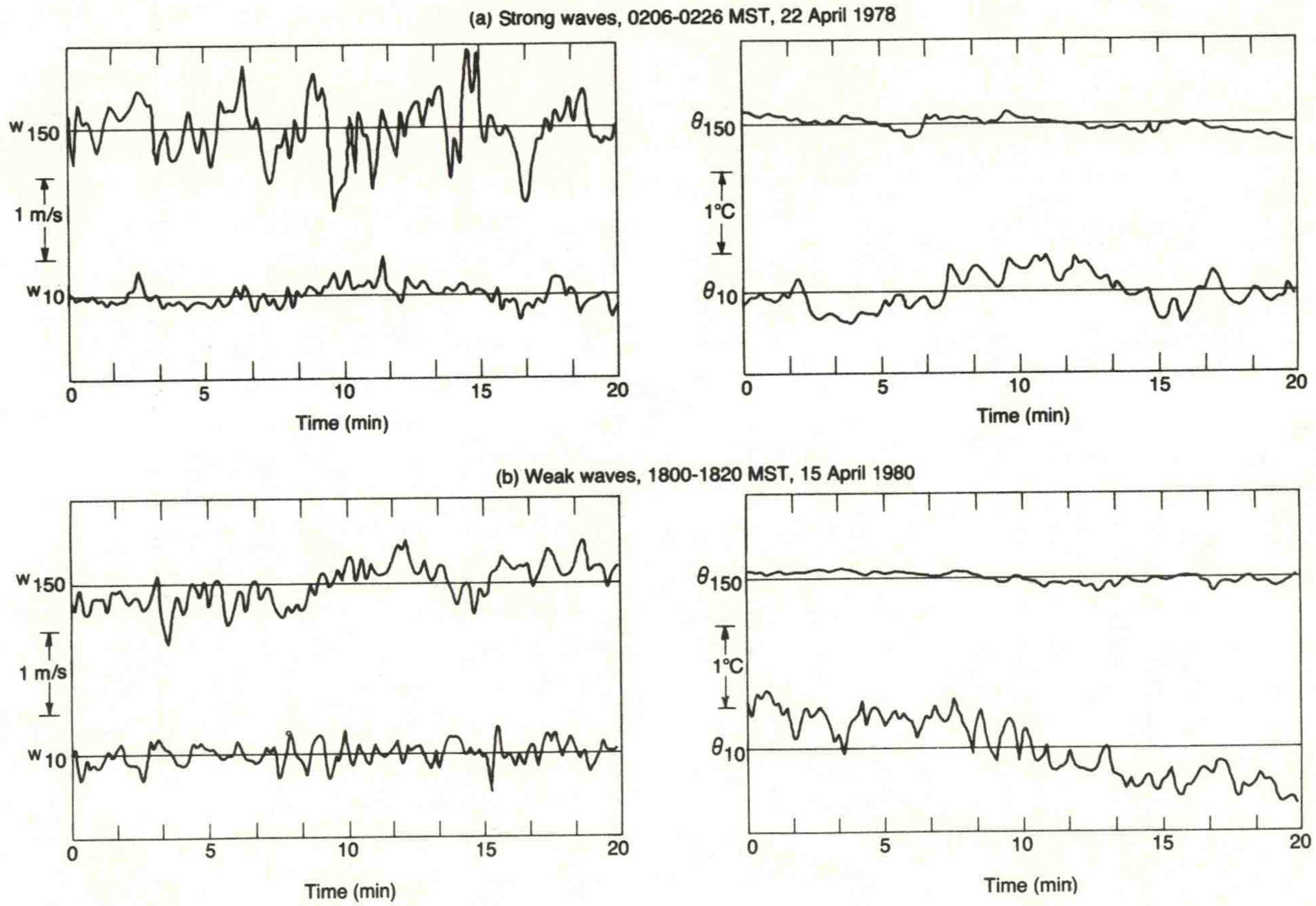
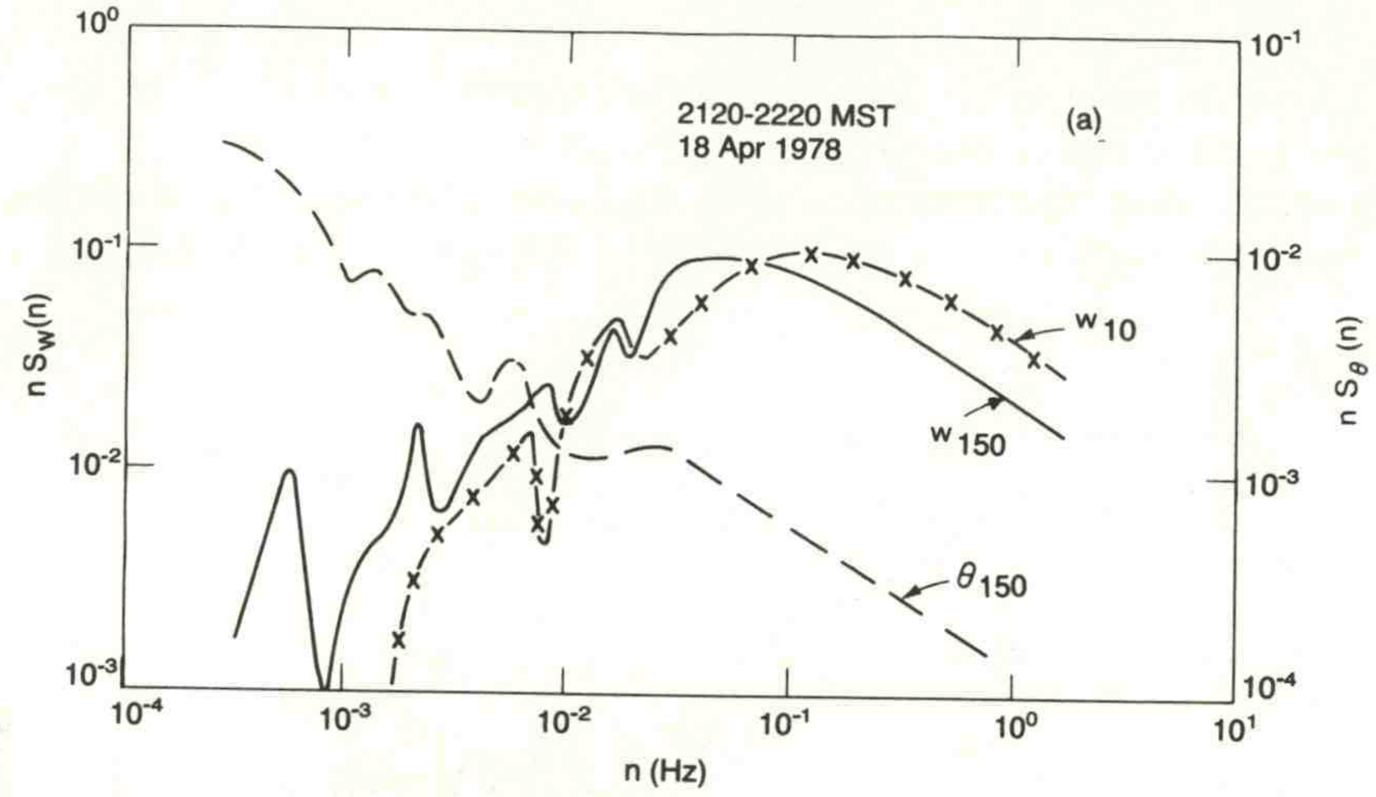
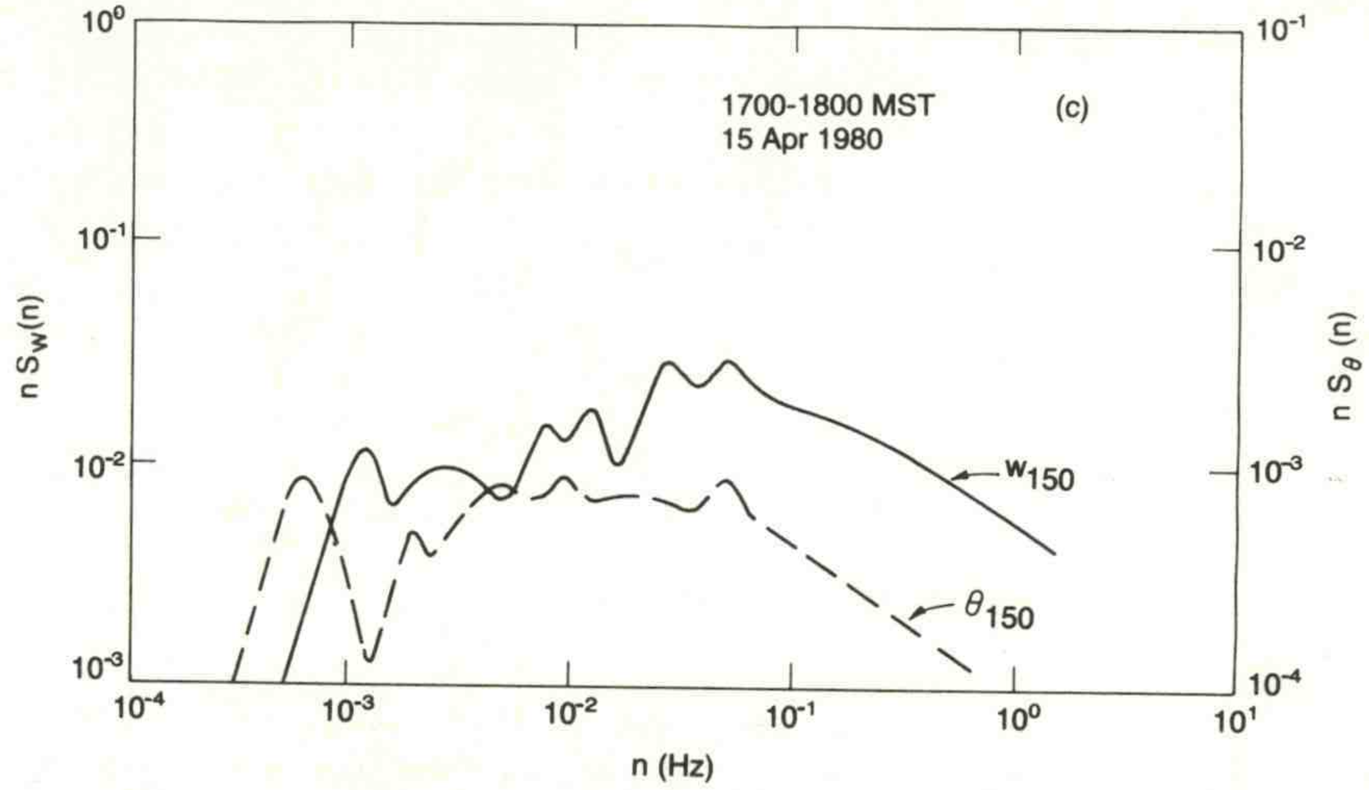
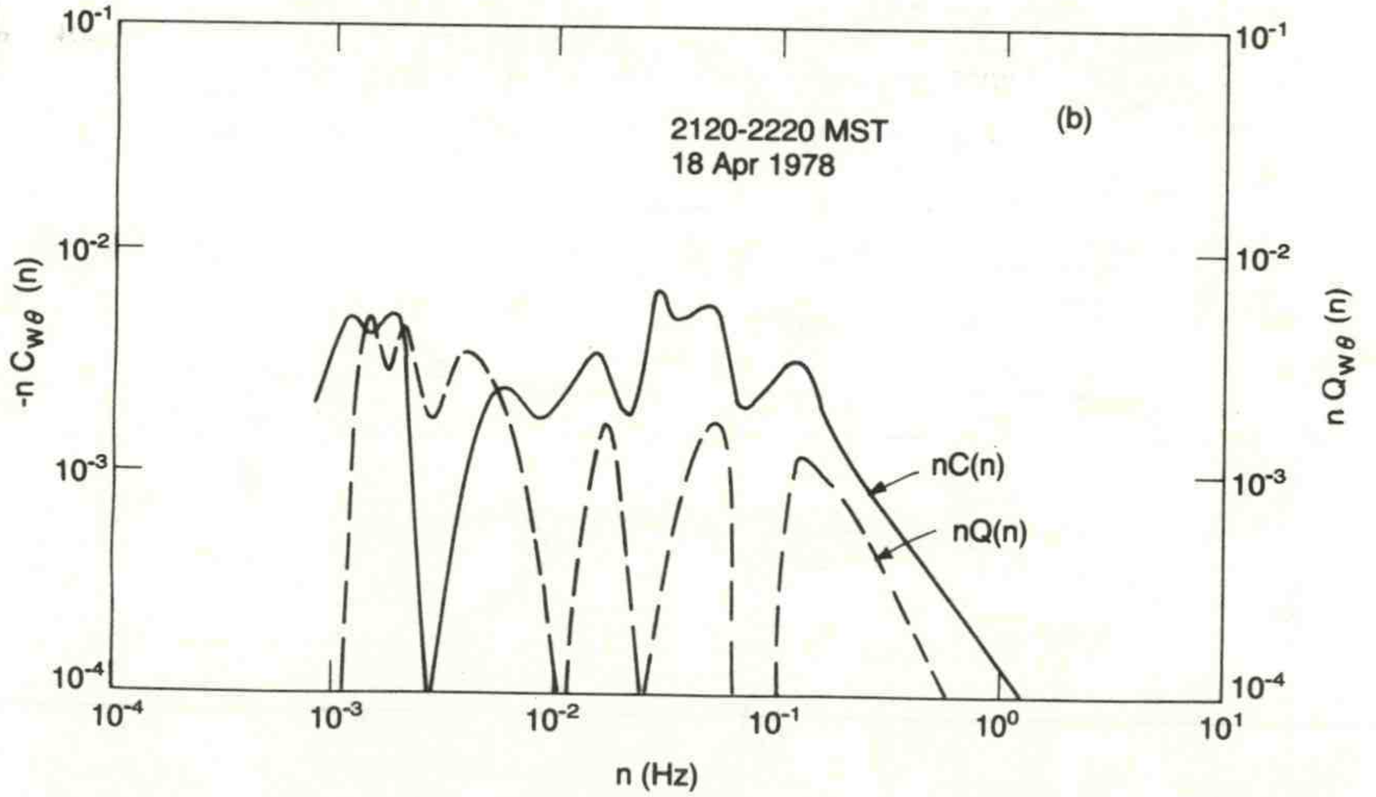


Figure 1.5.--Typical time series for strong and weak wave conditions: (a) w and θ fluctuations at 10 and 150 m for 22 April 1978; (b) w and θ fluctuations at 10 and 150 m for 15 April 1980.







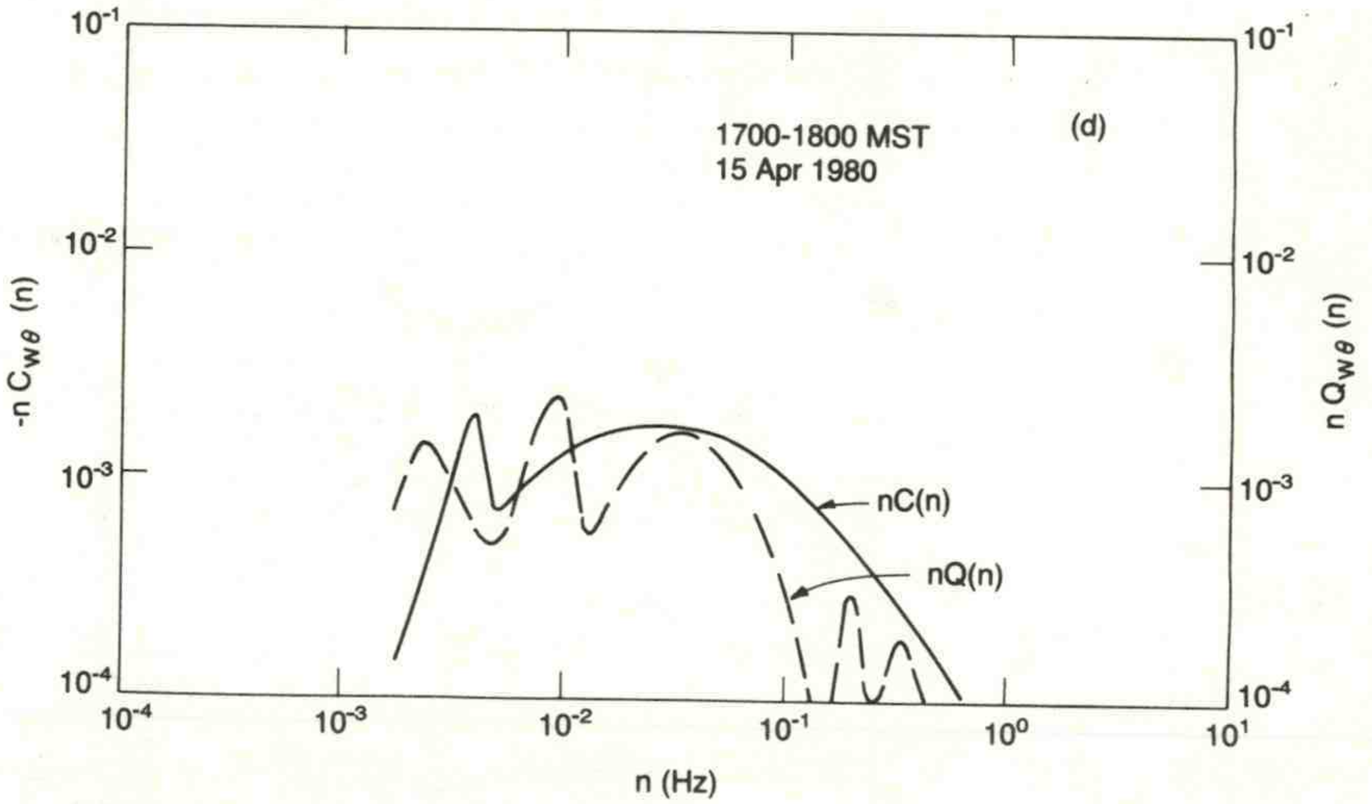
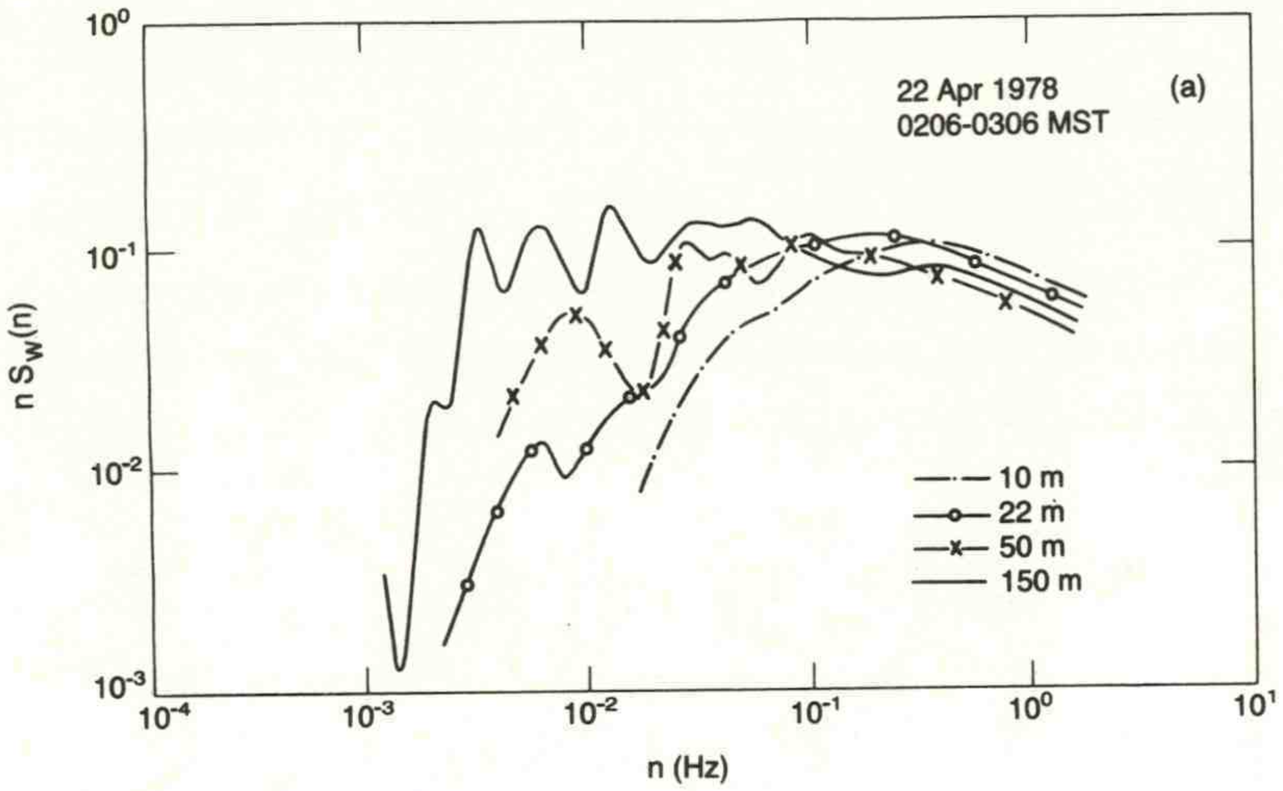
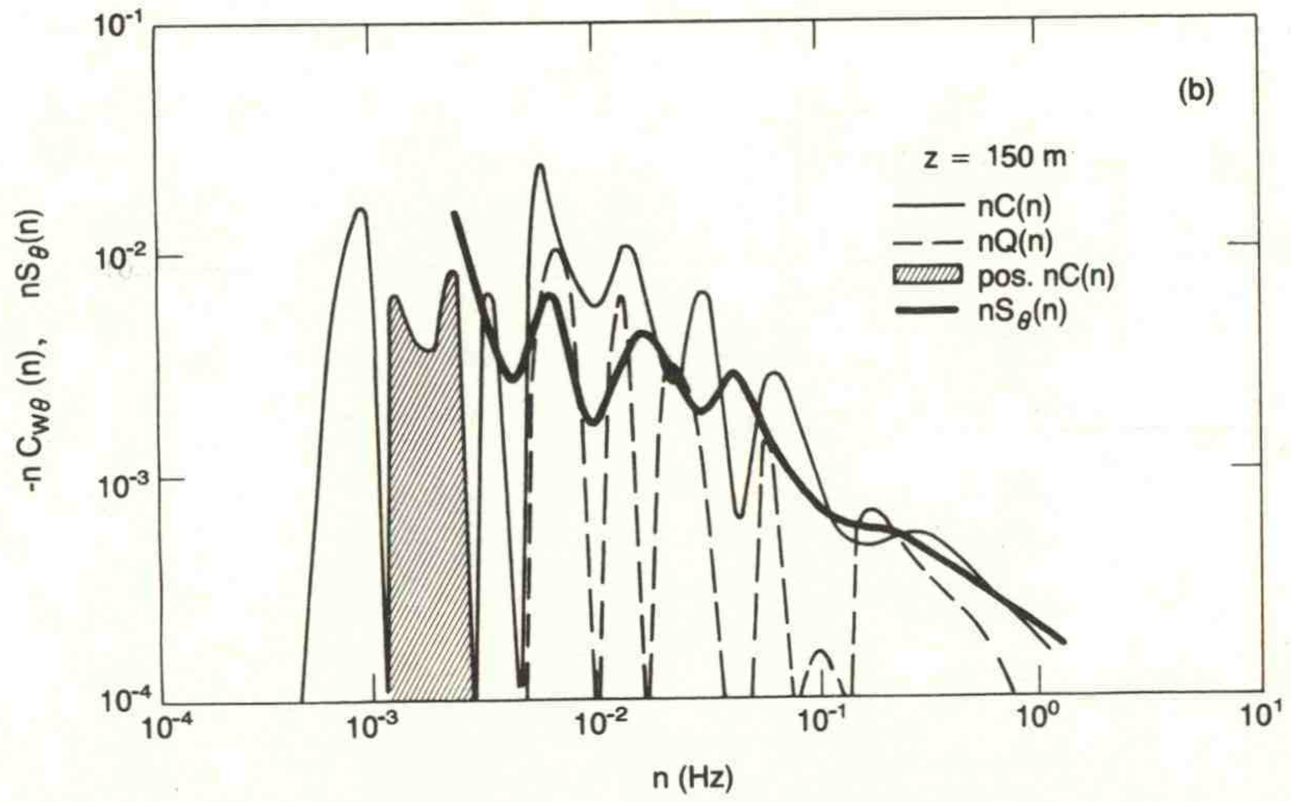
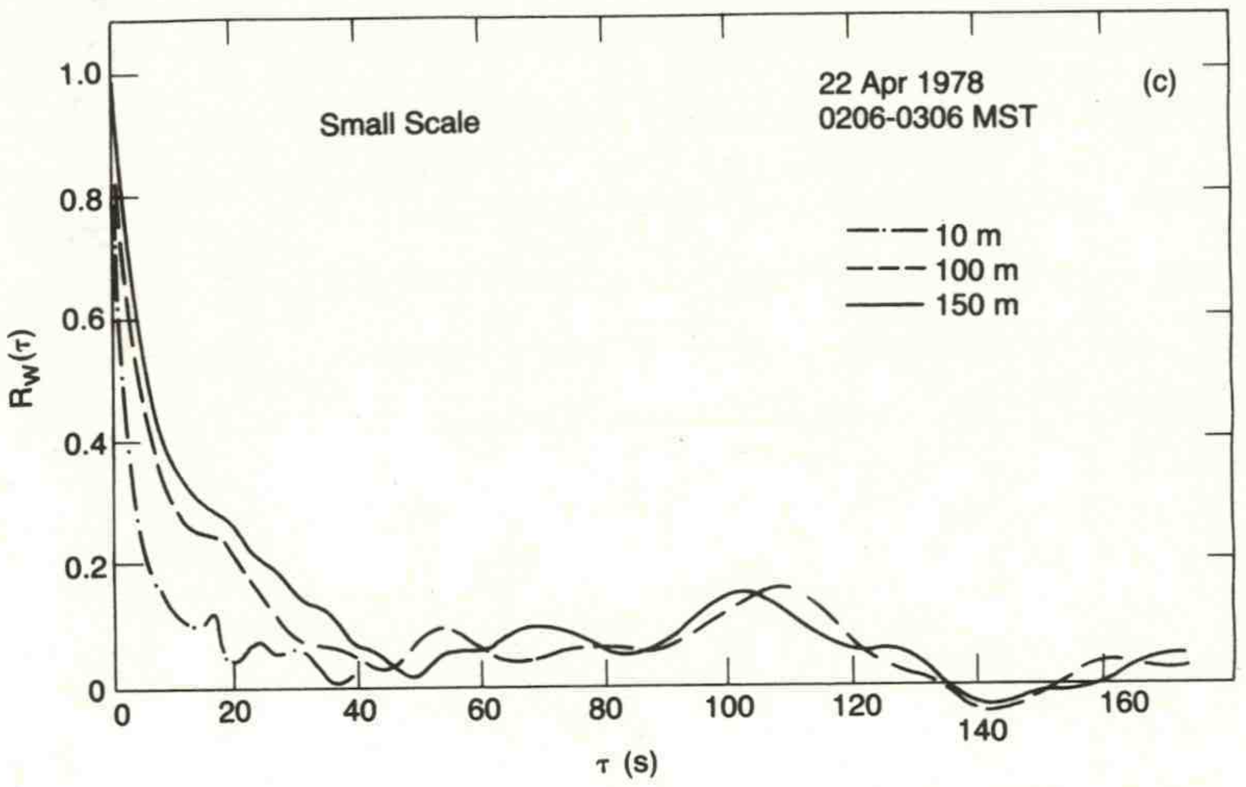


Figure 1.6.--Typical spectra for (a) and (b) moderate (18 April 1978) and (c) and (d) weak (15 April 1980) wave conditions. All spectra, cospectra, and quadspectra are from 150 m except for the 10-m w spectrum in (a). The modulus of the quadspectrum $|Q(n)|$ is plotted.







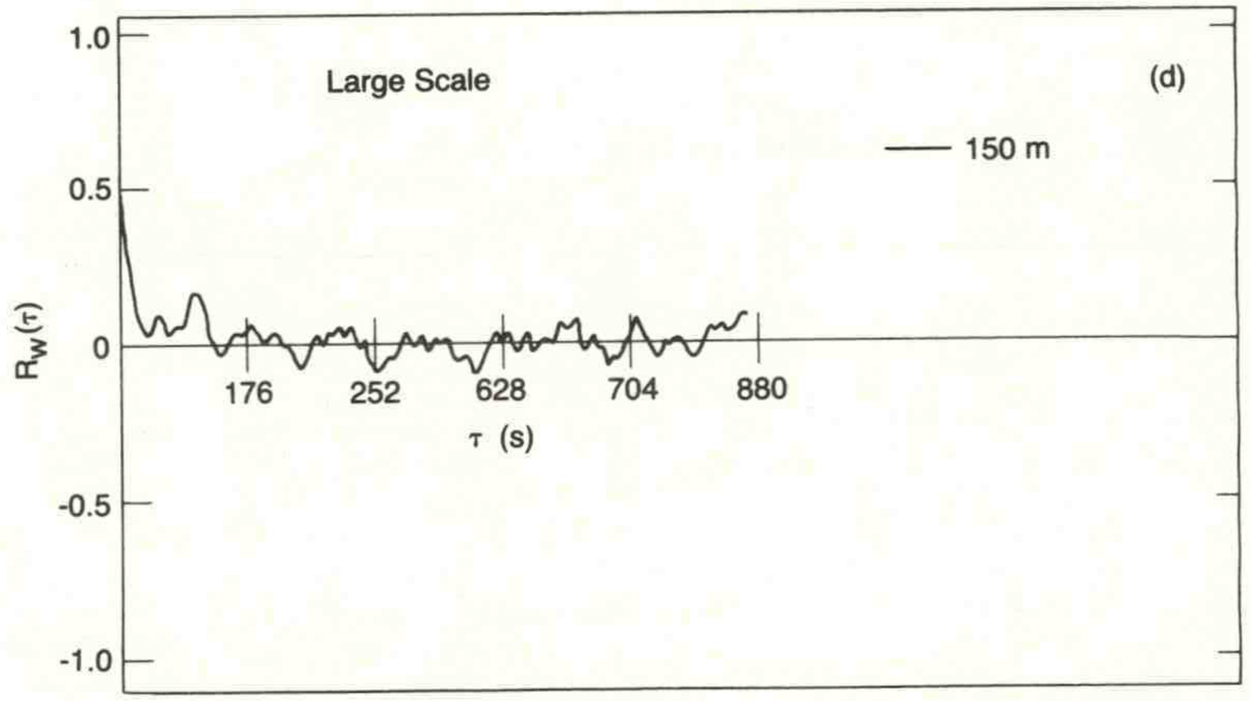
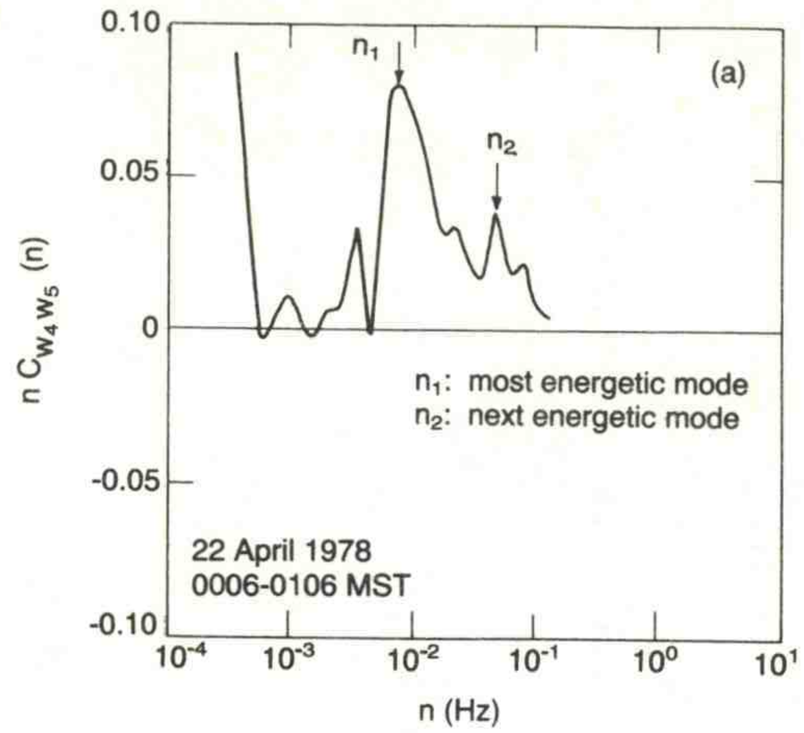
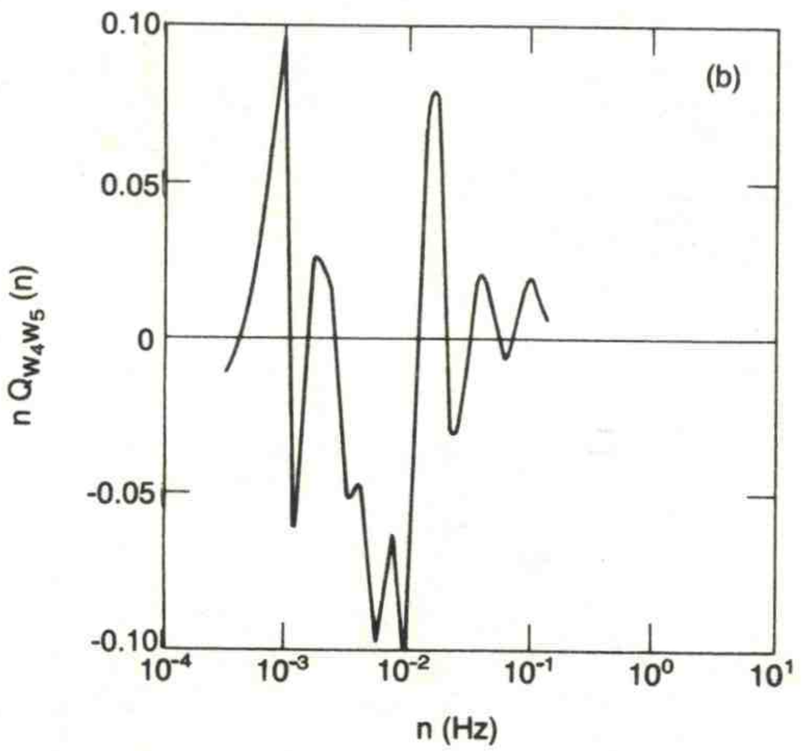
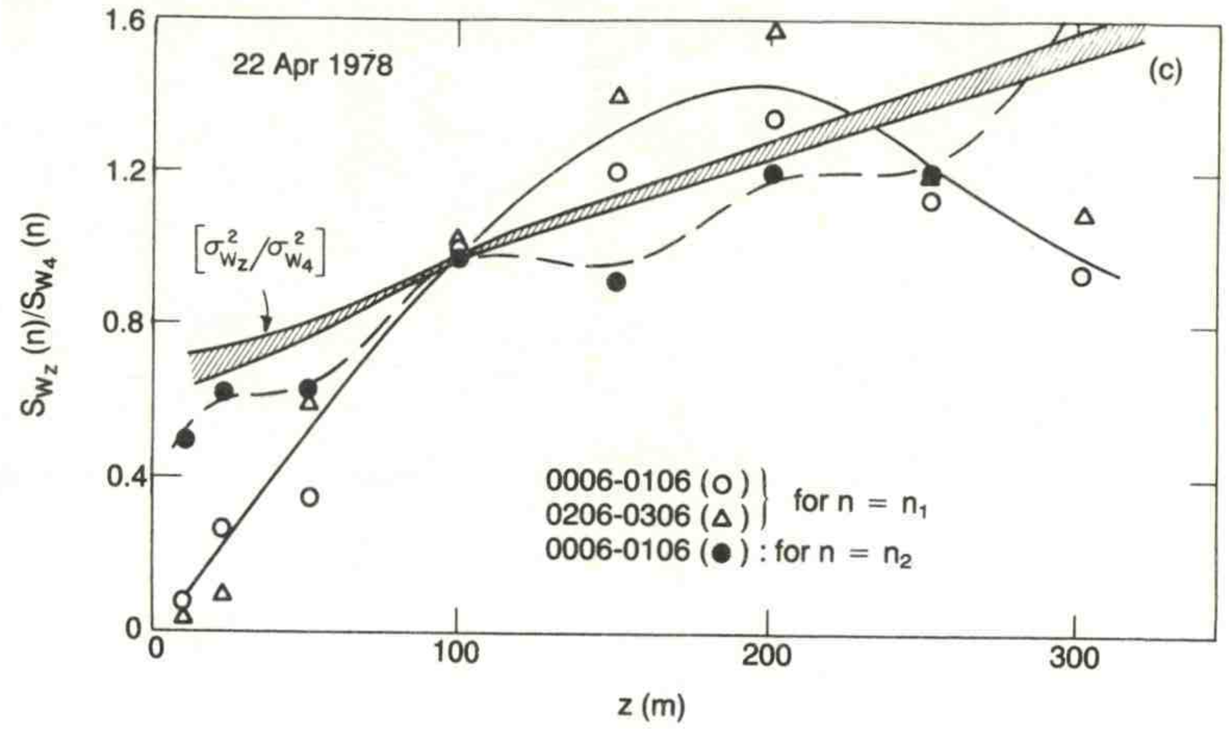


Figure 1.7.--Typical spectra, cospectra, and autocorrelations for the strong wave conditions of 22 April 1978. Spectra of w for four heights are shown in (a), but only the 150-m cospectra and quadspectra are shown in (b). Autocorrelations of w on small and large time scales are shown in (c) and (d).







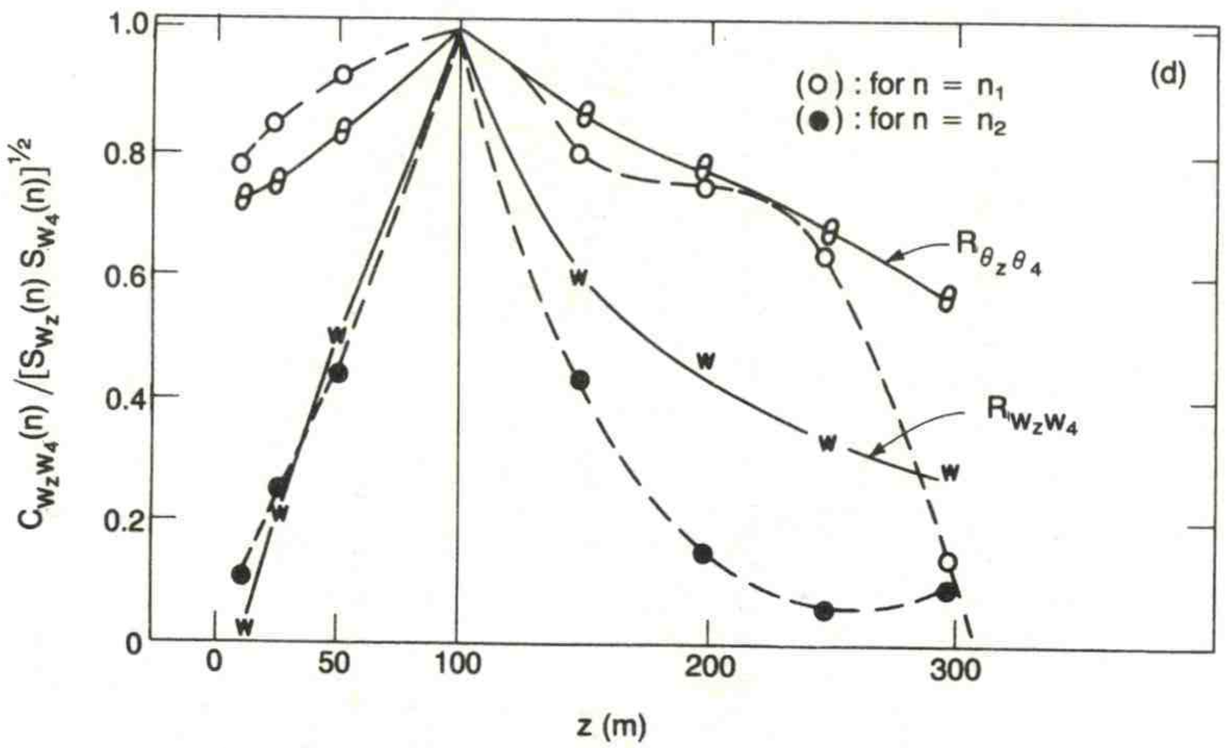


Figure 1.8.--Cross spectra and correlations between different heights in strong wave conditions. (a) $w_4 w_5$ cospectra and (b) $w_4 w_5$ quadspectra for 0006-0106 MST, 22 April 1978. Subscripts 4 and 5 refer to 100- and 150-m tower levels respectively. (c) Profiles of energy in most energetic (n_1) wave motions for two periods, 0006-0106 MST ($n_1 \simeq 7 \times 10^{-3}$ Hz) and 0206-0306 MST ($n_1 \simeq 10^{-2}$ Hz), and the next energetic (n_2) wave motions for 0006-0106 MST ($n_2 \simeq 5 \times 10^{-2}$ compared with normalized σ^2_w at different heights, denotedly $\sigma^2_{w_z}$. (d) Correlation spectra of w for the most energetic (n_1) waves and the next energetic (n_2) waves compared with cross correlation coefficients of observed w and θ at different heights with observations at 100 m.

narrow frequency range. This "spiky" form is indicative of large phase shifts between w and θ and is a nonlinear phenomenon.

The w spectrum in Fig. 1.6c, for 15 April 1980, indicates that on this occasion, when L, N, and U have about the same values as on 18 April 1978, there is no discernible wave motion. But the θ spectrum in Fig. 1.6c and the $w\theta$ cospectrum and quadspectrum in Fig. 1.6d indicate some weak concentration of energy into bands of frequencies. Note that $Q_{w\theta}(n)$ does not have a spiky form at frequencies where $C_{w\theta}(n)$ is a maximum, another indication of the weakness of wave motion. For frequencies where the wave motions are weak, it is possible to define a length scale $L_x = U/2\pi n_m$ even for the temperature fluctuations. Here n_m is the value of frequency n where S(n) or C(n) is a maximum. The turbulent flow with very weak waves is comparable with the Kansas air flow analyzed by Kaimal (1973). The graphs are not shown here. However, it was found that the ratio $L_x^{(\theta)}/L_x^{(w)}$ is in the range 6 to 8 at 22 and 50 m, but this ratio is only about 3 at 150 m (as may be inferred from Fig. 1.6c); $L_x^{(w\theta)}/L_x^{(w)}$ is about 2 at 150 m.

Figure 1.7 shows typical spectra, cospectra, and autocorrelations $R_w(\tau)$ for strong wave conditions. Figure 1.7a shows how the strength of the wave motion centered at a few frequencies increases with height. (These frequencies can be picked out from the autocorrelations in Figs. 1.7c,d.) At 10 m the w spectrum has much the same form as the moderate and weak wave spectra of Figs. 1.6a,c. At greater heights, note the concentration of the heat flux at a few frequencies (Fig. 1.7b) and the spiky shape of the $Q_{w\theta}(n)$ quadspectrum. The contribution of these wavelike motions to $\overline{w\theta}$ is even greater than in the moderate wave conditions shown in Fig. 1.6b.

Figures 1.8a,b show how the energy in the cospectrum and quadspectrum of the vertical velocity measured at 100 and 150 m is also concentrated around a few frequencies, the first and second most energetic waves (denoted by n_1 and n_2) being at about 7×10^{-3} and 5×10^{-2} Hz respectively.* In Fig. 1.8c, we explore the variation of the energy in these two modes with height. We observe a noticeable maximum in $nS(n=n_1)$ at z = 200 m, but not in $nS(n=n_2)$.

* The first of these frequencies is close to the value of $N/2\pi$ in the deep stratified layer between 1.5 and 3 km.

The latter, monotonic increase is somewhat similar to the energy in the wave studied by Einaudi and Finnigan (1981). The former's distribution is distinctly dissimilar. The correlation of the vertical turbulence and temperature, and also the correlation spectra of vertical velocity at the first two most energetic frequencies, are plotted in Fig. 1.8d. Note how the correlation coefficient, $R_{w_z w_4}$ (subscript 4 denotes 100-m level), falls off with $|z-100|$, the height above or below 100 m, i.e., at a rate similar to the falloff of $C_{w_z w_4}(n=n_2)$. But the correlation in $C_{w_z w_4}(n=n_1)$ is much higher and is comparable with that of $R_{\theta_z \theta_4}$, showing again how the temperature fluctuations are driven by wave motions to a greater extent than the vertical velocity fluctuations are.

Estimating the relative amounts of energy in turbulence and waves cannot be unambiguous since waves may well have random phases and be rotational, two features that are also important in low-frequency turbulence. If waves are motions with energy centered over a narrow frequency range, they can be identified if the cospectra and quadspectra are spiky. To estimate the energy of turbulence in the presence of waves, we assume that the contribution of turbulence to the spectrum is of the same form as that in the absence of waves (Figs. 1.9a,b). This was the assumption of Caughey et al. (1979) in their analysis of the Minnesota data. Thence we can say that on the basis of Figs. 1.6a,c on 18 April 1978 and 15 April 1980 for $z \leq 300$ m, and of Fig. 1.7a on 22 April 1978 for $z \leq 10$ m, the contribution of waves to the variance σ_w^2 was weak. But waves provided about 50% of σ_w^2 at 150 m on the strong-wave occasion of 22 April 1978.

A further distinction between different kinds of wave-turbulence combinations appears on examining the temperature and heat flux spectra. As is shown schematically in Figs. 1.9a-d on different stable days, w spectra may be largely similar to those in turbulent shear flows, but θ spectra and $w\theta$ cospectra may be quite different: on one occasion dominated by waves and on the other not. In the first of these two situations, we shall refer to the waves as "strong" (22 April 1978) or "moderate" (18 April 1978); on the second, we shall refer to them as "weak" (15 April 1980).

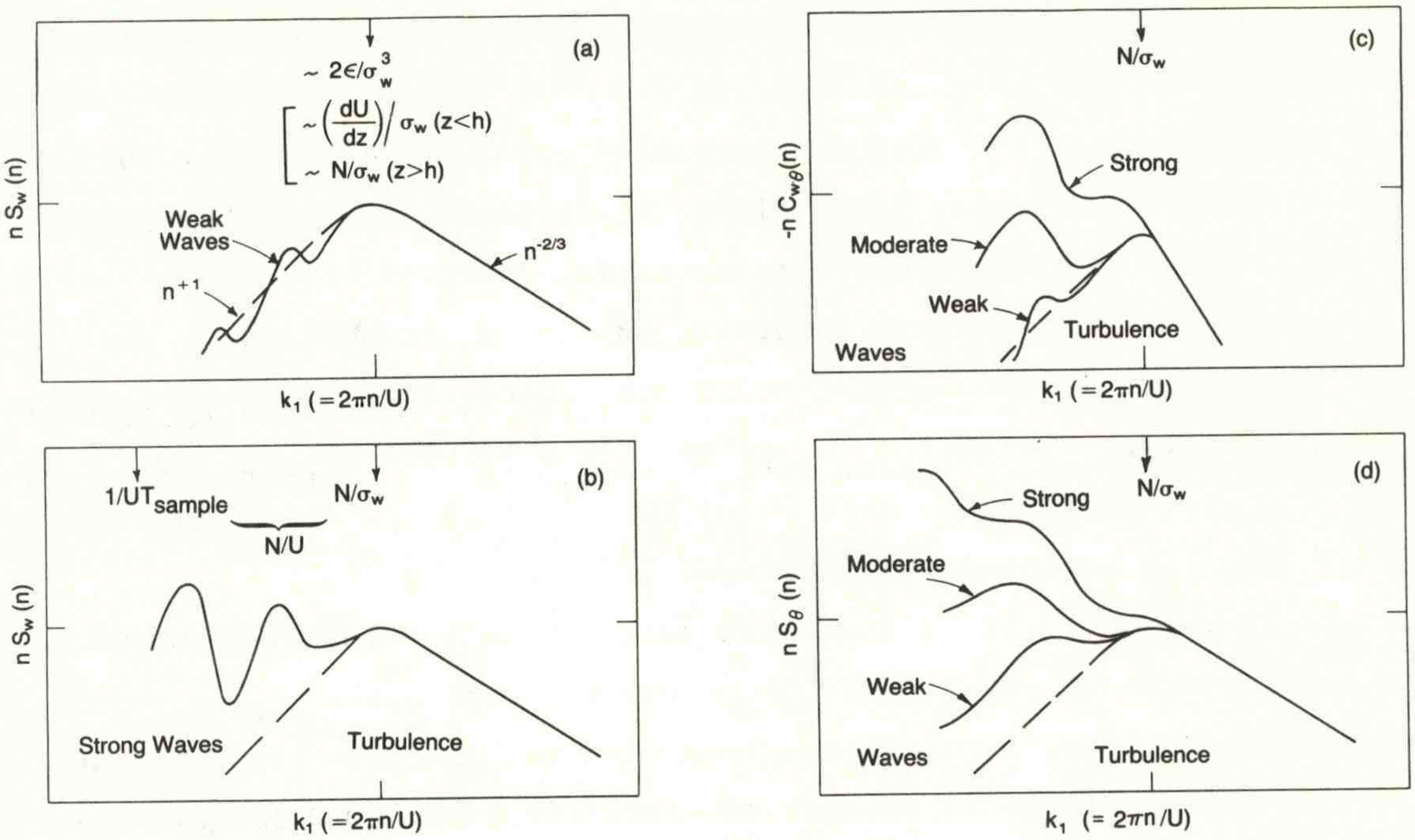


Figure 1.9.--Schematic form of spectra in stable conditions: (a) vertical velocity in the presence of weak waves (15 April 1980); (b) vertical velocity with strong waves (22 April 1978); (c) heat flux spectra; (d) temperature spectra.

To understand the dynamical processes in a stratified turbulent flow, one must estimate the rate of energy dissipation ε per unit mass, and relate it to the rate of buoyant production per unit mass, $B = g(\overline{w\theta})/T_o$, and to the ratio of the macroscopic velocity and integral scales, $0.4\ \sigma_w^3/L_x^{(w)}$ (see Appendix C). It is also of interest to estimate which part of the energy spectrum is contributing most to B. Only if the major contribution to B occurs at frequencies less than n_m can ε be estimated from the inertial subrange of the spectrum. (Otherwise the turbulent energy in the subrange would be transforming itself into potential energy.)

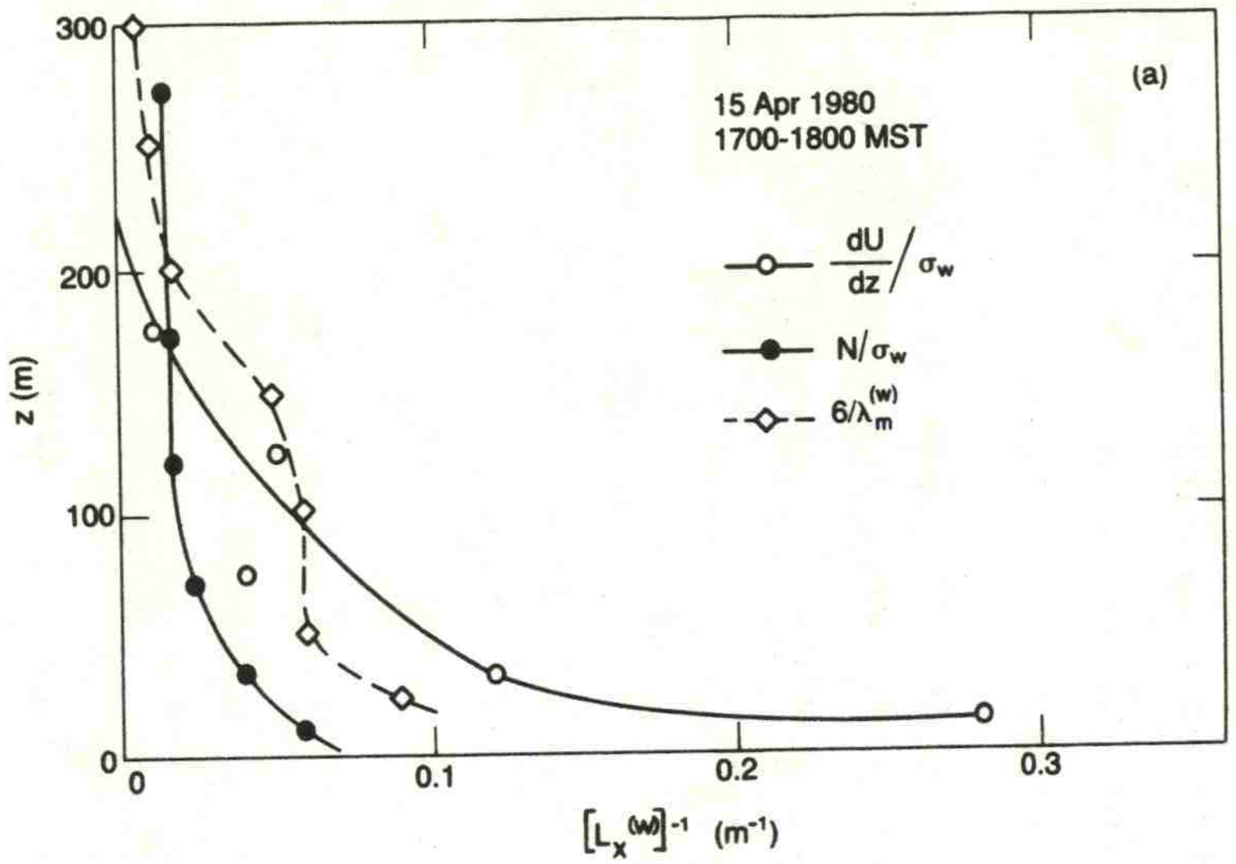
Our analysis of the measurements of $C_{w\theta}(n)$ shows that, even in the weak-wave case where $L^{(w\theta)} \simeq 2L^{(w)}$, the turbulence with scales larger than $L_x^{(w)}$ produces almost all the buoyancy flux. Consequently ε should be given by the value of $S_w(n)$ in the inertial subrange according to the result $S_w(n) \simeq (4/3)\ 0.5\ \varepsilon^{2/3}(2\pi n/U)^{-5/3}$ (Kaimal et al., 1972).

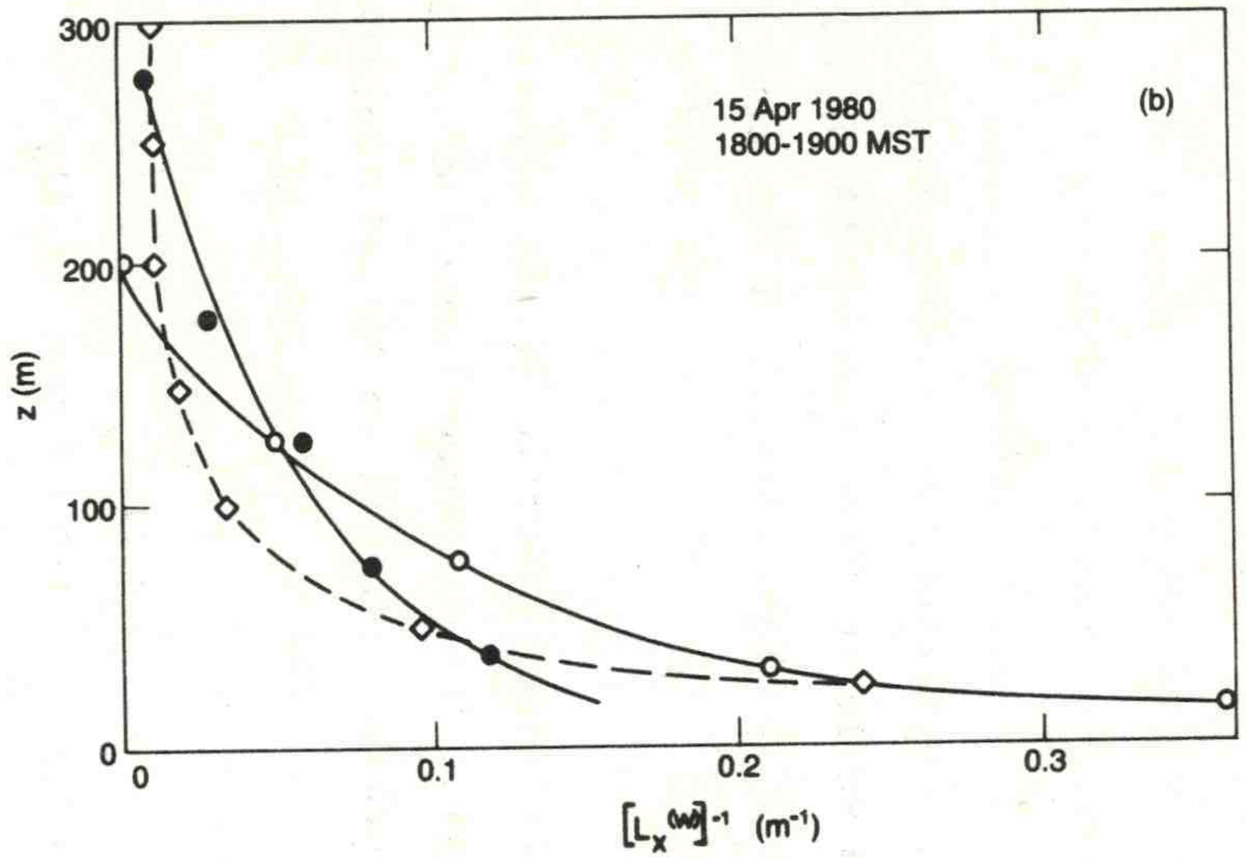
Using our measurements of 18 April 1978 at 2120 MST (moderate waves), we estimate $\varepsilon \simeq 0.0046\ m^2/s^3$ at 50 m and $0.4\ \sigma_w^3/L_x^{(w)} \simeq 0.005\ m^2/s^3$. For this case we find $|B/\varepsilon| \simeq 1/5$. On the strong-wave occasion of 22 April 1978 at 150 m, $\varepsilon \simeq 0.0037\ m^2/s^3$ and $|B/\varepsilon| \simeq 1/2$. It is interesting to compare $(\varepsilon/0.4\ \sigma_w^3)^{-1}$ with two length scales: the scale of the peak of the $nS_w(n)$ spectrum, $2\pi n_m/U$, and the scale σ_w/N. In this case, inspection of the spectra in Fig. 1.7 shows that the turbulent component of the w variance is about half the total variance. Thence the scale $[\varepsilon/(0.4\ \sigma_{w(t)}^3)]^{-1} \cong 59$ m, whereas $(2\pi n_m/U)^{-1} \simeq 40$ m and $(N/\sigma_w)^{-1} \simeq 100$ m. They are all of the same order (as they are in non-wavy conditions).

Since in strongly stable conditions the integral scale of the vertical component of turbulence is small compared with the distance above the surface (for $z \gtrsim 25$ m), it is plausible that the turbulence scale is largely determined by local conditions, namely the values of dU/dz, σ_w, and N, which determine the two natural inverse length scales $(dU/dz)/\sigma_w$ and N/σ_w (see Fig. 1.9). (Theoretical arguments for the dependence of $L_x^{(w)}$ on z, σ_w, dU/dz, and N are summarized in Appendix D.) An integral scale is most easily derived by using the spectrum of w to infer that $L_x^{(w)} \simeq U/(2\pi n_m)$, where n_m is the value of n where $nS_w(n)$ is a maximum. (This definition is equal to the true integral scale if the autocorrelation is an exponential function.) Evidently this definition is not appropriate for turbulence with strong waves, where the spectrum (as in Fig. 1.7a) does not have a maximum.

The values of n_m, even in the spectra chosen here, are uncertain to within a factor of about $\pm 25\%$. First, Figs. 1.10a-c show how $L_x^{(w)}$ increases to a large but finite value where the shear vanishes ($dU/dz \to 0$). This finite value approximates to σ_w/N. Second, the results show that in the lower part of the shear layer the vertical profile of $[L_x^{(w)}]^{-1}$ more closely approximates the profile of $(dU/dz)/\sigma_w$ than the profile of N/σ. To within 50%, the BAO data agrees with the formula for level ground [(D.14) of Appendix D] that $[L_x^{(w)}]^{-1} \simeq 0.7\ (dU/dz)/\sigma_w + 1/z$ (when $dU/dz > N$).

Note in Fig. 1.10c how the values of $L_x^{(w)}$ measured in the Kansas experiment at the same Monin-Obukhov length L are about half the values of





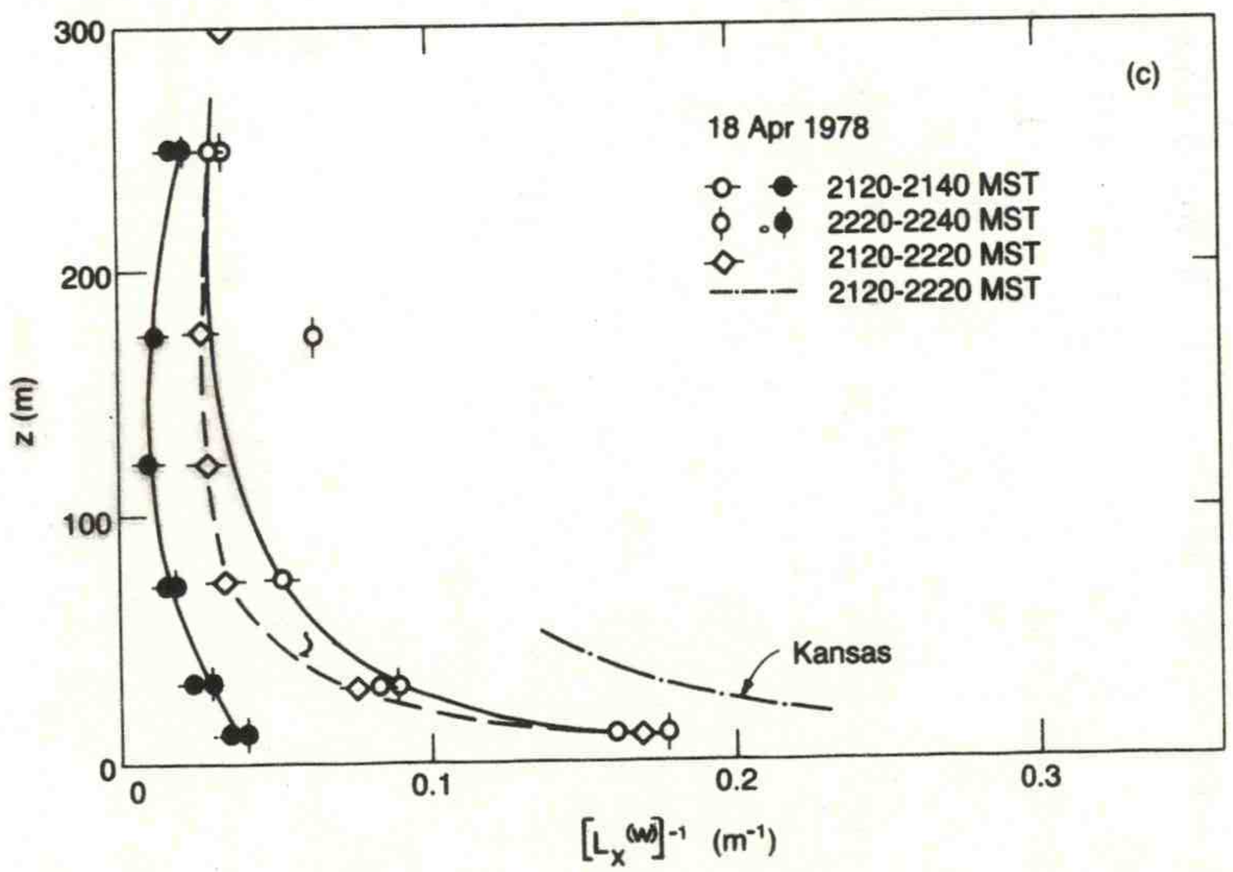


Figure 1.10.--Comparison of the reciprocals of length scales, $(dU/dz)/\sigma_w$ and N/σ_w (imposed by shear and buoyancy), with the reciprocal of the integral scale of vertical velocity $[L_x^{(w)}]^{-1}$ ($\simeq 6/\lambda_m^{(w)}$, where $\lambda_m^{(w)} = U/n_m$) in conditions with weak waves for two periods (a) and (b) on 15 April 1980 and moderate waves (c) on 18 April 1978. Comparison is also made in (c) with the stable data from Kansas where $[L_x^{(w)}]^{-1} \simeq 2.9\ z^{-1}\ (1 + 4\ z/L)$ as shown in Appendix C. Monin-Obukhov length L is 100 and 50 m respectively for the 1-h periods in (a) and (b) and 148 and 166 m for two successive 20-min periods in (c). The Kansas curve is based on a 1-h average (2120-2220 CST); L = 142 m.

$L_x^{(w)}$ in these experiments, where wave motions (even though weak) may increase $L_x^{(w)}$. Despite the scatter in our results, this difference is probably real.

The spectra of θ and cospectra of $w\theta$ in Figs. 1.6 and 1.7 show how the temperature fluctuations and the heat flux are controlled by motions with larger scales than that of the vertical velocity. The results of Fig. 1.10 indicate that such scales are likely to be affected by the buoyancy length scale σ_w/N. In the moderate- and strong-wave cases, these large motions are mostly waves that are also likely to be controlled by the local value of N if the vertical variation of N is small. If N(z) varies sharply, then other modes can be generated as in the case studied by Einaudi and Finnigan (1981). The upper-air soundings in Appendix A are rather different to their situation. These are the immediate reasons for suspecting that σ_w, N, and $d\bar{\theta}/dz$ are the main parameters determining σ_θ and the heat flux. For the idealized situation of homogeneous turbulence in a strongly stable stratification, the Lagrangian model of Pearson et al. (1982) suggests that

$$\sigma_\theta \simeq \zeta_\theta \, (\sigma_w/N)(d\bar{\theta}/dz) \, , \tag{1.1}$$

where ζ_θ is a temperature fluctuation parameter of the order of unity. In fact for a wide class of turbulence, $\zeta_\theta \simeq 1/\sqrt{2}$. The model also predicts that the coefficient of thermal diffusivity is given by

$$K_\theta = \frac{-\overline{w\theta}}{d\bar{\theta}/dz} \simeq F \, \sigma_w^2/N \, , \tag{1.2}$$

where F is a thermal diffusivity parameter much smaller than unity and roughly independent of $\sigma_w/(L_x^{(w)}N)$. The relationship in (1.2) can also be written to show that the effective length scale of turbulence governing heat flux (i.e., K_θ/σ_w) is equal to $F \, \sigma_w/N$. It is important to underline that this theory makes no distinction between wavy and turbulent motions at low frequency, and therefore suggests that in measuring ζ_θ and F we should not expect any great sensitivity to waviness.

Consequently in Fig. 1.11 we have plotted $\sigma_\theta/(d\bar{\theta}/dz)$ as a function of σ_w/N for all three of the days and conditions considered here from 16 m (where $d\bar{\theta}/dz$ is evaluated) to 275 m (σ_θ is interpolated). We have only included points where $d\bar{\theta}/dz$ can be calculated. In some cases, $d\bar{\theta}/dz$ is indeterminate because instruments were not working or because its value is too small (0.0005°C/m).

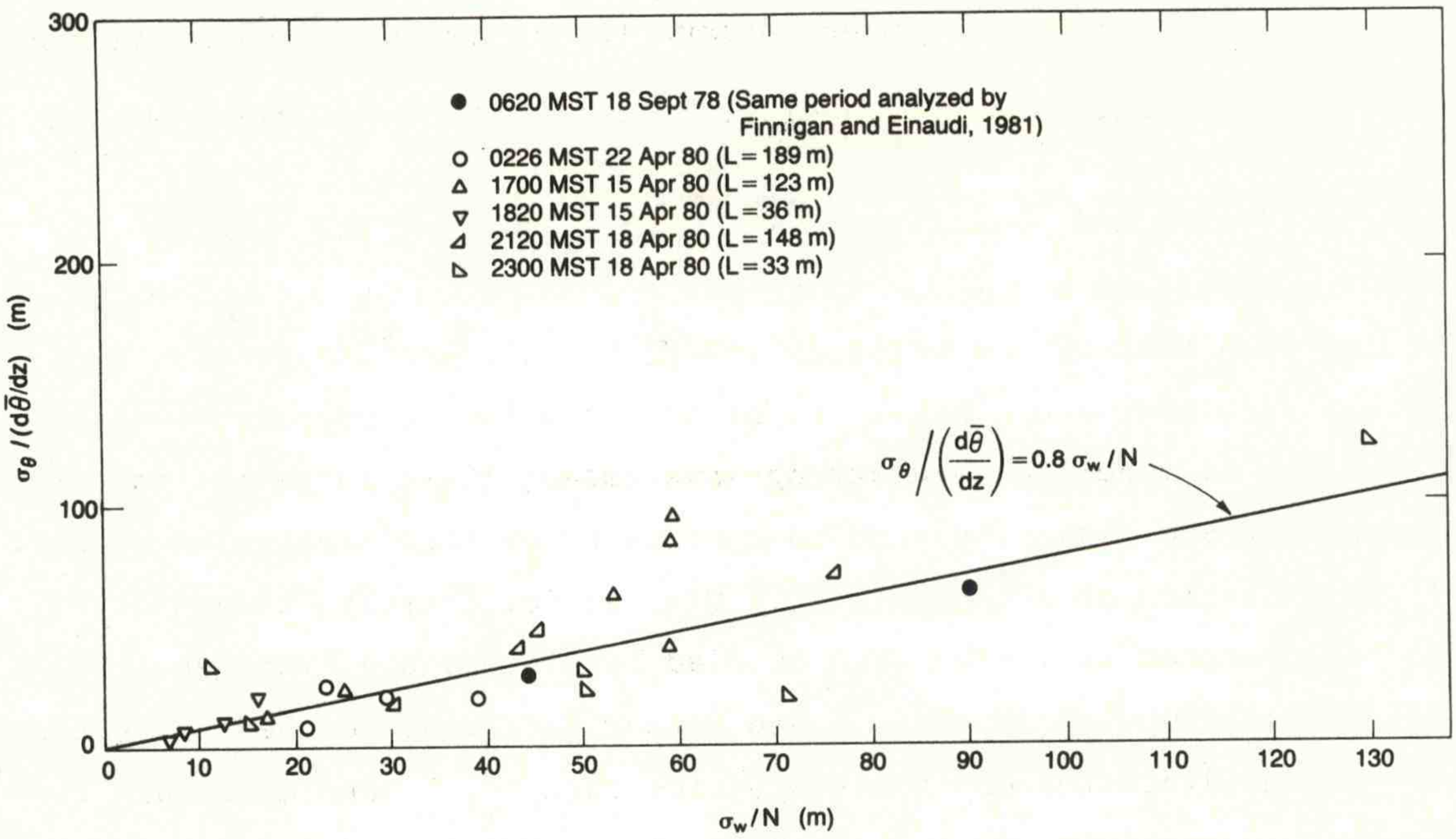


Figure 1.11.--Plot of the relationship in eq. (1.1) showing $\zeta_\theta \simeq 0.8$, irrespective of variations in z or L or the existence of waves.

In the latter case, temperature fluctuations persist, but there can no longer be a local connection between σ_θ and $d\bar{\theta}/dz$. (There are only about three excluded points, and all are at 225 m.)

The agreement with (1.1) is reasonably good, the observed constant ζ_θ being about 0.8 (see Fig. 1.11), compared with 0.7 in the theoretical model. Note that the correlation of the Kansas surface layer data for strong stability ($z < 25$ m) gives ζ_θ between 0.5 and 1.0 (see Appendix B). There is no apparent trend in the value of ζ_θ with z or with the existence or absence of wave motions.

Figure 1.12a shows how the effective length scale of the heat flux (K_θ/σ_w) varies with height in the stable boundary layer. Note the marked variation of the reciprocal heat flux σ_w/K_θ even over an hour. Figure 1.12b shows that σ_w/K_θ is an approximately linear function of N/σ_w; it does not correlate well with the velocity gradient length scale $(dU/dz)/\sigma_w$. Finally in Fig. 1.13, F (i.e., $K_\theta/\sigma_w \div \sigma_w/N$) is plotted as a function of the effectively largest scale of motion in these stratified flows (σ_w/N) and as a function of the inverse square root of the Richardson number $Ri^{-1/2} = (dU/dz)/N$. There is no obvious trend in this data. [According to surface boundary similarity arguments F

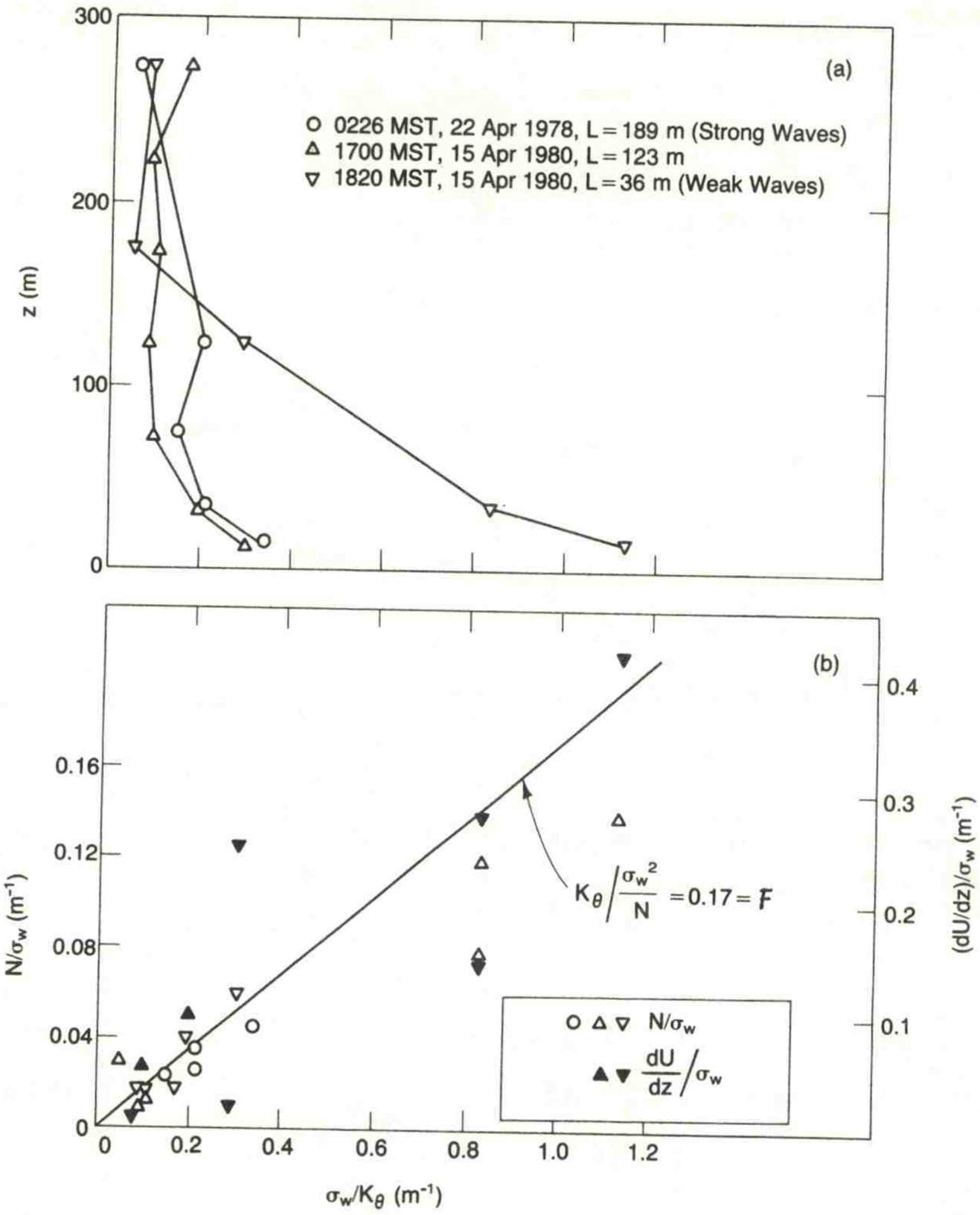


Figure 1.12.--Reciprocal heat flux scale σ_w/K_θ plotted as a function of (a) height and (b) reciprocal length scales imposed by buoyancy N/σ_w and by shear $(dU/dz)/\sigma_w$.

should be a function of z/L or $z/(\sigma_w/N)$, when $z/L \gg 1/5$.] The fact that the average value of F is about 0.17, which is half the value in the Kansas experiment, might be explained by the relatively larger values of σ_w associated with the wave motions present here. However there is no direct correlation between wave motion and any of the results in Fig. 1.13.

Recent measurements by Nieuwstadt (1982) at the Cabauw tower in the Netherlands also showed that in stable conditions above about 100 m the temperature fluctuations and heat flux could be scaled on the local turbulence and temperature gradient. His results yield $\zeta_\theta \simeq 1.3$ and $F \simeq 0.25$. Unlike us, he found that F systematically decreased as z decreased, reaching a value of about 0.1 at $z/L \simeq 0.1$.

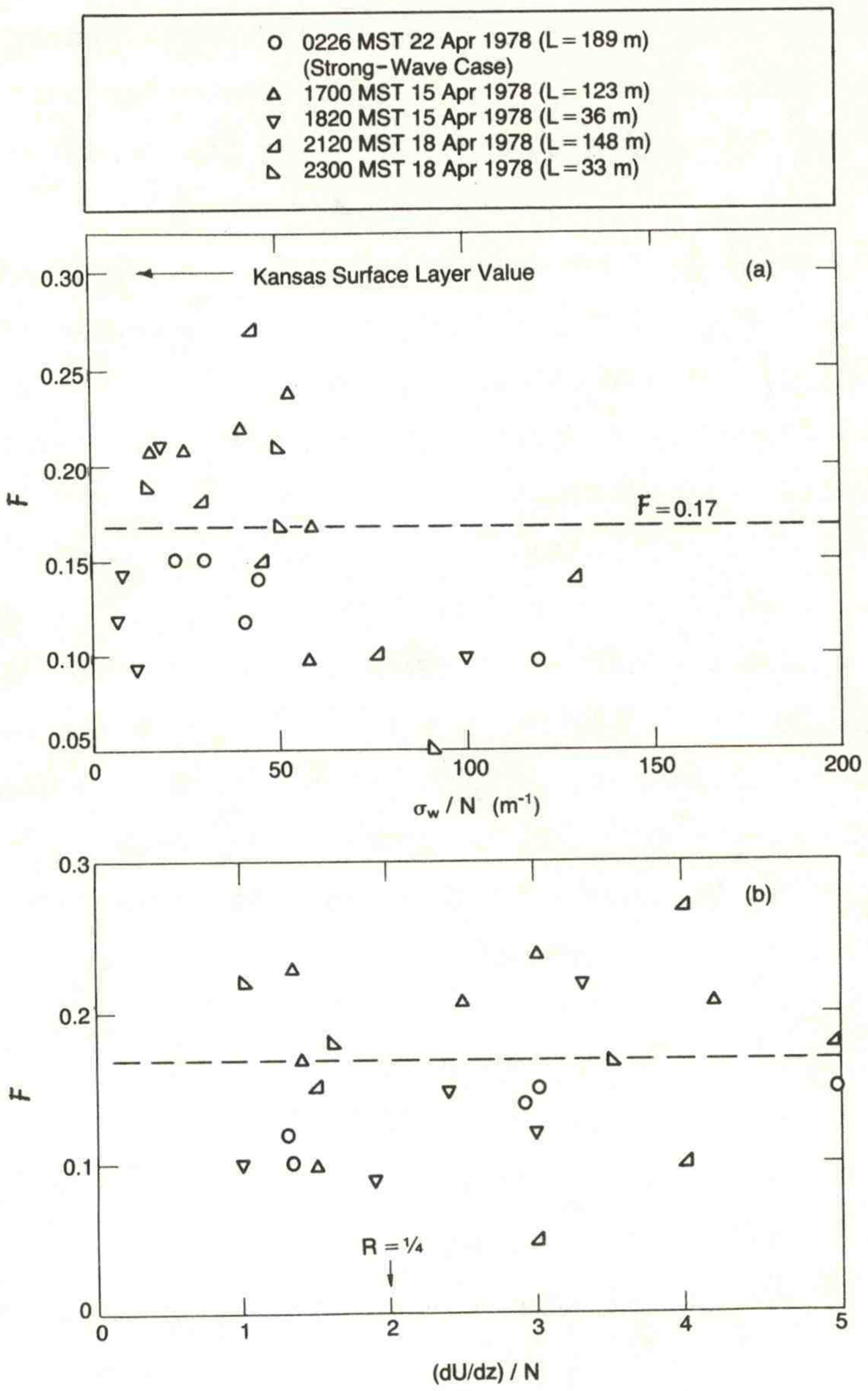


Figure 1.13.--Thermal diffusivity parameter $F = K_\theta/(\sigma_w^2/N)$ as a function of (a) σ_w/N and (b) $(dU/dz)/N$ (i.e., $Ri^{-1/2}$).

1.5 TENTATIVE CONCLUSIONS

(1) The presence of coherent wave motions in stable atmospheric flows cannot be detected from the mean temperature and velocity profiles, nor even on some occasions from spectra of the vertical velocity.

(2) Vertical wave motions are most likely to be detected by temperature spectra and/or temperature-vertical velocity cospectra. Cospectra, quad-spectra, and autocorrelations help identify the frequencies where wave energy

is particularly concentrated. Waves of higher frequency appear to be correlated over smaller vertical distances. Temperature fluctuations are better correlated over larger vertical distances than are the velocity fluctuations.

(3) It may be useful to consider turbulence in stably stratified conditions as belonging to one of three categories: weak, moderate, or strong wave conditions, depending on whether significant wave effects are present in neither velocity nor temperature spectra, only temperature (or $w\theta$ cospectra), or both w and θ spectra, respectively.

(4) Wave motions and large-scale turbulence are both agents for the transport of heat and the production of temperature fluctuations. In the presence of a stable density gradient, where the buoyancy frequency N is approximately uniform with height, it appears that both processes are associated with vertical motions on a scale approximately equal to σ_w/N, over a time scale of order N^{-1}. Consequently dimensionless parameters can be defined to estimate (or correlate) temperature fluctuations σ_θ or thermal diffusivity K_θ:

$$\sigma_\theta \simeq \zeta_\theta \ (\sigma_w/N)(d\bar{\theta}/dz)$$

$$K_\theta \simeq F \ \sigma_w(\sigma_w/N) \ ,$$

where typically

$$\zeta_\theta \simeq 0.8 \pm 0.25$$

$$F \simeq 0.2 \pm 0.1 \ .$$

[Note that these general ideas are not appropriate when vertical oscillations are driven by elevated inversions, i.e., strong variations in N. Indeed, as Finnigan (CSIRO, Canberra, Australia; personal communication) has pointed out, wave-induced heat flux may then be in the opposite direction to the high frequency wave and turbulent flux.]

(5) The integral scale for the vertical turbulence velocity is shown to be approximately given by

$$[L_x^{(w)}]^{-1} \simeq \frac{dU/dz}{\sigma_w}$$

in the lower part of the boundary layer, at $z \simeq 25$ m. Below this height, the direct effect of the ground on the eddies has to be considered; other data and theoretical arguments given in Appendix D suggest, in stable neutral and unstable conditions,

$$[L_x^{(w)}]^{-1} \simeq 0.7 \frac{dU/dz}{\sigma_w} + \frac{1}{z} .$$

In the upper part of the boundary layer and above it (to within a factor of about 2)

$$[L_x^{(w)}]^{-1} \simeq N/\sigma_w \quad \text{(when } N >> dU/dz\text{)} .$$

(6) The integral scales of temperature $L_x^{(\theta)}$ and $w\theta$ fluctuations $L_x^{(w\theta)}$ are greater than those of $L_x^{(w)}$. (They can only be defined in weak wave conditions.) Typically when $z \gtrsim 100$ m in such conditions $L_x^{(\theta)}/L_x^{(w)} \simeq 3$; $L_x^{(w\theta)}/L_x^{(w)} \simeq 2$. Near the surface, $L_x^{(w)}$ decreases where $L_x^{(\theta)}$ does not; so at 22 m or 50 m, $L_x^{(\theta)}/L_x^{(w)} \simeq 7 \pm 1$.

(7) Whether waves are present or not, inertial subrange spectra are observed for w and θ. Measurements of ε from this range are consistent to within a factor of 2 with the usual estimate based on the turbulent component of the total variance (σ_w^2) and with local integral scales estimated on the basis of σ_w/N and the wavenumber at the peak in the spectra.

(8) From a practical point of view, the data show unmistakably how heat is transferred vertically by wave or wavelike motions as well as by low-frequency turbulent motions. Consequently contaminants can also be transferred by such processes. Therefore it is important that, in the presentation and recording of measurements of atmospheric turbulence, the wavelike motions should be included. [By excluding spectral contributions from frequencies below 0.001 Hz (Caughey et al., 1979) in the analysis of the Minnesota data, the data appeared to be very consistent, presumably because it was just a turbulence record. But the analysis may be misleading if it is to be used to estimate heat or contaminant fluxes.]

(9) The second practical point about the data is that they provide evidence for the theoretical suggestion of Pearson et al. (1982) that in a

stably stratified flow, diffusion heat or pollutant transfer takes place more by slow mixing between fluid elements, which are constrained in their vertical motions to a distance of about σ_w/N, rather than by large-scale advection or transport by fluid elements. If $F \simeq 0.2$, it means that the time scale for a fluid element to change its temperature is about $5\ N^{-1}$. Therefore vertical diffusion of any pollution released from an elevated source into the atmosphere is limited to σ_w/N for some distance downwind of a source until mixing can occur. This prediction for the vertical extent of a plume in strongly stable flows can also be estimated from the variance of temperature fluctuations σ_θ^2 using eq. (1.1).

1.6 ACKNOWLEDGMENTS

JCRH is grateful for stimulating conversations with J.C. Wyngaard and very helpful comments by S.P.S. Arya, H.J. Pearson, W. Rodi, J.J. Finnigan, and P.J. Mason.

1.7 REFERENCES

Britter, R.E., J.C.R. Hunt, L. Marsh, and W.H. Snyder, 1983: Turbulent diffusion in a stratified fluid. J. Fluid Mech. (in press).

Brost, R.A., and J.C. Wyngaard, 1978: A model study of the stably stratified planetary boundary layer. J. Atmos. Sci., 35, 1427-1440.

Busch, N.E., 1973: The surface boundary layer. Bound.-Layer Meteorol., 4, 213-240.

Caughey, S.J., J.C. Wyngaard, and J.C. Kaimal, 1979: Turbulence in the evolving stable boundary layer. J. Atmos. Sci., 36, 1041-1052.

Csanady, G.T., 1964: Turbulent diffusion in a stratified flow. J. Atmos. Sci., 7, 439-447.

Einaudi, F., and J.J. Finnigan, 1981: The interaction between an internal gravity wave and the planetary boundary layer. Part I: The linear analysis. Quart. J. Roy. Meteorol. Soc., 107, 793-806.

Finnigan, J.J., and F. Einaudi, 1981: The interaction between an internal gravity wave and the planetary boundary layer. Part II: Effect of the wave on the turbulence structure. Quart. J. Roy. Meteorol. Soc., 107, 807-832.

Hunt, J.C.R., 1981: Turbulent stratified flow over hills. Proceedings, Colloquium on "Construire avec le Vent," Centre Sci. Tech. du Bat, Nantes, France, paper I-1.

Hunt, J.C.R., 1982: Turbulent diffusion in the stably stratified boundary layer. Proceedings, Short Course on Boundary Layer Meteorology in Air Pollution Modeling, Royal Netherlands Meteorological Institute, De Bilt, F.T.M. Nieuwstadt and H. Van Dop, eds., Reidel, Dordrecht, Netherlands, 231-274.

Hunt, J.C.R., 1983: Turbulence structure in convective and shear-free boundary layers. J. Fluid Mech. (submitted).

Hunt, J.C.R., and J.M.R. Graham, 1978: Free-stream turbulence near plane boundaries. J. Fluid Mech., 83, 209-235.

Hunt, J.C.R., and W.H. Snyder, 1980: Experiments on stably and neutrally stratified flow over a model three-dimensional hill. J. Fluid Mech., 96, 671-704.

Hunt, J.C.R., and A.H. Weber, 1979: A Lagrangian statistical analysis of diffusion from a ground level source in a turbulent boundary layer. Quart. J. Roy. Meteorol. Soc., 105, 423-443.

Kaimal, J.C., 1973: Turbulence spectra, length scales and structure parameters in the stable surface layer. Bound.-Layer Meteorol., 4, 289-309.

Kaimal, J.C., J.C. Wyngaard, y. Izumi, and O.R. Coté, 1972: Spectral characteristics of surface layer turbulence. Quart. J. Roy. Meteorol. Soc., 98, 563-589.

Kaimal, J.C., R.A. Eversole, D.H. Lenschow, B.B. Stankov, P.H. Kahn, and J.A. Businger, 1982: Spectral characteristics of the convective boundary layer over uneven terrain. J. Atmos. Sci., 39, 1098-1114.

Klemp, J.B., and D.K. Lilly, 1975: The dynamics of wave-induced downslope winds. J. Atmos. Sci., 32, 320-329.

Monin, A.S., and A.M. Yaglom, 1971: Statistical Fluid Mechanics, Vol. 1. MIT Press, Cambridge, Mass., 769 pp.

Nieuwstadt, F.T.M., 1982: Observations on the turbulent structure of the stable boundary layer. Quart. J. Roy. Meteorol. Soc. (submitted).

Okamoto, M., and E.K. Webb, 1970: The temperature fluctuations in stable stratification. Quart. J. Roy. Meteorol. Soc., 96, 591-600.

Pearson, H.J., and R.E. Britter, 1980: A statistical model for vertical turbulent diffusion in stably stratified flows. Proceedings, 2nd International Symposium on Stratified Flows, Trondheim, 24-27 June, Tapir Publishers, Trondheim, Norway, 269-279.

Pearson, H.J., J.S. Puttock, and J.C.R. Hunt, 1983: A statistical model of fluid element motions and vertical diffusion in homogeneous stratified fluid. J. Fluid Mech. (in press).

Prandtl, L., 1952: The Essentials of Fluid Dynamics. Hofner, New York, 452 pp.

Scorer, R.S., 1949: Theory of waves in the lee of mountains. Quart. J. Roy. Meteorol. Soc., 75, 41-56.

Sherman, F.S., J. Imberger, and G.M. Corcos, 1978: Turbulence and mixing in stably stratified waters. Ann. Rev. Fluid Mech., 10, 267-288.

Smith, R.B., 1980: Linear theory of stratified hydrostatic flow past an isolated mountain. Tellus, 32, 348-364.

Townsend, A.A., 1958: Turbulent flow in a stably stratified atmosphere. J. Fluid Mech., 3, 361-372.

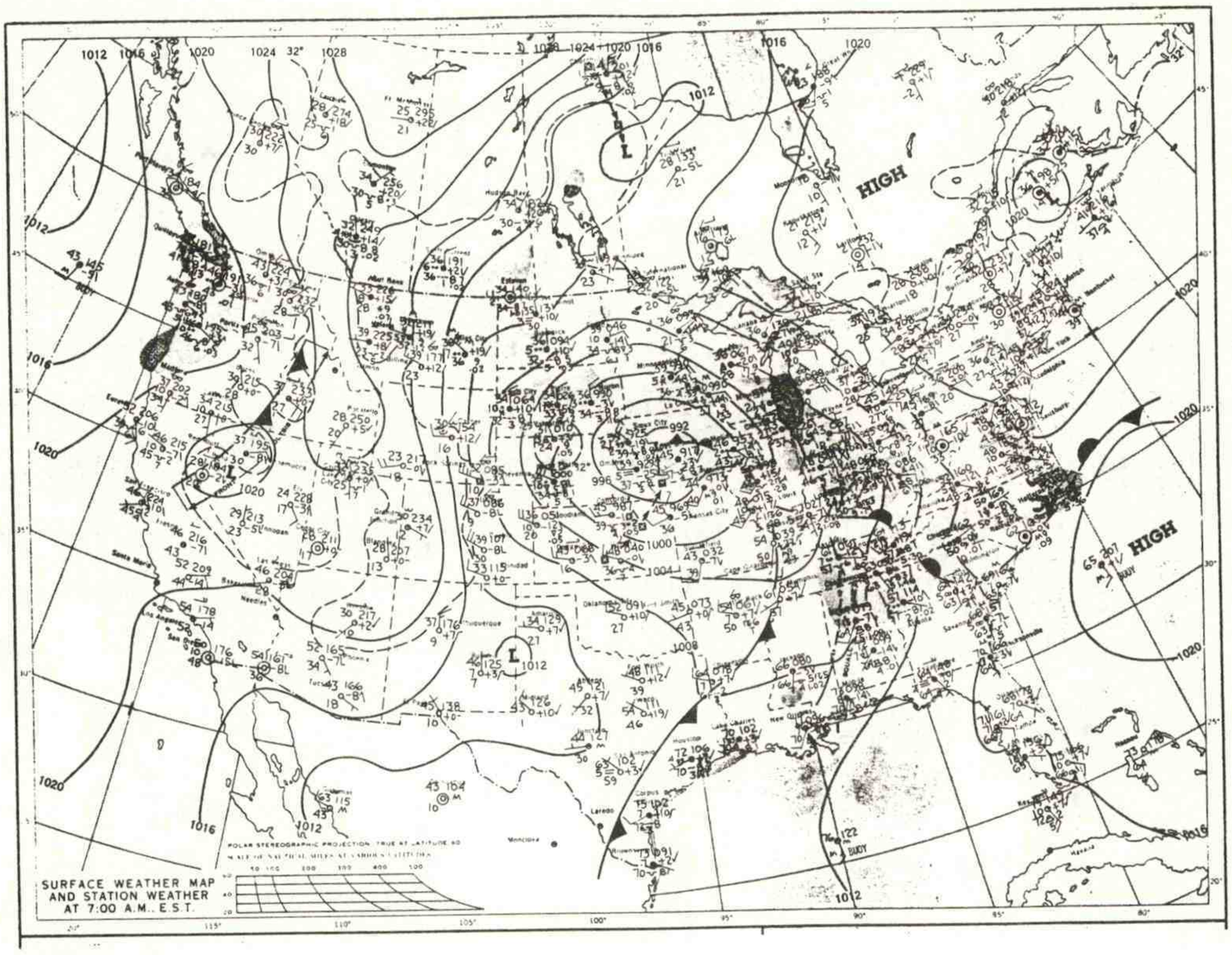
Townsend, A.A., 1976: Structure of Turbulent Shear Flow. Cambridge University Press, Cambridge, England, 429 pp.

Turner, J.S., 1973: Buoyancy Effects in Fluids. Cambridge University Press, Cambridge, England, 367 pp.

Wyngaard, J.C., O.R. Coté, and Y. Izumi, 1971: Local free convection, similarity, and the budgets of shear stress and heat flux. J. Atmos. Sci., 28, 1171-1182.

APPENDIX A: BACKGROUND DATA FOR OBSERVATION PERIODS

Presented here are background data on synoptic and boundary layer scales for the three nights discussed in this paper. The daily weather maps for 12 Z (0500 MST), published by NOAA's Environmental Data and Information Service, are reproduced in Figs. A.1-A.3. Two maps bracketing the selected nights are shown. The rawinsonde plots for Denver (30 km from the BAO) covering the same observation periods are presented in Figs. A.4-A.6. The upper-air soundings at 1700 MST the evening before and 0500 MST the morning after are shown to highlight changes occurring during the night. On a smaller scale, the profiles of the mean and turbulent properties of the stable boundary layer to a height of 300 m over 20-min averaging periods can be found in Tables A.1-A.4.



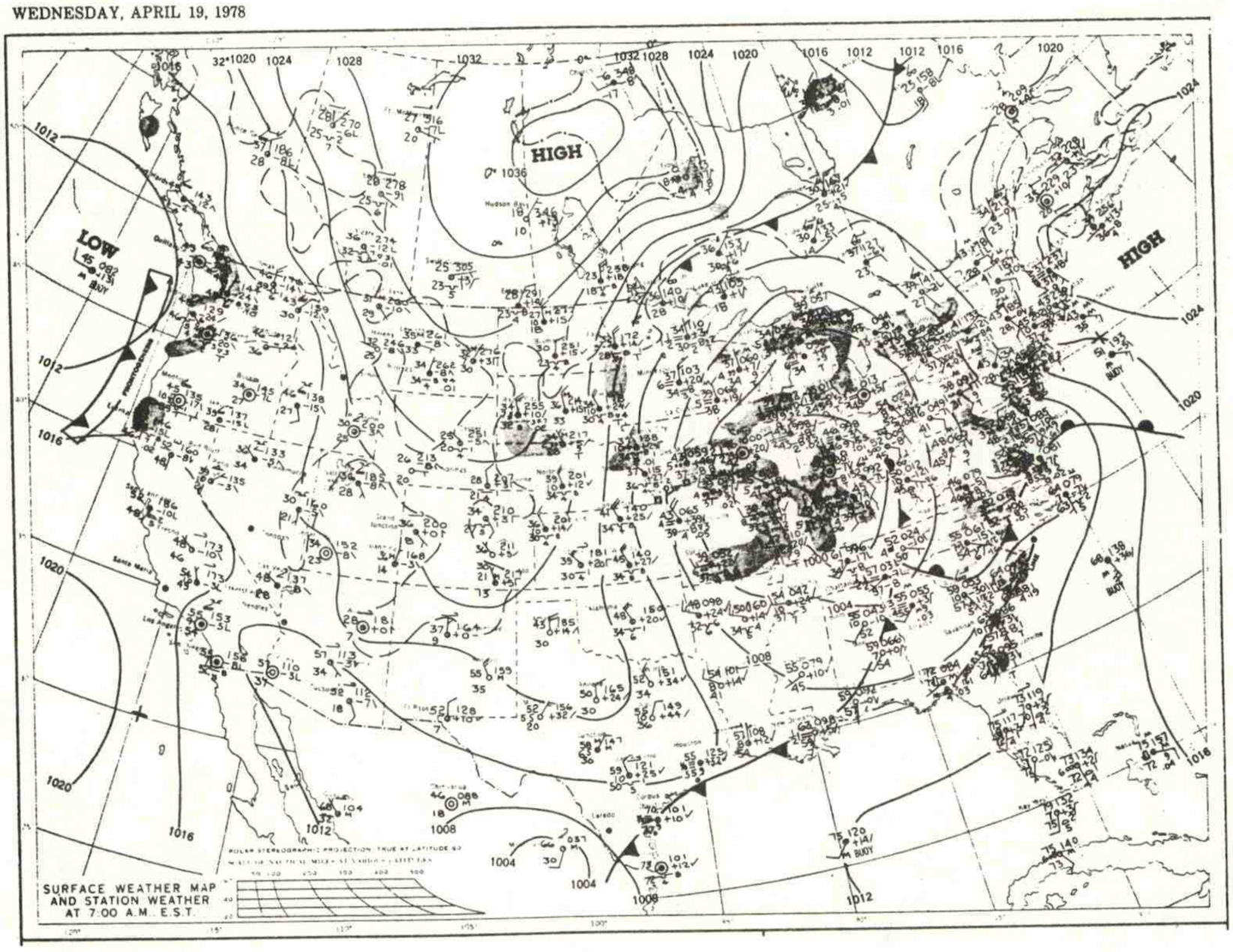
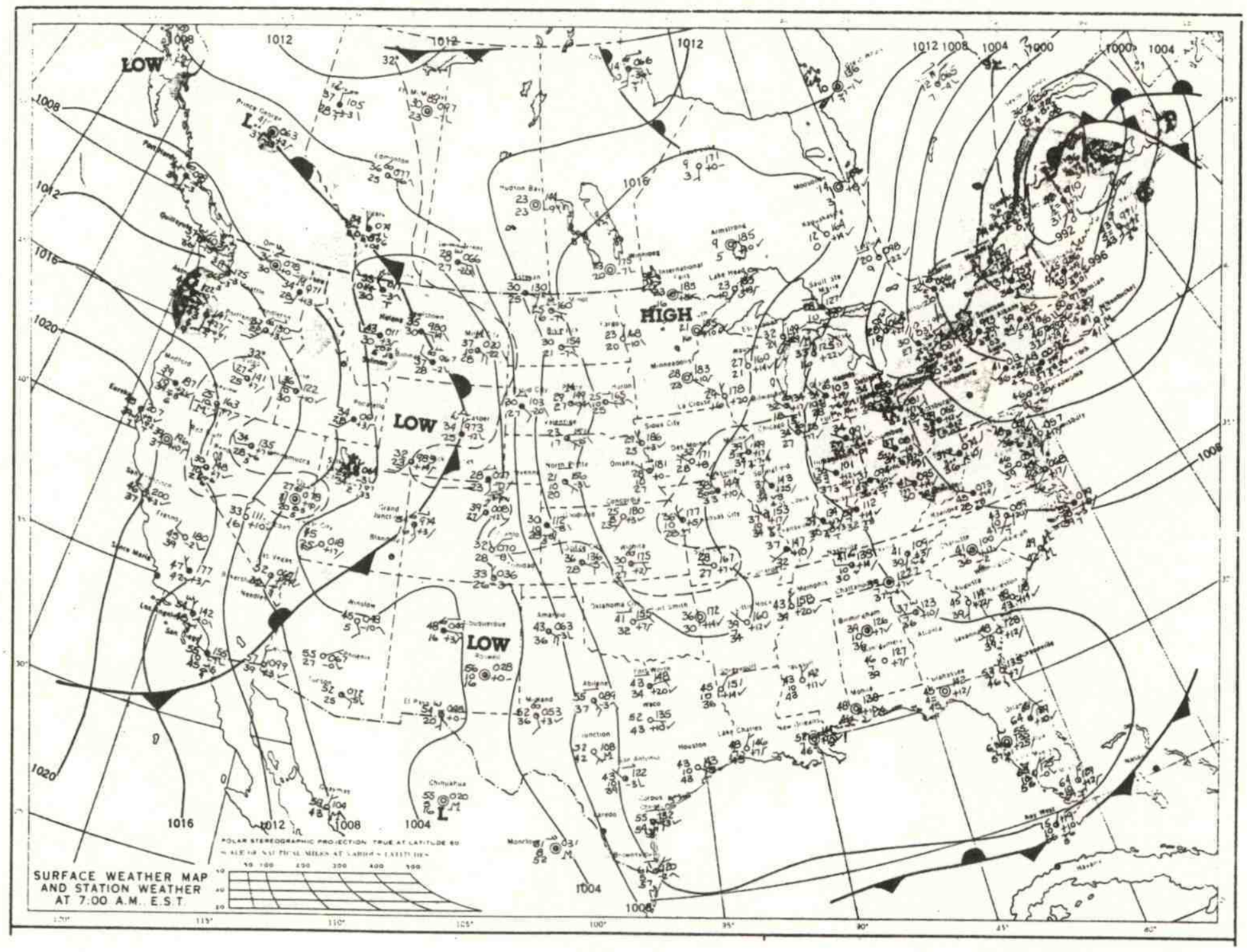


Figure A.1.--National Weather Service maps for 18 and 19 April 1978.

FRIDAY, APRIL 21, 1978



SATURDAY, APRIL 22, 1978

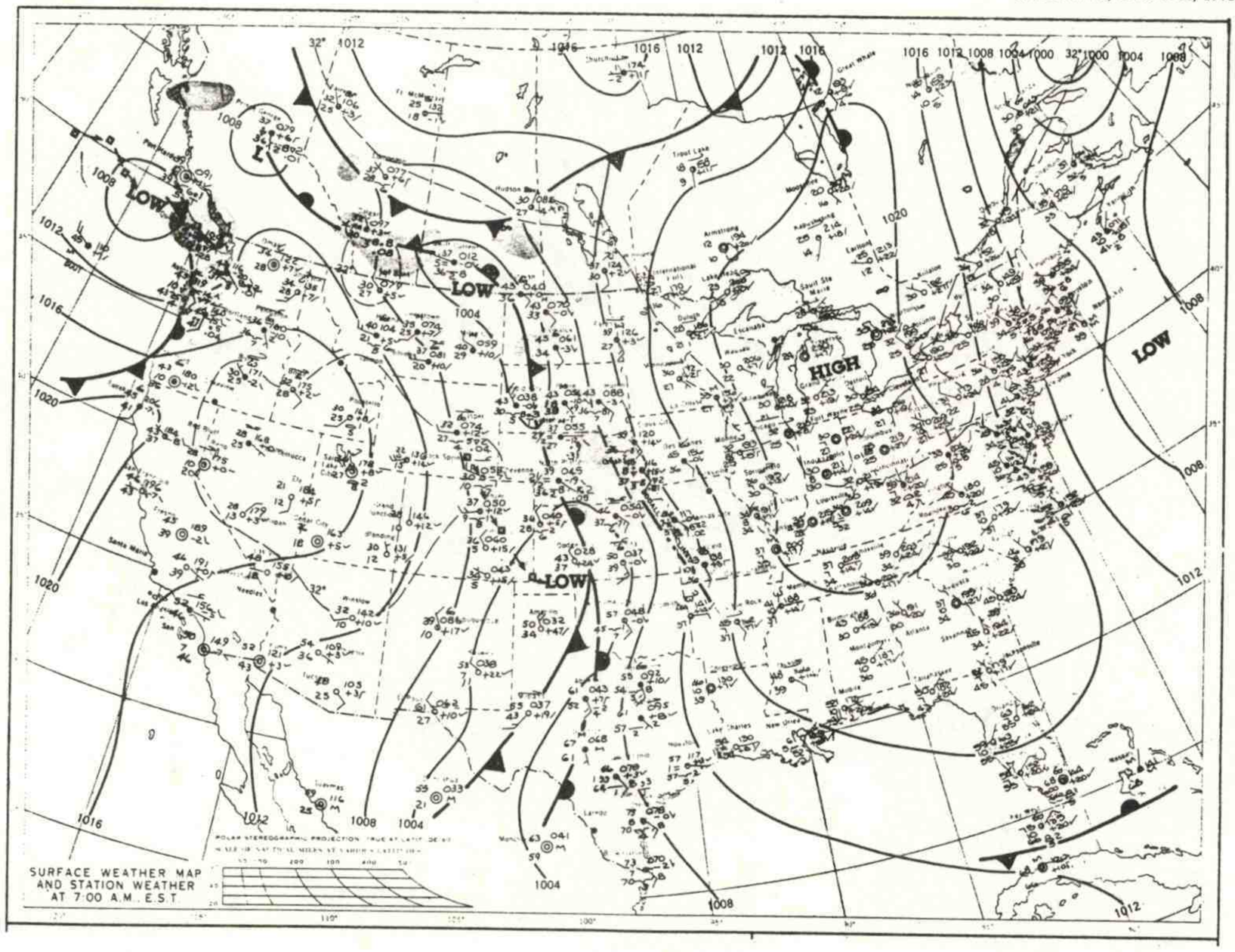
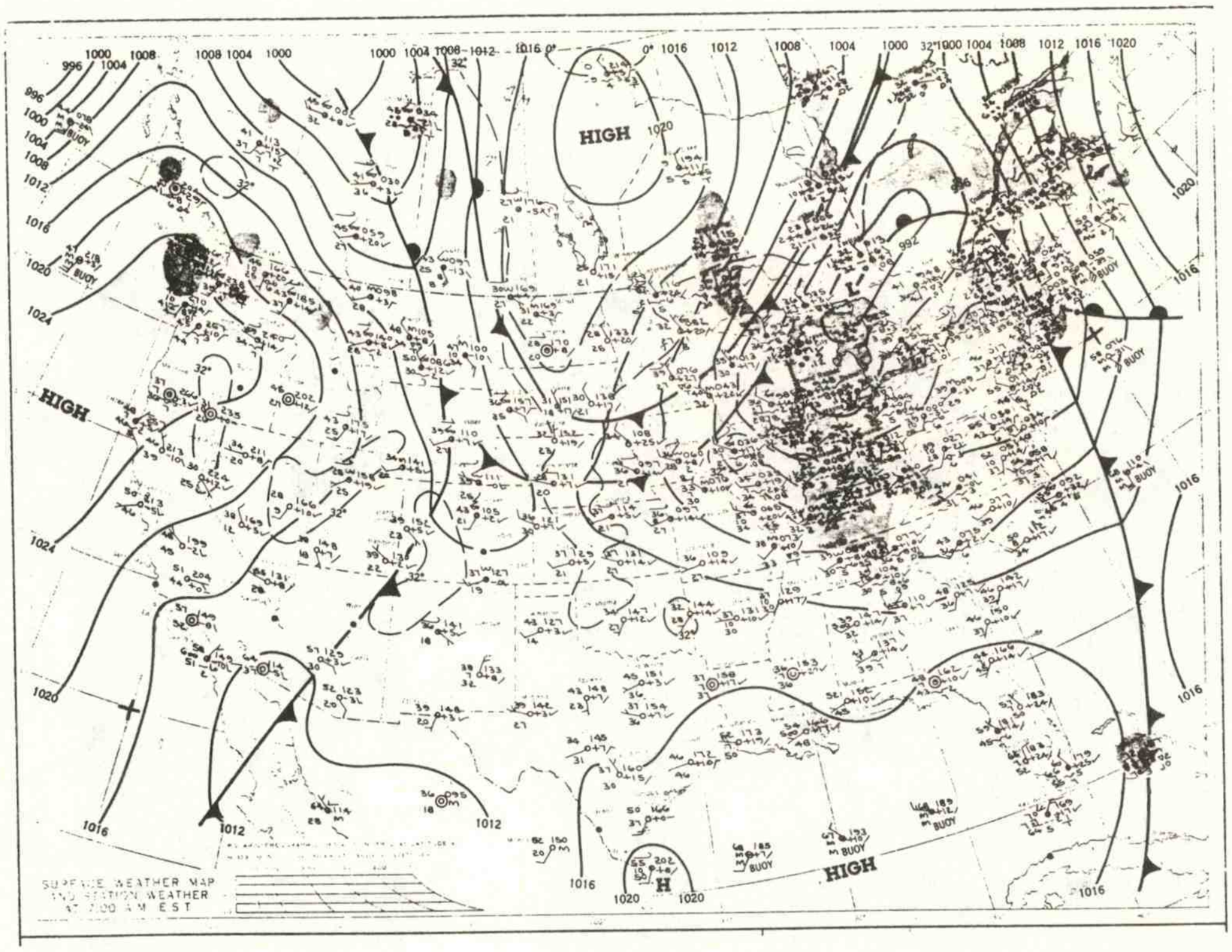


Figure A.2.--National Weather Service maps for 21 and 22 April 1978.



WEDNESDAY, APRIL 16, 1980

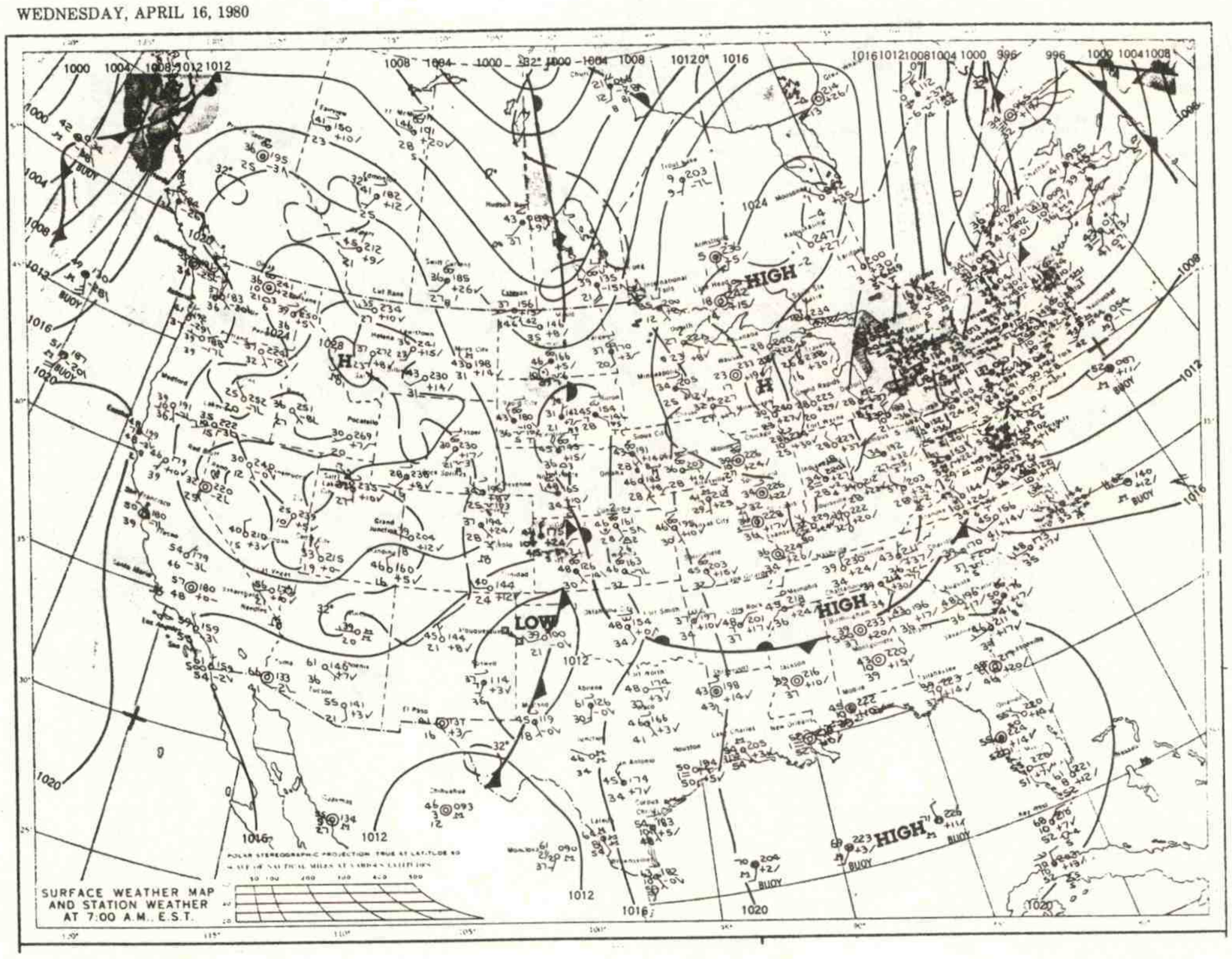


Figure A.3.--National Weather Service maps for 15 and 16 April 1980.

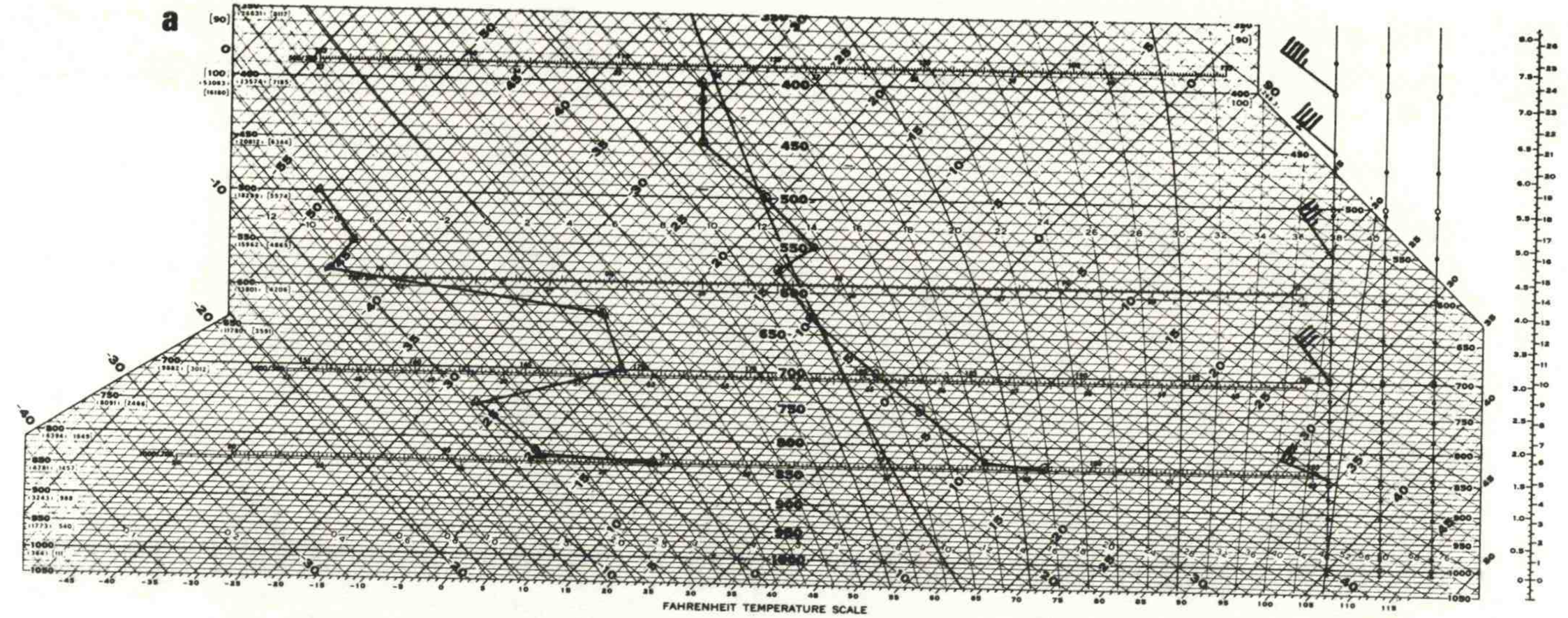


Figure A.4.--Denver upper-air soundings for (a) 1700 MST on 18 April and (b) 0500 MST on 19 April 1978.

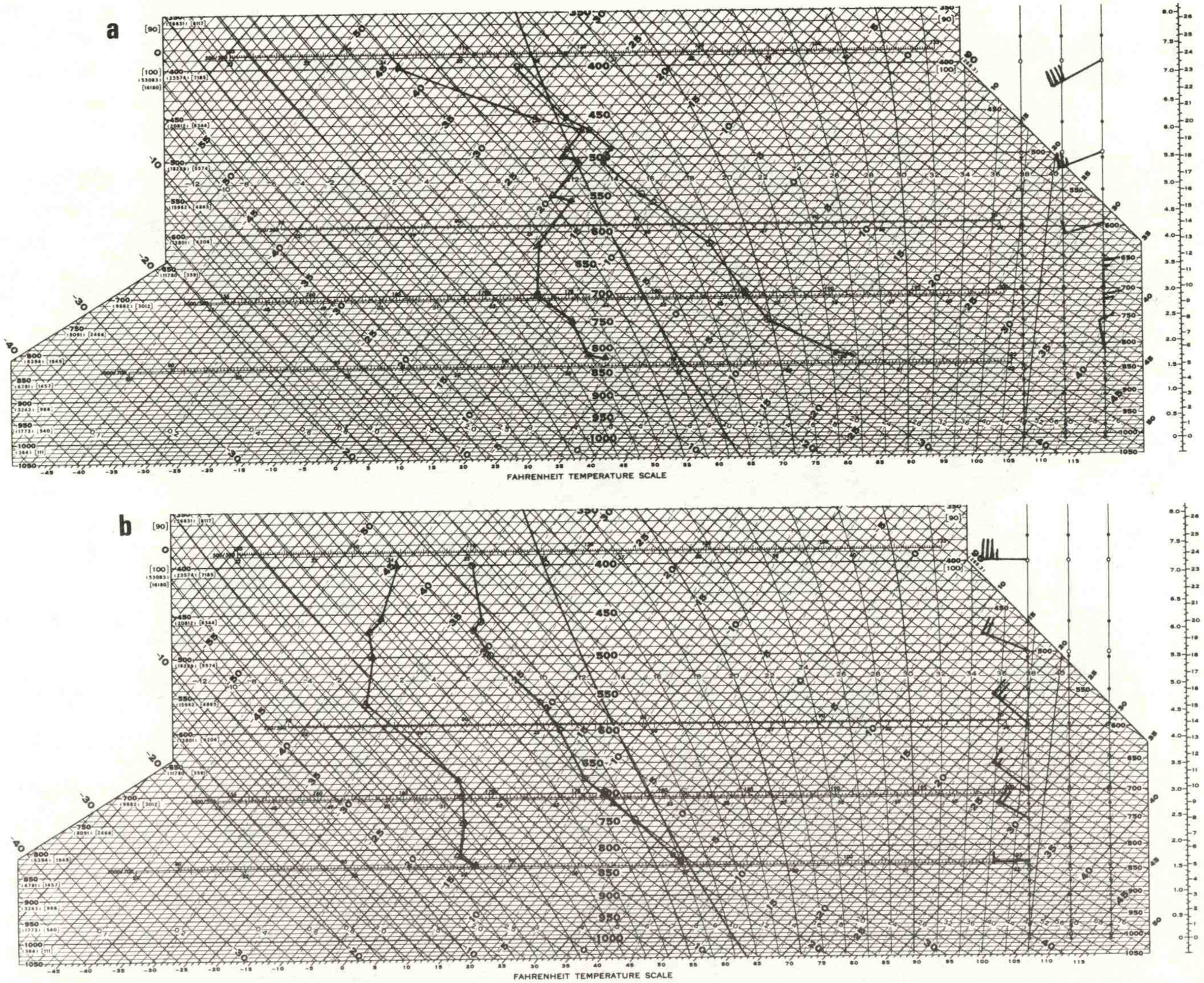


Figure A.5.--Denver upper-air soundings for (a) 1700 MST on 21 April and (b) 0500 MST on 22 April 1978.

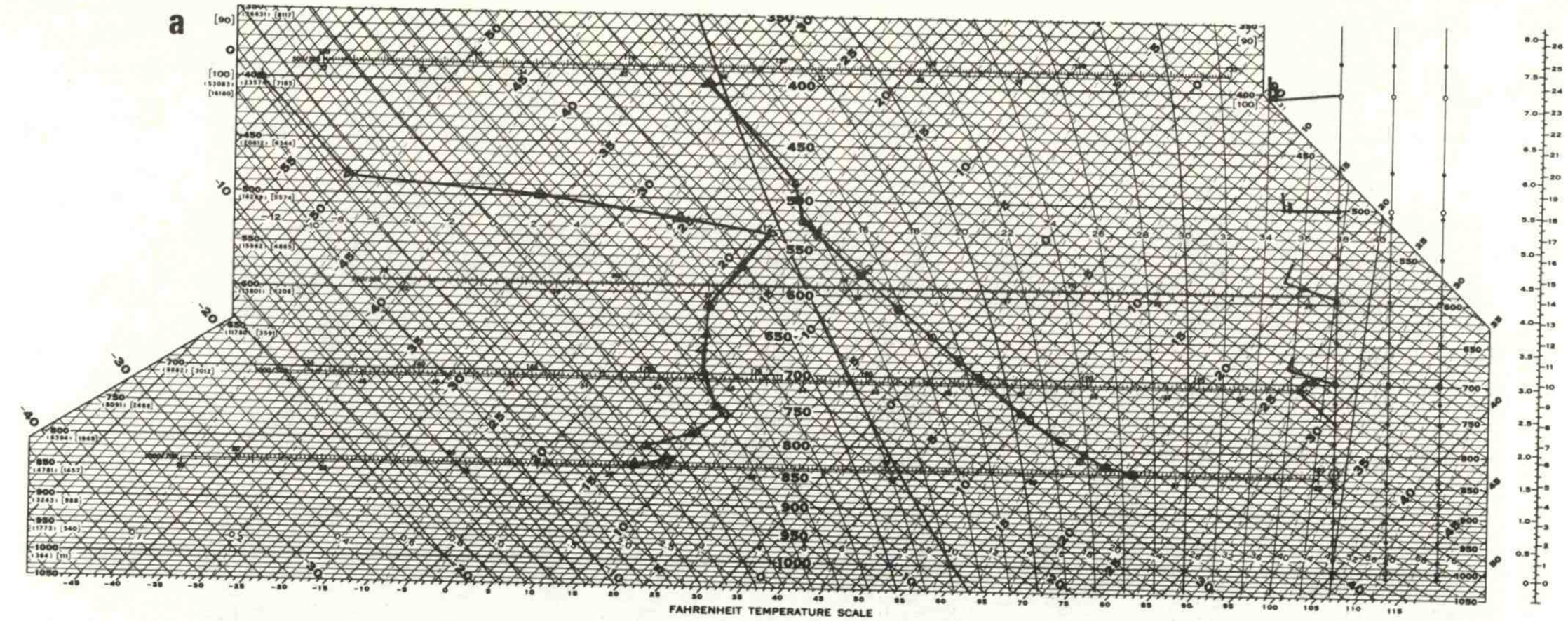


Figure A.6.--Denver upper-air soundings for (a) 1700 MST on 15 April and (b) 0500 MST on 16 April 1980.

Table A.1.--Data summary for 18 April 1978

Period (MST)	z (m)	U (m/s)	A (deg)	T (°C)	T_d (°C)	σ_w^2 (m^2/s^2)	σ_θ^2 ($°C^2$)	$\overline{uw}$ (m^2/s^2)	$\overline{w\theta}$ (°C m/s)	L (m)
2120 to 2140	10	8.06	53	4.46	-2.73	0.343	0.057	-0.173	-0.037	148
	22	9.25	52	4.48	-4.50	0.402	0.041	-0.239	-0.040	250
	50	10.71	53	4.38	-3.25	0.443	0.026	-0.170	-0.026	216
	100	12.41	47	4.00	-2.80	0.451	0.022	-0.300	-0.011	645
	150	12.83	43	3.55	-3.44	0.376	0.020	-0.239	-0.006	---
	200	14.86	44	3.18	-2.92	0.282	0.018	-0.052	-0.005	---
	250	*	*	2.75	-3.51	*	0.017	*	*	---
	300	16.21	36	2.41	-3.46	0.190	0.017	+0.007	-0.009	---
2220 to 2240	10	7.50	49	3.92	-2.51	0.280	0.049	-0.123	-0.026	132
	22	8.70	48	3.96	-4.32	0.341	0.034	-0.143	-0.026	167
	50	10.27	50	3.88	-3.07	0.354	0.022	-0.123	-0.014	256
	100	12.06	45	3.52	-2.52	0.317	0.017	-0.117	-0.017	195
	150	12.13	41	3.08	-3.15	0.275	0.015	-0.190	-0.015	---
	200	14.22	43	2.66	-2.48	0.277	0.015	-0.094	-0.010	---
	250	*	*	2.30	-3.31	*	0.018	*	*	---
	300	16.12	35	1.98	-3.32	0.185	0.026	-0.028	-0.006	---
2300 to 2320	10	1.66	342	2.37	-2.24	0.094	0.051	-0.038	-0.018	33
	22	2.11	349	2.44	-3.88	0.160	0.022	-0.052	-0.014	67
	50	2.30	14	2.26	-2.87	0.245	0.008	-0.091	-0.020	107
	100	4.25	15	1.93	-2.02	0.403	0.006	-0.063	-0.156	81
	150	5.46	23	1.47	-2.63	0.480	0.006	-0.124	-0.008	---
	200	6.69	29	1.14	-1.99	0.507	0.004	-0.078	-0.006	---
	250	*	*	0.67	-2.80	*	0.005	*	*	---
	300	9.00	24	0.28	-2.86	0.564	0.005	-0.201	-0.007	---

Notes: * indicates missing or suspect data
--- parameter not computed

Table A.2.--Data summary for 22 April 1978

Period (MST)	z (m)	U (m/s)	A (deg)	T (°C)	T_d (°C)	σ_w^2 (m^2/s^2)	σ_θ^2 ($°C^2$)	$\overline{uw}$ (m^2/s^2)	$\overline{w\theta}$ (°C m/s)	L (m)
0006 to 0026	10	9.12	253	4.85	-13.07	0.527	0.027	-0.355	-0.024	702
	22	10.83	254	4.84	-15.05	0.478	0.026	-0.308	-0.022	624
	50	12.36	256	4.72	-14.97	0.395	0.026	-0.165	-0.011	488
	100	13.86	259	4.37	-13.42	0.323	0.026	-0.108	-0.011	272
	150	14.34	261	3.97	-14.28	0.364	0.030	-0.125	+0.003	---
	200	*	*	3.58	-13.60	0.416	0.025	*	+0.018	---
	250	*	*	3.15	-13.65	*	0.028	*	*	---
	300	14.13	264	2.73	-15.10	0.601	0.029	+0.308	+0.041	---
0026 to 0046	10	5.92	265	4.34	-12.59	0.265	0.068	-0.175	-0.028	212
	22	7.45	265	4.41	-14.84	0.233	0.048	-0.190	-0.022	299
	50	8.65	265	4.33	-17.36	0.226	0.045	-0.229	-0.026	347
	100	10.03	269	4.04	-12.91	0.297	0.044	-0.394	-0.046	438
	150	10.49	273	3.72	-13.92	0.381	0.036	-0.749	-0.065	---
	200	*	*	3.38	-13.38	0.346	0.019	*	-0.016	---
	250	*	*	2.96	-13.42	*	0.017	*	*	---
	300	11.28	279	2.56	-15.00	0.588	0.024	-0.186	-0.021	---
0046 to 0106	10	3.99	276	4.01	-13.09	0.132	0.148	-0.029	-0.025	16
	22	5.01	276	4.18	-15.13	0.225	0.108	-0.109	-0.037	78
	50	5.94	277	4.15	-19.95	0.359	0.085	-0.047	-0.026	31
	100	7.32	284	3.92	-13.75	0.724	0.076	-0.148	-0.034	135
	150	8.37	287	3.56	-14.72	0.691	0.065	-0.699	-0.055	---
	200	*	*	3.23	-14.12	0.852	0.043	*	-0.043	---
	250	*	*	2.80	-14.07	*	0.037	*	*	---
	300	10.50	284	2.40	-15.72	1.012	0.031	+0.252	-0.032	---

Notes: * indicates missing or suspect data
--- parameter not computed

Table A.3.--Data summary continued for 22 April 1978

Period (MST)	z (m)	U (m/s)	A (deg)	T (°C)	T_d (°C)	σ_w^2 (m^2/s^2)	σ_θ^2 ($°C^2$)	$\overline{uw}$ (m^2/s^2)	$\overline{w\theta}$ (°C m/s)	L (m)
0206 to 0226	10	6.05	286	3.44	-15.13	0.299	0.222	-0.136	-0.005	850
	22	7.64	286	3.74	-15.20	0.394	0.130	-0.203	-0.035	222
	50	8.83	286	3.80	-15.02	0.587	0.070	-0.124	-0.040	89
	100	10.39	287	3.49	-15.55	0.928	0.043	-0.117	-0.032	98
	150	11.32	286	3.06	-16.24	0.900	0.333	-0.603	-0.048	---
	200	*	*	2.63	-15.49	1.310	0.275	*	-0.033	---
	250	*	*	2.19	-15.26	*	0.039	*	*	---
	300	13.24	281	1.76	-16.87	1.576	0.046	-0.054	-0.065	---
0226 to 0246	10	8.12	276	3.10	-14.75	0.409	0.068	-0.223	-0.045	189
	22	9.88	276	3.28	-14.84	0.415	0.051	-0.310	-0.051	276
	50	11.59	277	3.36	-14.61	0.381	0.036	-0.106	-0.026	105
	100	13.53	280	3.15	-15.29	0.396	0.033	-0.161	-0.027	195
	150	14.45	281	2.81	-16.16	0.582	0.022	-0.399	-0.045	---
	200	*	*	2.44	-15.55	0.403	0.016	*	-0.011	---
	250	*	*	2.01	-15.30	*	0.014	*	*	---
	300	15.77	281	1.57	-16.09	0.539	0.012	+0.244	-0.011	---
0246 to 0306	10	7.27	280	2.99	-14.97	0.306	0.069	-0.152	-0.036	133
	22	8.93	281	3.20	-15.02	0.316	0.049	-0.174	-0.040	147
	50	10.41	283	3.30	-14.78	0.268	0.035	-0.078	-0.020	89
	100	12.14	286	3.04	-15.40	0.317	0.030	-0.087	-0.024	86
	150	12.96	28	2.68	-16.19	0.394	0.025	-0.249	-0.029	---
	200	*	*	2.27	-15.48	0.407	0.021	*	-0.011	---
	250	*	*	1.85	-15.20	*	0.019	*	*	---
	300	14.13	285	1.41	-15.64	0.405	0.016	+0.115	-0.003	---

Notes: * indicates missing or suspect data
--- parameter not computed

Table A.4.--Data summary for 15 April 1980

Period (MST)	z (m)	U (m/s)	A (deg)	T (°C)	T_d (°C)	σ_w^2 (m^2/s^2)	σ_θ^2 ($°C^2$)	$\overline{uw}$ (m^2/s^2)	$\overline{w\theta}$ (°C m/s)	L (m)
1700 to 1720	10	6.22	276	17.67	-10.29	0.164	0.084	-0.109	-0.025	123
	22	7.40	276	17.75	-11.34	0.153	0.042	-0.118	-0.021	165
	50	8.50	276	17.67	-12.55	0.172	0.019	-0.102	-0.010	263
	100	9.24	277	17.33	-13.40	0.173	0.058	-0.106	-0.014	208
	150	10.33	278	16.92	-14.05	0.152	0.010	-0.118	-0.007	---
	200	10.77	275	16.49	-15.04	0.135	0.006	-0.060	-0.004	---
	250	10.54	274	16.04	-15.29	0.263	0.006	-0.056	-0.004	---
	300	11.09	273	15.63	-15.43	0.133	0.003	-0.014	-0.005	---
1820 to 1840	10	3.16	303	15.57	- 8.89	0.108	0.084	-0.040	-0.019	36
	22	4.73	297	16.18	- 9.68	0.093	0.060	-0.020	-0.015	16
	50	7.17	290	16.71	-10.46	0.097	0.108	-0.021	-0.007	39
	100	9.31	290	16.96	-12.08	0.066	0.017	+0.020	-0.004	---
	150	9.64	289	16.63	-12.29	0.096	0.007	+0.026	-0.003	---
	200	9.23	285	16.26	-13.26	0.120	0.005	+0.089	-0.003	---
	250	9.15	286	15.78	-13.10	0.228	0.004	+0.133	+0.003	---
	300	8.83	283	15.32	-13.13	0.237	0.005	+0.203	-0.003	---
1900 to 1920	10	4.93	258	14.32	- 7.56	0.067	0.162	-0.022	-0.015	18
	22	6.86	263	15.53	- 8.46	0.079	0.472	+0.036	+0.029	---
	50	8.39	265	16.17	- 9.18	0.072	0.272	-0.060	-0.017	76
	100	8.70	269	16.12	-10.19	0.130	0.170	-0.114	-0.036	89
	150	9.52	275	15.94	-10.08	0.173	0.147	-0.216	-0.039	---
	200	9.87	274	15.74	-11.11	0.153	0.065	-0.214	+0.013	---
	250	10.12	276	15.32	-10.89	0.305	0.062	-0.219	+0.025	---
	300	10.26	272	14.36	-10.67	0.203	0.065	-0.226	+0.027	---

Note: --- parameter not computed

APPENDIX B: VARIANCES AND SCALES OF TEMPERATURE AND VELOCITY FLUCTUATIONS IN THE STABLE BOUNDARY LAYER*

Monin-Obukhov similarity reasoning and measurements over flat terrain show that the mean temperature gradient in stable conditions ($z/L > 0$) is given by

$$d\bar{\theta}/dz = \frac{T_*}{kz}\,(1 + \beta\, z/L), \tag{B.1}$$

where $T_* = -\overline{w\theta}/u_*$, $L = -u_*^3\, T_o/(g\,\overline{w\theta}\,k)$, and k and β are constants (Monin and Yaglom, 1971). Since fluxes are taken as constant in the surface layer, σ_w ($\simeq 1.3\, u_*$) is approximately constant with height, as is $\overline{w\theta}$. T_o is the mean surface temperature. Consequently for similarity,

$$\Gamma_\theta = \sigma_\theta/T_* = \text{constant, when } z/L > 0\ . \tag{B.2}$$

The Kansas data give a range for $\Gamma_\theta \simeq 1.5$ to 2.0 (Wyngaard et al., 1971), whereas Okamoto and Webb (1970) suggest 2.5 to 3.3, whence $\Gamma_{w\theta} = -\overline{w\theta}/\sigma_\theta\sigma_w \simeq 0.35$ (Kansas and Minnesota data, Caughey et al., 1979). The ranges of values of Γ_θ and $\Gamma_{w\theta}$ measured at BAO ($z \leq 22$ m) are 2.9 ± 0.6 and 0.23 ± 0.1.

Given (B.1), we can write (B.2) as a relation between the rms temperature fluctuation σ_θ, the mean temperature gradient $d\bar{\theta}/dz$, and a length scale $L^{(\theta)}$ defined by

$$\sigma_\theta = L^{(\theta)}\, d\bar{\theta}/dz\ , \tag{B.3a}$$

where

$$L^{(\theta)} = \frac{kz}{1 + \beta\, z/L}\,\Gamma_\theta\ . \tag{B.3b}$$

---

* Summary of a yet-to-be-published note by J.C.R. Hunt. It is on the basis of the results presented here that some of the measurements are discussed in the paper. [Some aspects were published by Hunt (1982a).]

So for weak stratification, $L^{(\theta)} = \Gamma_\theta\, kz$, and for strong stratification, where $\beta\, z/L >> 1$,

$$L^{(\theta)} = \frac{\Gamma_\theta\, kL}{\beta} \simeq (0.15 \pm 0.5)\, L\ , \tag{B.3c}$$

if $\beta \simeq 5.4$, as in the Kansas experiments (Busch, 1973). The Monin-Obukhov length scale L can be expressed as

$$L \equiv \left[\frac{u_*^3\, L\, T_o}{g(-\overline{w\theta})k}\right]^{1/2} = \left[\frac{\sigma_w^2\, (u_*/\sigma_w)^2\, \beta}{(g/u_*)(-\overline{w\theta}/T_o)(\beta/kL)k^2}\right]^{1/2}$$

$$= \frac{\sigma_w}{N}\left(\frac{\beta^{1/2}}{0.4 \times 1.3}\right)[1 + 1/(\beta z/L)]^{1/2}\ . \tag{B.4a}$$

Thus for strong stratification,

$$L \simeq 5\, \sigma_w/N \quad \text{for the Kansas value of } \beta. \tag{B.4b}$$

At BAO, $L/(\sigma_w/N)$ varies over the range 3 to 10 for $z \leq 50$ on the strongly stratified days considered here when $z/L > \frac{1}{5}$. Thus (B.3a) becomes for the Kansas data

$$\sigma_\theta \simeq \zeta_\theta(\sigma_w/N)\, d\bar{\theta}/dz\ , \tag{B.5}$$

where ζ_θ varies from 0.5 to 1.0.

The thermal diffusivity parameter $F = K_\theta/(\sigma_w^2/N)$ can also be derived for surface-layer stable turbulence. From (B.1), the coefficient of thermal diffusivity is

$$K_\theta \equiv -\frac{\overline{w\theta}}{d\bar{\theta}/dz} = \frac{ku_*\, z}{1 + \beta\, z/L} = \frac{ku_*\, L}{\beta[1 + 1/(\beta\, z/L)]}\ .$$

Then from (B.4a)

$$F = \frac{K_\theta}{\sigma_w^2/N} = \frac{k(u_*/\sigma_w)}{\beta[1 + 1/(\beta\, z/L)]} \cdot \frac{\sigma_w}{N}\, \frac{\beta^{1/2}}{k(\sigma_w/u_*)}\left[\frac{(1 + 1/\beta\, z/L)^{1/2}}{(1 + \beta\, z/L)^{1/2}}\right]$$

$$F = \frac{\beta^{-1/2}}{(\sigma_w/u_*)^2\ [1 + 1/(\beta\ (z/L)]^{1/2}} \quad . \tag{B.6a}$$

Thence

$$F \simeq \frac{0.3}{[1 + (\sigma_w/N)/z]^{1/2}} \tag{B.6b}$$

when $\beta(z/L) >> 1$, using Kansas data.

APPENDIX C: SCALES OF TEMPERATURE AND VELOCITY FLUCTUATIONS

If in stable conditions in the surface layer there is a local balance of turbulent kinetic energy (TKE) between production, dissipation, and the local flux of buoyancy, then the steady-state TKE equation becomes

$$\varepsilon = \frac{u_*^3}{L_{\varepsilon,u_*}} = u_*^2 \, (dU/dz) - \frac{u_*^3}{kL} \quad , \tag{C.1}$$

which provides a definition for the energy dissipation scale L_{ε,u_*}. Since it is observed that in stable conditions

$$dU/dz = \frac{u_*}{kz} \, (1 + \alpha z/L) \tag{C.2}$$

where $\alpha \simeq 5$ (Monin and Yaglom, 1971), then from (C.1) and (C.2)

$$\varepsilon = \frac{u_*^3}{kz} \, [1 + (\alpha-1)z/L] \tag{C.3a}$$

(Busch, 1973), and

$$L_{\varepsilon,u_*} = \frac{kz}{1 + (\alpha-1)z/L} \quad . \tag{C.3b}$$

The implication of (C.3a) is that for given shear stress u_*^2, or for given w variance σ_w^2, the increase of dissipation with stable stratification is $(\alpha - 1)$, or about 4 times greater than the damping of turbulence by the buoyancy flux. Only if one assumes that the mean horizontal velocity U or mean velocity gradient dU/dz is held constant as z/L increases do the dissipation and turbulence decrease. Most physical discussions of the damping action of stratification are rather vague as to what aspect of the flow is kept constant or determined by boundary conditions when z/L or Ri increases. An explanation for this result is given in Appendix D. [Usually Prandtl's (1952, p. 381) discussion of "balls" of fluid moving vertically influences most qualitative descriptions, though Turner (1973, p. 136) emphasizes that dissipative viscous losses greatly exceed those caused by buoyancy. However, he fails to consider how this dissipation changes with stratification or why it does.] Clearly such an assumption has to be made (implicitly or explicitly) and this then determines which is the dominant physical process.

Observations and physical arguments based on the local nature of small-scale turbulent motion indicate that

$$\varepsilon = C_\varepsilon \, \sigma_w^3 / L_x^{(w)}$$

even in stably stratified boundary layers where C_ε is a coefficient that varies little between different shear flows (see Appendix D). It follows from (C.1) that

$$L_x^{(w)} \simeq C_\varepsilon (\sigma_w/u_*)^3 \, L_{\varepsilon,u_*} \quad , \tag{C.4a}$$

whence from (C.3b)

$$L_x^{(w)} \simeq C_\varepsilon (\sigma_w/u_*)^3 kz/[1 + (\alpha-1)z/L] \quad . \tag{C.4b}$$

If $C_\varepsilon = 0.4$, $\sigma_w/u_* \simeq 1.3$, and $k = 0.4$,

$$L_x^{(w)} \simeq 0.35 \; z/(1 + 4z/L) \; . \tag{C.5}$$

The results in (C.3a) and (C.5), which derive from the observed form of $\phi_m = kz(dU/dz)/u_*$ and the TKE equation, agree well over the range of $0 < z/L < 1.0$ with Kaimal's (1973) Kansas data. (His points at $z/L = 1.5$ and 3.0 do not agree!) This equivalence between L_{ε,u_*} and $L_x^{(w)}$ was an important hypothesis in Townsend's (1958) argument for the critical Richardson number; it certainly seems to be substantiated by Kaimal's data.

The relative scale of temperature fluctuations can also be inferred from observations and the equation for temperature variance $\overline{\theta^2}$ (see Townsend, 1958); viz,

$$-\overline{w\theta} \, \frac{d\bar{\theta}}{dz} + \frac{d}{dz} \, (\overline{w\theta^2}/2) - \varepsilon_\theta \; = 0 \; . \tag{C.6}$$

Then let $\varepsilon_\theta = \sigma_\theta^2 \, u_*/L_{\varepsilon_\theta}$, where L_{ε_θ} is the temperature dissipation scale. As in the TKE equation (C.1), the diffusion term $\frac{d}{dz} \, (\overline{w\theta^2}/2)$ is negligible in the stable surface layer. Since $d\bar{\theta}/dz$ is observed to have the form of (B.1) in

Appendix B, it follows that

$$L_{\varepsilon_\theta} = \frac{\sigma_\theta^2 \; u_* \; \sigma_w}{(\overline{w\theta})^2} \frac{kz}{(1 + \beta \; z/L)} \; . \tag{C.7}$$

From (C.3b) and (C.7) the ratio of temperature to vertical velocity dissipation scales can be estimated as

$$L_{\varepsilon_\theta}/L_{\varepsilon,u_*} \simeq \frac{1}{(\Gamma_{w\theta})^2} \left(\frac{u_*}{\sigma_w}\right) \frac{1 + (\alpha-1) \; z/L}{1 + \beta \; z/L} \; . \tag{C.8}$$

In the Kansas data $\Gamma_{w\theta} \simeq 0.35$, and $\sigma_w/u_* \simeq 1.3$. Assuming that the temperature integral and dissipation scales are related to each other as are the vertical scales, then when $z/L = 0$,

$$\frac{L_x^{(\theta)}}{L_x^{(w)}} \; \frac{L_{\varepsilon_\theta}}{L_{\varepsilon,u_*}} = 6.5 \; , \tag{C.9a}$$

and when $\beta \; z/L >> 1$, since $\beta \simeq 6.4$ (Busch, 1973),

$$L_x^{(\theta)}/L_x^{(w)} \simeq 4.0 \; . \tag{C.9b}$$

In the Kansas measurements $L_x^{(\theta)}/L_w^{(w)} \simeq 8$ when $z/L = 0$ and 3 when $z/L \simeq 1.0$, whereas in the BAO measurements (Kaimal et al., 1982), $L_x^{(\theta)}/L_x^{(w)} \simeq 5$ when $z/L = 0$. These results give some support to the arguments leading to (C.9a) and (C.9b). We conclude that there may be at most a reduction by a factor of 2 in the relative scales of $L_x^{(\theta)}$ and $L_x^{(w)}$ as the stability increases or as z increases in stable conditions.

APPENDIX D: HYPOTHESES CONCERNING INTEGRAL SCALES AND DISSIPATION SCALES IN SLOWLY VARYING TURBULENT FLOWS

The ideas in this Appendix are derived from studies of grid turbulence (near and far from the wall), and of convective and neutral atmospheric boundary layers. Some of the new results are applicable in these other flows as well as in stable boundary layers.

Hypothesis 1

In many turbulent flows it is observed that

$$\varepsilon \simeq C_\varepsilon \, \sigma_w^3 / L_x^{(w)} \quad . \tag{D.1}$$

In turbulent boundary layers, whether stable, neutral, or convective, C_ε varies from 0.4 to 0.6, whereas in grid turbulence $C_\varepsilon \simeq 1.5$. [For some justification see the subsequent analysis as well as Appendix C, and Hunt (1982b), Kaimal (1973), and Townsend (1958).]

Hypothesis 2

In neutral and stable shear flows

$$\sigma_w \simeq a_3 u_* \quad , \quad \text{where} \quad a_3 \simeq 1.3 \tag{D.2}$$

(Townsend, 1976).

The integral scale of $L_x^{(w)}$ is defined in an unconfined stably stratified shear flow by dU/dz, N, and σ_w. A linearized analysis similar to that of Townsend (1976, pp. 46-49) for the rate of growth T^{-1} of a disturbance with wavenumber $\underline{k}$ in such a flow shows that, if $|N/(dU/dz)| \ll 1$,

$$T^{-1} \simeq \chi_1(\underline{k}) \left| dU/dz + \sqrt{(dU/dz)^2 - \chi_2(\underline{k}) \, N^2} \right| \, , \tag{D.3}$$

where the constants χ_1, χ_2 are functions of $\underline{k}$ and hereafter taken to be equal to 1.0.

Weak stable stratification affects turbulent energy only when combined with shear; without shear, laboratory experiments of decaying turbulence show (Britter et al., 1983) that there is little effect until the turbulence is very weak.

If the shear is so small that $|dU/dz| \ll N$, and the turbulence intensity is weak enough that $NL_x^{(w)}/\sigma_w \gtrsim 3$, then the density gradient may directly affect the straining of small eddies by the large eddies, and thence determine ε and $L_x^{(w)}$. Such a situation is likely to occur only above the boundary layer in decaying turbulence or in turbulence maintained by large-scale wave motion. For these reasons, in the boundary layer where $dU/dz \simeq N$ and $NL_x^{(w)}/\sigma_w \lesssim 1$ there appears to be no physical reason why the turbulence scale should be controlled by the local value of N/σ_w. However, when the flux and gradient Richardson numbers are constant, as assumed by Brost and Wyngaard (1978) in their model for the stable boundary layer, $dU/dz \sim N$ and then the local value of σ_w/N is an appropriate scaling for $L_x^{(w)}$.

If the local Richardson number $Ri = N^2/(dU/dz)^2 \lesssim 1/4$, then it follows from (D.3) that the natural local length scale $L_x^{(w)}$ in an unconfined shear flow is given by

$$[L_x^{(w)}]^{-1} \simeq \frac{T^{-1}}{\sigma_w} \simeq \frac{A_1\, dU/dz}{\sigma_w}\left(1 - \frac{\chi_2\, N^2}{4(dU/dz)^2}\right), \qquad (D.4)$$

where A_1 is an unknown constant.

If the turbulence is close to a rigid boundary at $z = 0$, the turbulence scale is reduced in proportion to z (Hunt and Graham, 1978). If the turbulence is far from a boundary and controlled by the overall scale of the flow (e.g., a grid mesh scale L_o or a wake depth L_o or a convective boundary layer scale L_o or the scale of some large-scale wave motion), then L_o is the relevant scale.

Thus combining these suggestions with (D.4) leads to the next hypothesis for boundary layer flows where $Ri \lesssim 1/4$.

Hypothesis 3

$$[L_x^{(w)}]^{-1} \simeq [L_o]^{-1} + \frac{A_S \, dU/dz}{\sigma_w}\left(1 - \frac{N^2}{4(dU/dz)^2}\right) + \frac{A_B}{z} , \qquad (D.5)$$

where A_S and A_B are constants for the shear and "blocking" effects.

From the kinematic theory of shear-free turbulence near a rigid interface (Hunt, 1982; Hunt and Graham, 1978), it can be shown that close to the surface when

$$z/L_o \to 0 \text{ or } [z/L_x^{(w)} \ (z \to \infty)] \to 0, \text{ then } L_x^{(w)} \simeq 1.7 \ z , \qquad (D.6)$$

the factor 1.7 being determined by the experimental constant in Kolmogorov's inertial subrange law. Since in the limit $z/L_o \to 0$ the expression in (D.5) for $[L_x^{(w)}]^{-1}$ equals A_B/z, it follows that

$$A_B \simeq 1/1.7 = 0.6 . \qquad (D.7)$$

The putative constant A_S in (D.5) can be estimated by either of two alternative observations.

(1) The turbulent kinetic equation in a boundary layer and (D.1), (D.2), and (D.5) show that, where $z/L_o \ll 1$,

$$\varepsilon = \frac{u_*^3}{kz} = C_\varepsilon \, \sigma_w^3 \left(\frac{A_S \, dU/dz}{\sigma_w} + \frac{A_B}{z}\right). \qquad (D.8)$$

Since it is observed that

$$\frac{dU}{dz} = \frac{u_*}{kz}(1 + \alpha z/L) , \qquad (D.9)$$

where $\alpha \simeq 5$ (Monin and Yaglom, 1971), then combining (D.2), (D.8), and (D.9), when $z/L \gg 1$, gives

$$A_S = k \, a_3 \left(\frac{a_3^{-3}}{C_\varepsilon \, k} - A_B\right) \simeq 0.7 \text{ if } C_\varepsilon \simeq 0.6 \qquad (D.10a)$$

$$\simeq 1.2 \text{ if } C_\varepsilon \simeq 0.4 . \qquad (D.10b)$$

(2) Alternatively, the value of A_S can be fixed by comparing the expression for $L_x^{(w)}$ in (D.5) when $z/L_o \ll 1$ with the observation that in a neutral boundary layer $L_x^{(w)} \simeq (0.4 \pm 0.1)z$ (Hunt and Weber, 1979). In that case,

$$A_S \simeq 1.3 \times 0.4 \times [(2.5 \pm 0.5) - 0.6] \qquad \text{(D.11)}$$

$$\simeq 1.0 \pm 0.25 \ .$$

Thus either method gives roughly equivalent values of A_S. On the other hand, if $C_\varepsilon \simeq 0.6$, and A_S is fixed by the first alternative, then (D.5) provides a prediction that in a neutral SBL

$$L_x^{(w)}/z \simeq 0.5 \ .$$

The physical implication is that in a neutral boundary layer $L_x^{(w)}$ is really determined by two comparable effects--the local shear and the wall proximity effect.

A second important prediction can be made by substituting the value of the "constant" A_S into the turbulent kinetic energy equation (C.1) for conditions near the ground when there is significant stable stratification, i.e., $z/L > 0$. Then from (C.1), (D.1), (D.5), and (D.9)

$$u_*^2 \frac{dU}{dz} - \frac{u_*^3}{kL} = C_\varepsilon \sigma_w^3 \left[\frac{A_S \, dU/dz}{\sigma_w} \left(1 - \frac{N^2}{4(dU/dz)^2} \right) + \frac{A_B}{z} \right] ,$$

so

$$\frac{dU}{dz} = \frac{u_*}{\tilde{k}z} \frac{(1 + \tilde{\alpha}z/L)}{1 + \left(A_S \, a_3^3 C_\varepsilon/4 \right) \left(\frac{N^2}{(dU/dz)^2} \right)}$$

$$\simeq \frac{u_*}{\tilde{k}z} [1 + (\tilde{\alpha} - A_S \, a_3^3 C_\varepsilon/4) z/L] \ , \qquad \text{(D.12)}$$

where

$$\tilde{k} = \frac{1 - A_S \, a_3^2 \, C_\varepsilon}{C_\varepsilon \, \sigma_w^3 \, B} \quad \text{and} \quad \tilde{\alpha} = \frac{1}{A_B \, \tilde{k} \, C_\varepsilon \, a_3^3} \ . \qquad \text{(D.13)}$$

Note that when $\tilde{\alpha}z/L \gg 1$, $z/L \gg N^2/(dU/dz)^2$, so $dU/dz \simeq \frac{u_*}{\tilde{k}z} (1 + \tilde{\alpha}z/L)$. Since A_S is chosen to agree with the measurements of the neutral case, $\tilde{k} = k = 0.4$,

but $\tilde{\alpha}$ is not fixed. However by these arguments $\tilde{\alpha}$ is found to be 3.2. Experiments over flat ground give a value of α equal to about 5, which is certainly of the same order of magnitude.

We see in Appendix B that when a stable stratification is applied to a turbulent boundary layer, the increase in viscous dissipation is a factor (α-1) times as great as the loss of energy caused by the buoyancy flux. We can now see that this must be so. For given u_* or σ_w, the generation of a small buoyancy flux δB must require an increased energy input by an increased shear $\delta(dU/dz)$. If this were the only balance to be made, then $\delta(dU/dz) = \delta B/u_*^2$. But an increase of $\delta(dU/dz)$ reduces the integral scale $L_x^{(w)}$ and increases the dissipation by about $0.7\ u_*^2\ \delta(dU/dz)$. Thus only 30% (by our calculation) of the increased shear can be used to balance the buoyancy flux. Only by realizing the relative sensitivity of $L_x^{(w)}$ to both dU/dz and z^{-1} can this point be appreciated. If $L_x^{(w)}$ is assumed to be entirely controlled by the distance from the surface, then an alternative explanation would have to be sought for the observed sensitivity of ε to z/L. Since the turbulent structure at scales less than $L_x^{(w)}$ is not measurably affected by stable stratification, there is no evidence for any other explanation. [The same effects are found in free shear layers where about 70% to 80% of the energy of Kelvin-Helmholtz billows is dissipated, the rest providing a buoyancy flux (Sherman et al., 1978); perhaps the same explanation is appropriate.]

As a third prediction, the hypothesis (D.5) and the observation (D.9) imply that when $\alpha z/L \gg 1$, $dU/dz = \alpha u_*/(0.4L)$, and that

$$[L_x^{(w)}]^{-1} \simeq 0.7\ \frac{dU/dz}{\sigma_w} + \frac{1}{z} \qquad \text{(D.14)}$$

or

$$[L_x^{(w)}]^{-1} \simeq \frac{6 \times 0.7}{0.4 \times 1.3}\ \frac{1}{L}$$

or

$$L_x^{(w)} \simeq 0.12\ L \simeq 0.55\ \sigma_w/N\ , \qquad \text{(D.15)}$$

in approximate agreement with the observations (C.5) and (B.4b).

Thus, given the more general turbulence hypotheses (D.1), (D.2), and (D.5), we have found that in strongly stable conditions $L_x^{(w)}$ must be proportional to

L and σ_w/N near the surface, a result otherwise only deducible from the kind of Monin-Obukhov similarity and dimensional arguments used in Appendix B.

In boundary layers with strong stable stratification, Brost and Wyngaard (1978) argued that on physical grounds σ_w/N and z are the two scales that determine L_{ε,u_*}, so by interpolating from the outer edge of the boundary layer to the layer nearest the surface, they postulated that

$$[L_{\varepsilon,u_*}]^{-1} = N/\sigma_w + z^{-1} \quad . \tag{D.16}$$

This result is consistent with the arguments and results presented here when the stratification is <u>strong</u> and at the outer edge of the boundary layer (even when the Richardson number is not constant). When the stratification is <u>weak</u>, (i.e., $L_x^{(w)}\ N/\sigma_w \lesssim 1$) we are suggesting on the basis of theoretical arguments, and surface-layer and BAO observations, that (D.16) is not the appropriate scaling, even in boundary layers. The more general scaling suggested here is appropriate.

2. WAVE AND TURBULENCE STRUCTURE IN A DISTURBED NOCTURNAL INVERSION

Lu Nai-ping
Institute of Atmospheric Physics
Academia Sinica
Beijing, China

W.D. Neff and J.C. Kaimal
NOAA/ERL/Wave Propagation Laboratory
Boulder, Colorado 80303

ABSTRACT. Acoustic sounder and tower data obtained at the Boulder Atmospheric Observatory (BAO) are used to examine several features of the wave and turbulence structure associated with a disturbed nocturnal inversion. General features, including mean fields and Richardson number, for the case selected for this study are presented. Spectral analysis of the tower data reveals a separation of energy into wavelike and turbulent fluctuations. Analysis of the heat flux, however, shows upward counter-gradient fluxes in the vicinity of a low-level jet and near the top of the inversion. Co-spectral analysis shows that the major contribution to the upward heat flux occurs at frequencies that would normally be considered characteristic of waves. In some cases, the upward flux is associated with a phase shift between vertical velocity w and fluctuating temperature θ different from the quadrature relation that would be expected of internal waves. Time series analysis reveals that these unexpected positive fluxes occur in relatively short bursts. Analysis of time series of θ and w in other cases, as well as inspection of acoustic sounder records, shows that sometimes such upward fluxes can result from a combination of wave motion and horizontal temperature advection. In this case the advection is associated with a shallow cold front.

2.1 INTRODUCTION

Remote-sensing devices using microwaves or acoustic waves have often been used to provide visual documentation for special case studies of waves and turbulence within the nocturnal inversion layer (e.g., Gossard et al., 1970; Emmanuel et al., 1972; Merrill, 1977; Einaudi and Finnigan, 1981). Whereas many of the details of such events are well understood, the data on which such analyses are often based arise from idealized circumstances (such as situations with nearly monochromatic internal waves). More commonly, the nocturnal

inversion as seen by remote-sensing devices reveals a complex mixture of waves, instabilities, and turbulence. Often, the complexity of the inversion seems to be related to particular synoptic situations as noted by Zhou Ming-yu et al. (1980) and Neff (1980). The acoustic sounder and the sensors on the 300-m tower at the Boulder Atmospheric Observatory (BAO), operating almost continuously over the last 4 years, provide the data base needed to relate typical patterns in nocturnal inversion development to synoptic and mesoscale events.

One event that occurs frequently in winter at BAO is the passage of a shallow cold front. Using data from BAO, we present a case study of one such event. We will first describe the meteorological setting, the general features of the low-level front, and the complexity of the waves, turbulence, and advective processes that are present. We will then outline the spectral characteristics of the turbulence and waves followed by detailed interpretation of the features contributing to an anomalous counter-gradient heat flux that appears in a conventional 20-min covariance of w (vertical velocity) and θ (fluctuating temperature).

2.2 SITE CHARACTERISTICS AND INSTRUMENTATION

BAO is located about 30 km north of Denver and 30 km east of the foothills of the Rocky Mountains. This site, on the high plains of Colorado, is characterized by gentle slopes (Kaimal et al., 1982); at the time of the present study, the ground cover consisted of areas of wheat stubble mixed with bare areas planted with winter wheat.

The tower instrumentation at BAO has been described in some detail by Kaimal and Gaynor (1983). Briefly, the tower is instrumented at eight levels (10, 22, 50, 100, 150, 200, 250, and 300 m) with three-axis sonic anemometers, propeller-vane anemometers, fast-response platinum wire and slow-response quartz thermometers, and a cooled-mirror dewpoint hygrometer. A network of five sensitive microbarographs, measuring pressure fluctuations p, is centered about the tower to detect the phase speed and direction of internal waves propagating across the site. Two acoustic sounders were used: one close to the

tower with a 340-m vertical range, and a second about 600 m away with an 850-m vertical range.

Data from the tower and the microbarographs are transmitted via phone line to the central data archiving computer system in Boulder. Standard system programs are used to compute fluxes, variances, and 20-min spectra in real time. Post-processing programs are available to compute spectra as well as cospectra and quadrature spectra over 80- or 160-min periods. A special "beamsteering" program (Kaimal and Gaynor, 1983) is used to calculate wave phase speeds and directions from the microbarograph array. This program has provisions for filtering time series of tower data in any specified spectral interval with varying passbands and cutoff frequencies.

2.3 GENERAL DESCRIPTION OF CASE STUDY

2.3.1 Meteorological Situation

The events under consideration here occurred on the morning of 27 March 1981. Earlier in the evening, the development of the nocturnal inversion had followed an uneventful course in response to surface cooling. Winds aloft were from south-southwest reflecting the presence of a cutoff low centered over southwestern Nevada. The combined circulation of the associated surface low- and a surface high-pressure system located over the Great Lakes maintained southeasterly surface flow over the eastern plains of Colorado. A surface low over central Wyoming meanwhile formed and moved in a southerly direction along the Continental Divide and by 0500 MST on 27 March was located south of Denver. The 0500 MST rawinsonde ascent made by the National Weather Service at Denver showed a surface-based inversion capped by a weak isothermal layer that extended from 800 to 700 mb. The winds were light and variable from the surface to 700 mb, above which the winds abruptly increased to 18 m/s from the southwest. While the relatively coarse rawinsonde network revealed little complexity in the flow, acoustic sounder and tower data at BAO showed an abrupt change in the nocturnal inversion shortly after midnight. As shown in the next section, winds at the top of the tower became light from the west

while in the lower half of the tower a 10-m/s jet developed, blowing from north-northeast. Associated with this wind shift were a drop of about 3°C in temperature and a sudden decrease in surface pressure of about 0.5 mb. Measurement of the wave and turbulence properties associated with this unsteady jet will be of primary interest here.

2.3.2 Acoustic Sounder and Mean Flow Data

Figure 2.1 shows the nocturnal inversion, as seen by the acoustic sounder, during the period from midnight to 0800 MST. Three distinct periods can be noted. The first is the initial transition period between midnight and 0100 MST when a north-northeast jet first appears. The second is between 0330 and 0400 MST when the inversion is strongly disturbed. The third is after 0600 MST, just before the onset of convection, when the inversion height is relatively stationary.

The intensity of the echoes depicted in Fig. 2.1 is a function of the strength of the temperature fluctuations. Explicitly, the scattering cross section is proportional to (Neff, 1980)

$$\left[\left(\frac{Ri}{\frac{K_M}{K_H} - Ri}\right)^{1/3} K_H^{2/3}\right]\left[\frac{\partial\Theta}{\partial z}\right]^{5/3} . \qquad (2.1)$$

The first term in brackets measures the strength of the turbulence, where K_H is the eddy diffusion coefficient for heat, K_M is the coefficient for momentum, and Ri is the gradient Richardson number. With a given mean potential temperature (Θ) profile, the distribution of turbulence is a significant factor in the echo patterns seen in the acoustic backscatter. Results from Neff (1980) also suggest that the distribution of wind shear, in turn, is the most significant factor determining the distribution of turbulence. These conclusions are illustrated fairly clearly in Figs. 2.2 and 2.3. Figure 2.2 shows the wind and temperature fields as well as isopleths of Ri calculated using data from fixed levels of the tower. The most notable feature of these figures is the presence of two scattering layers: one near the ground, the

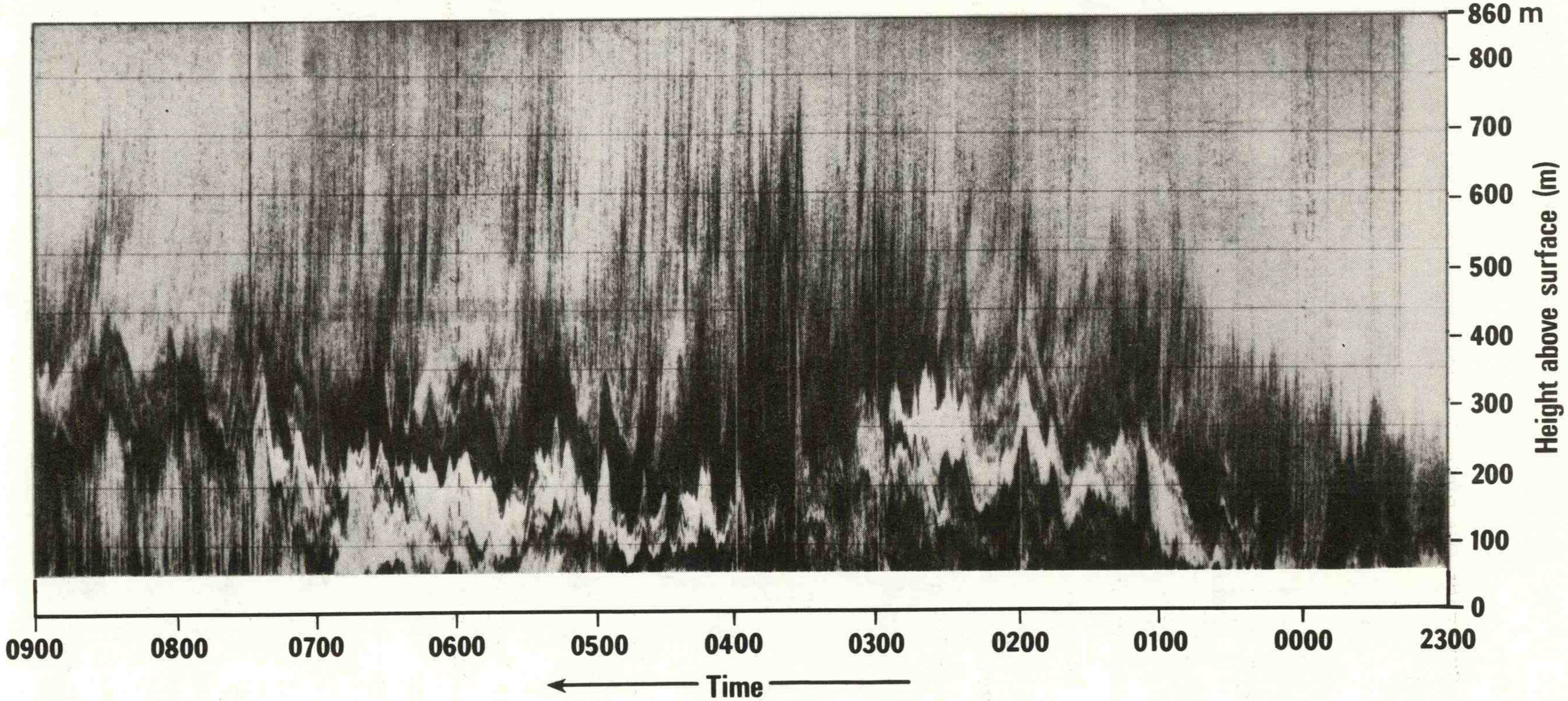


Figure 2.1.--Acoustic sounder record for 2300 MST on 26 March to 0900 MST on 27 March 1981 from a site some 600 m south of the tower. Maximum range is 850 m.

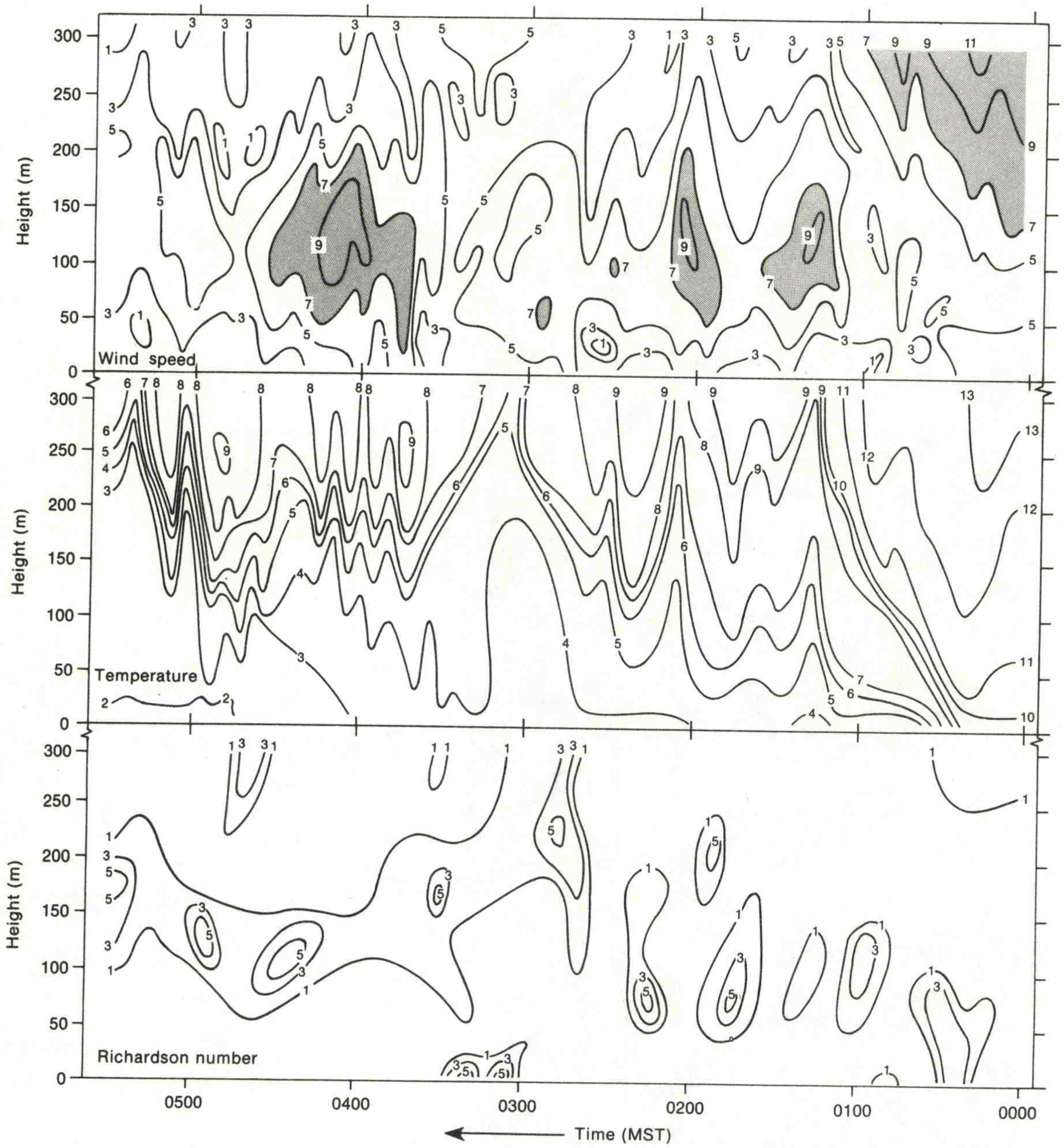


Figure 2.2.--Isopleths of wind speed, temperature, and Ri developed from tower fixed-level data for 0000-0540 MST, 27 March 1981. (Wind speeds are in meters per second, and temperatures are in degrees Celsius.)

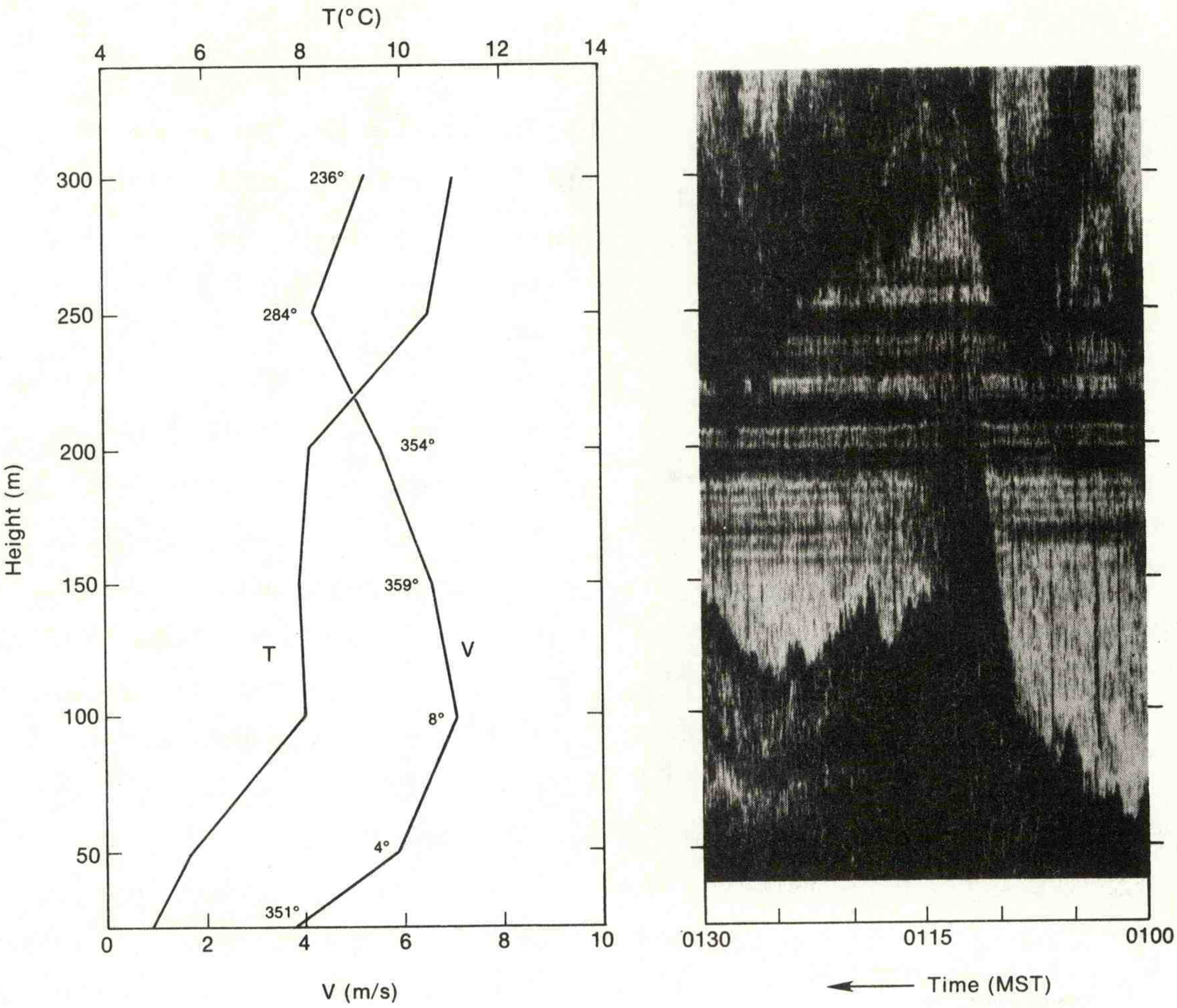


Figure 2.3.--Tower wind and temperature profiles averaged over 5 min frc 0105 to 0110 MST compared with the acoustic sounder record from 0100 to 0130 MST obtained at a site just 160 m north of the tower. The dark, horizontal bands correspond to reflections from the tower.

second elevated above a clear echo region on the record. Comparison of Figs. 2.1 and 2.2 indicates that the clear region is characterized by large values of Ri. This can also be seen in a detailed comparison between the sounder record and the tower wind and temperature profiles as shown in Fig. 2.3. Within the resolution permitted by the 50-m spacing of fixed tower levels, the non-echo region is closely associated with the maximum of the low-level jet where the shear is the least. The elevated scattering layer appears to be connected with the region of increased shear and stability above the jet. In accord with Eq. (2.1), the strongest scattering occurs in layers of largest potential temperature gradient.

2.3.3 Internal Wave Behavior

Of interest throughout the event shown in Fig. 2.1 are the oscillations with periods of several minutes at the height of the inversion base capping the low-level jet. Analysis of the microbarograph data from the array surrounding the tower shows waves of several frequencies propagating from a generally southwesterly direction at speeds from 6 to 22 m/s.

To determine the characteristics of these waves, we used the BAO beam-steering program to calculate wave phase speed, direction, and coherence as a function of frequency. This program requires an 80-min time series. Because waves of a particular frequency may occur only over a short period of time, we incremented the starting time of the calculation by 20 min. We found that prior to 0300 MST, only one wave component dominated for each 80-min calculation; that at the time of frontal passage, the wave phase speed increased markedly; and that after 0300 MST, many waves of different speeds and directions were present. These results are shown graphically in Fig. 2.4, where data are plotted at the center time of each period and the vertical bars represent the range of significant wave speeds and directions found. This broadening of the wave spectrum coincides with the large disturbance in the inversion shortly after 0300 MST as seen in Fig. 2.1.

Since the direction of propagation of these waves is opposed or perpendicular to the low-level flow, it may be that the waves originated from a critical level aloft. The most likely region, determined from the 0500 MST rawinsonde launched from Denver, is at 2 km where, in a strongly sheared region, the winds increase from less than 1 m/s to nearly 18 m/s. This seems a reasonable conclusion based on the work of Keliher (1975) who studied the correlation of surface-measured waves with jet-stream velocities and directions. Atkinson (1981) suggests, though, that although a low-level inversion may amplify surface pressure fluctuations, wavelengths less than 5 km at tropopause level are unlikely to be associated with surface pressure fluctuations. Prior to 0300 MST, the dominant wave period was about 15 min; afterwards wave periods ranged from 4 to 15 min. On the basis of the wave phase speeds in Fig. 2.4 after 0300 MST, only the long-period oscillations in the inversion, from 10 to 20 min in length, are likely to be associated with an

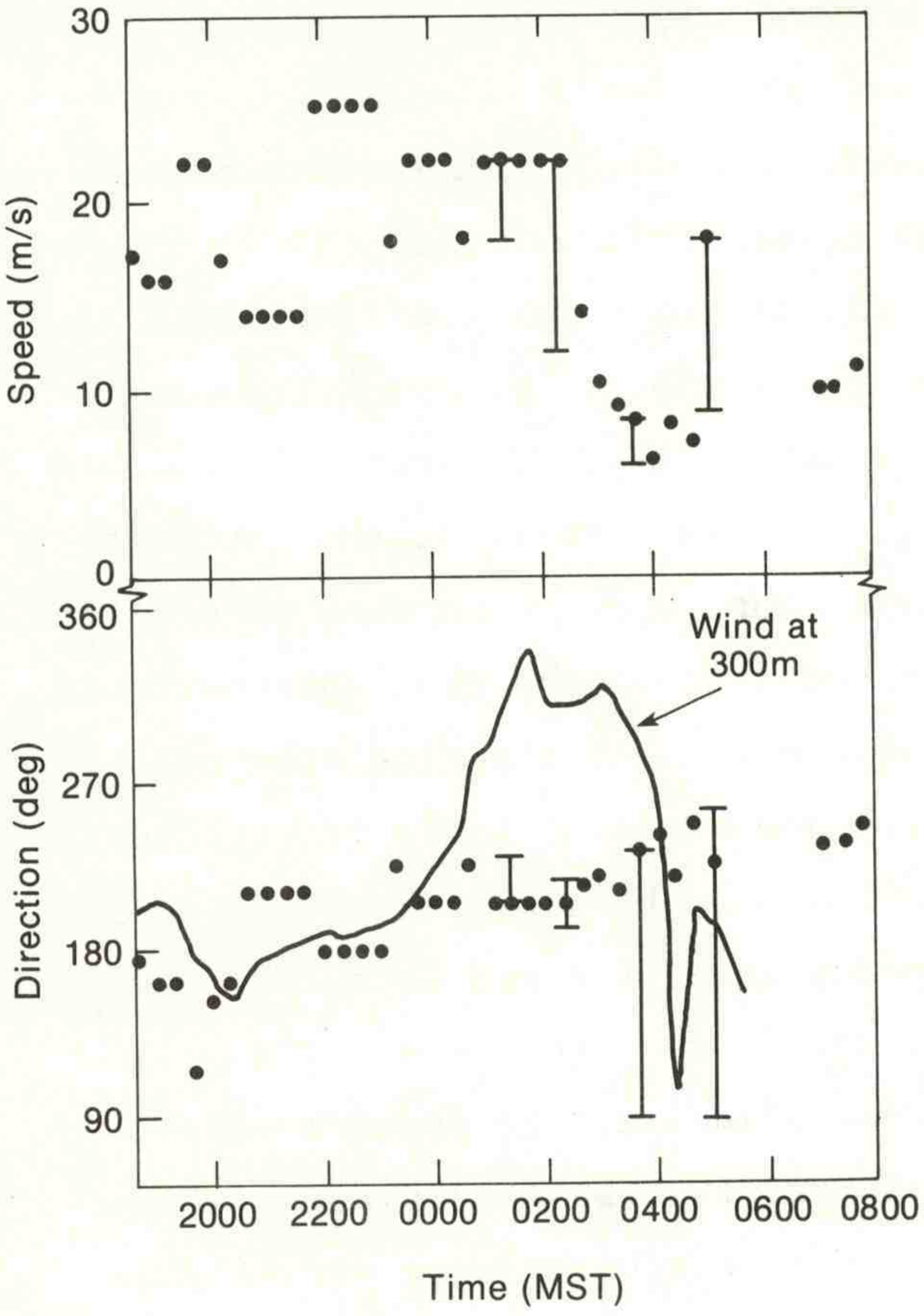


Figure 2.4.--Wave phase speed and direction calculated at 20-min intervals from 1900 MST on 26 March to 0800 MST on 27 March 1981. Calculation is in overlapping 80-min segments. Vertical bars represent the range of significant wave speeds and directions.

upper-level source. The origin of the shorter period waves is not determined although one might speculate that they could be an artifact of the frontal disturbance and/or its interaction with the foothills of the Rocky Mountains some 30 km to the west.

2.4 SPECTRAL ANALYSIS

2.4.1 Spectra Under Steady Conditions

The evidence of waves in both the microbarograph and acoustic sounder data prompted a closer examination of the tower wind and temperature data by spectral techniques. The first period chosen for this analysis was one with a fairly constant inversion height, just before the onset of convection.

A number of authors have discussed spectra under stable conditions. Steward (1969) pointed out some of the difficulties of distinguishing rigorously between waves and turbulence. However, a number of subsequent papers (Axford, 1971; Kaimal, 1973; Caughey and Reading, 1975; Caughey, 1977; Caughey et al., 1979) have shown that in the analysis of power spectra there is often a clear separation into wavelike and turbulent regions. Figure 2.5 presents such results from data taken between 0620 and 0720 MST, 27 March. These data show a clear spectral gap at about 10^{-2} Hz. In the w spectra, the gap is much less noticeable near the ground, primarily because w must approach zero at the surface. The high-frequency portion of the spectra follow the characteristic -2/3 power law. Cross-spectra at 250 m for the same time period show an abrupt change in spectral slope at 10^{-2} Hz. The slope at lower frequencies is almost -5; the slope at higher frequencies tends to be a bit less than -4/3 predicted from surface layer similarity theory (Wyngaard and Coté, 1972).

Integrating the wavelike and turbulent portions of the spectra separately, we get the results in Table 2.1. Here it can be seen that the low-frequency portion of the spectra and cospectra contributes more strongly to the variances and covariances than the high frequency portion does.

Table 2.1--Ratios of low-frequency (L) to high-frequency turbulent (H) contributions to standard deviations and covariances during the period (0620-0720 MST, 27 March 1981)

z (m)	$\frac{(\sigma_\theta)_L}{(\sigma_\theta)_H}$	$\frac{(\sigma_u)_L}{(\sigma_u)_H}$	$\frac{(\sigma_v)_L}{(\sigma_v)_H}$	$\frac{(\sigma_w)_L}{(\sigma_w)_H}$	$\frac{(\overline{w\theta})_L}{(\overline{w\theta})_H}$	$\frac{(\overline{wu})_L}{(\overline{wu})_H}$	$\frac{(\overline{wv})_L}{(\overline{wv})_H}$
10-100	8.9	9.0	13.0	0.4	3.1	2.6	6.2
150-300	13.0	22.7	21.7	3.6	92.4	63.1	30.0

2.4.2 Disturbed Cases

Figure 2.6 shows time series of temperature from 2100 to 0540 MST, and Fig. 2.7 shows time series of temperature flux $\overline{w\theta}$ from 0000 to 0540 MST. (Prior to 0000 MST, the wind was through the tower rendering the sonic measurements useless.) Data for these time series were obtained as 20-min means.

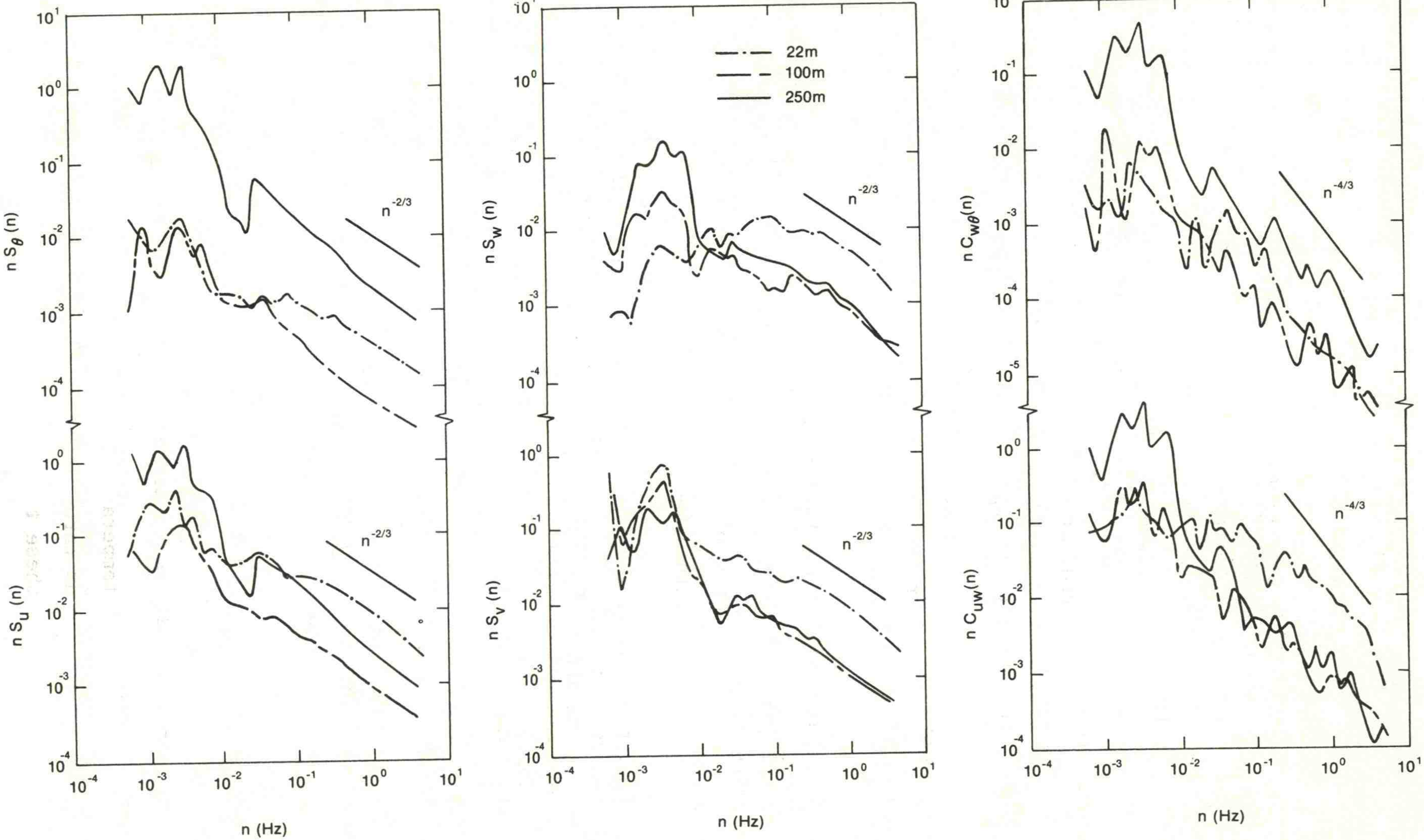


Figure 2.5.--Variance spectra for θ, u, w, and v together with cross-spectra of wθ and uw during 0620-0720 MST, 27 March 1981.

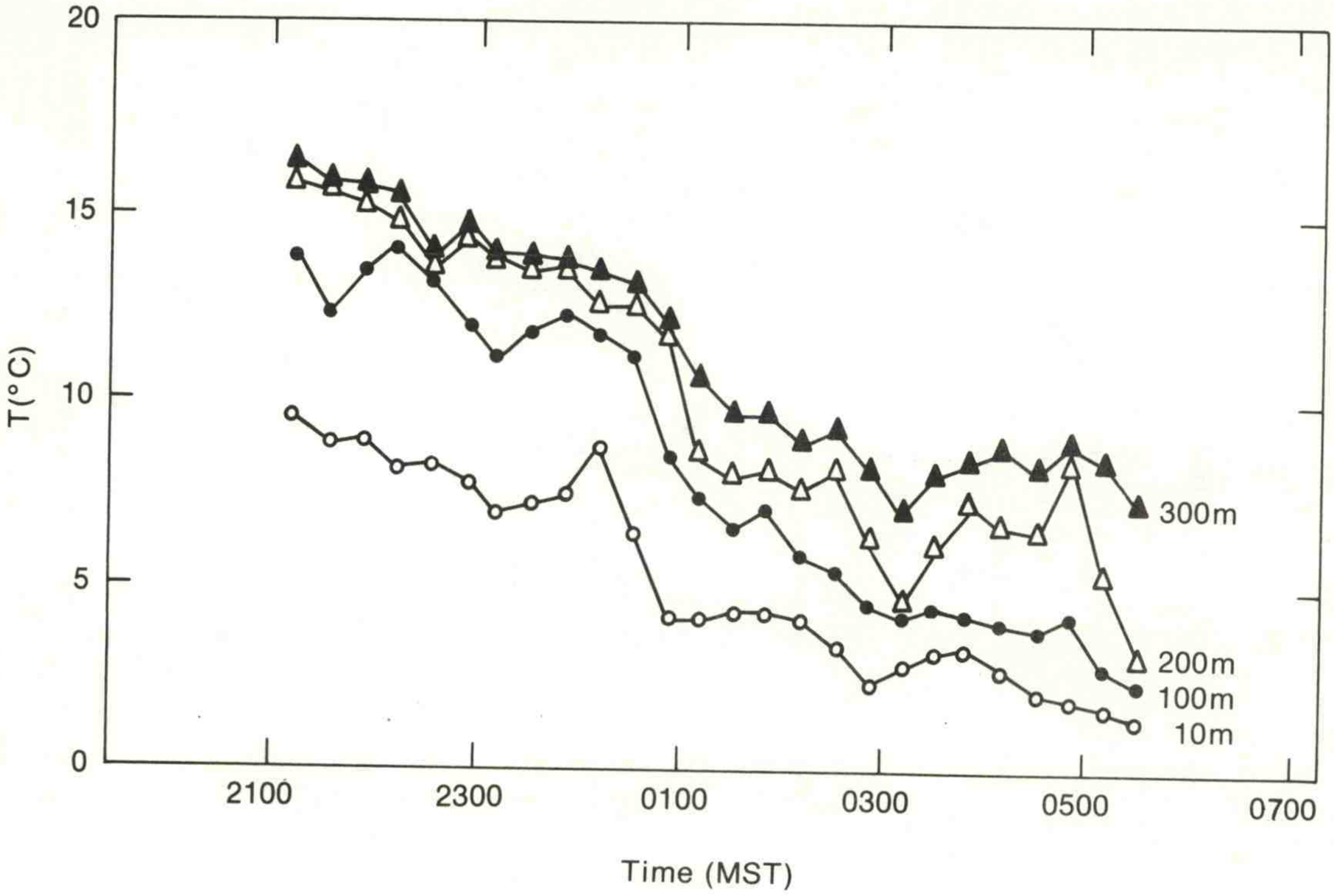


Figure 2.6.--Time series of temperature averaged over 20 min at four tower levels from 2100 MST on 26 March through 0540 MST on 27 March.

The covariance of temperature and vertical velocity was computed in the usual manner after removal of the means. The temperature and temperature flux data used are the standard archived values in the BAO files. As we will show below, use of these standard flux values requires some caution. In principle, simple removal of mean values should be satisfactory if no more than one time series has a trend. In general it is assumed that the time series of w is free of trends. An example will be given later where this is not the case.

Notable in the temperature traces is the interruption of the general cooling trend by a warming at midlevels after 0300 MST. Unusual in the flux time series are the positive fluxes observed several times during the night. Since these are counter-gradient, they are most puzzling. Applying the technique used in the previous section, of integrating the cospectrum of w and θ separately over wave and turbulence intervals, we find that the positive contributions to the temperature flux come from low-frequency motions. Inspection of Fig. 2.7 shows positive fluxes mostly in the midlevels of the tower

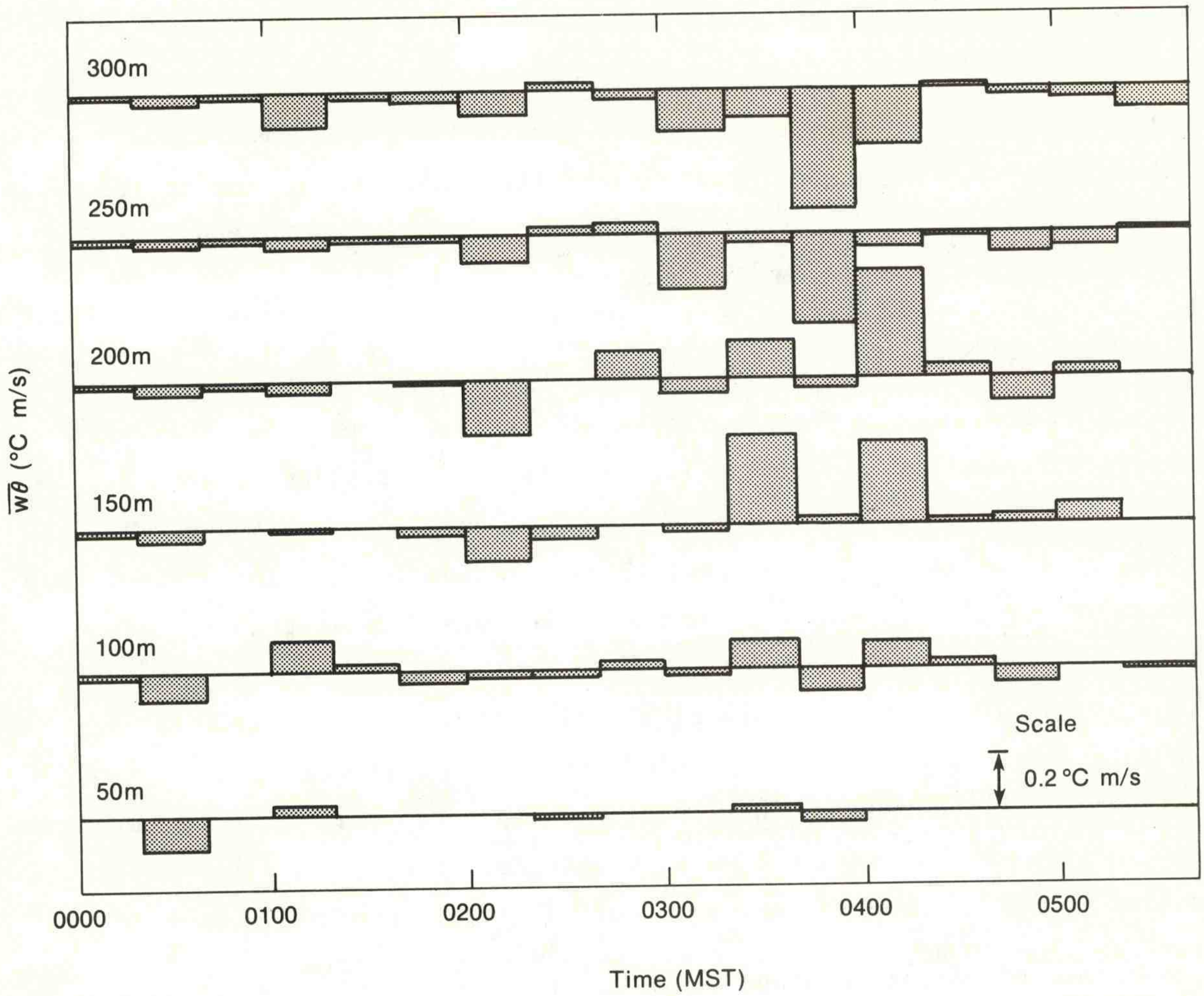


Figure 2.7.--Time series of temperature flux $\overline{w\theta}$ calculated over 20 min from 0000 to 0540 MST, 27 March 1981.

(100-200 m) with negative fluxes at 250 and 300 m. Comparison with the temperature traces in Fig. 2.6 shows that this midlevel flux convergence corresponds to a period of net warming at 200 m. From Fig. 2.7, taking an average flux difference of 0.2°C m/s between 150 m and 250 m respectively, over the period from 0320 to 0440 MST, produces a net heating of 9.6°C in the absence of advective or radiative temperature changes. This temperature change compares with the observed heating of about 4°C at 200 m over the same period. In the next section we examine these unusual counter-gradient fluxes in more detail.

2.5 INTERPRETATION

Our analysis of the temperature flux measured at each level showed periods during which there was a net upward flux that was counter to the mean gradient. The first of these occurred shortly after 0100 MST, the second after 0500, and the third after 0330 MST.

In the analysis of the $w\theta$ cospectrum, upward temperature flux was associated with frequencies characteristic of internal waves. The spectral technique, however, has the limitation that it does not allow an identification of contributions to the positive flux from any isolated events. In addition, it is difficult to separate idiosyncracies in the time series (such as trends or steps) from waves after they have been Fourier-transformed.

Inspection of the time series of the product $w\theta$ often showed singular flux events where an excursion in one direction was followed by one of the opposite sign. Since the net contribution appeared to come from the imbalance between the two, which was not always evident from the actual time series of $w\theta$, a time series of the cumulative sum of $w\theta$ is more useful for identifying the contribution of such individual events. Such time series, plus those of w and θ, are shown for each of three cases in Fig. 2.8. Case 1 shows the effect of a long-period wave combined with a step decrease in temperature associated with the passage of the frontal interface. Case 2 shows a similar case with the added complication of a slow drift in the mean vertical velocity. Case 3 represents a strong disturbance in the inversion.

2.5.1 Effects at the Frontal Interface, 0100-0140 MST

A key feature in Case 1 is the sharp step in the contributions to the flux associated with the time when the inversion interface moves through the 150-m tower level. As indicated by the vertical velocity trace, the passage occurs at the particular phase of the wave so that a negative velocity is associated with a decrease in temperature. Were the interface to remain stationary and only perturbed by a wave, there would be no net flux. However, with advection of the tilted frontal interface and its associated waves, this becomes a singular event.

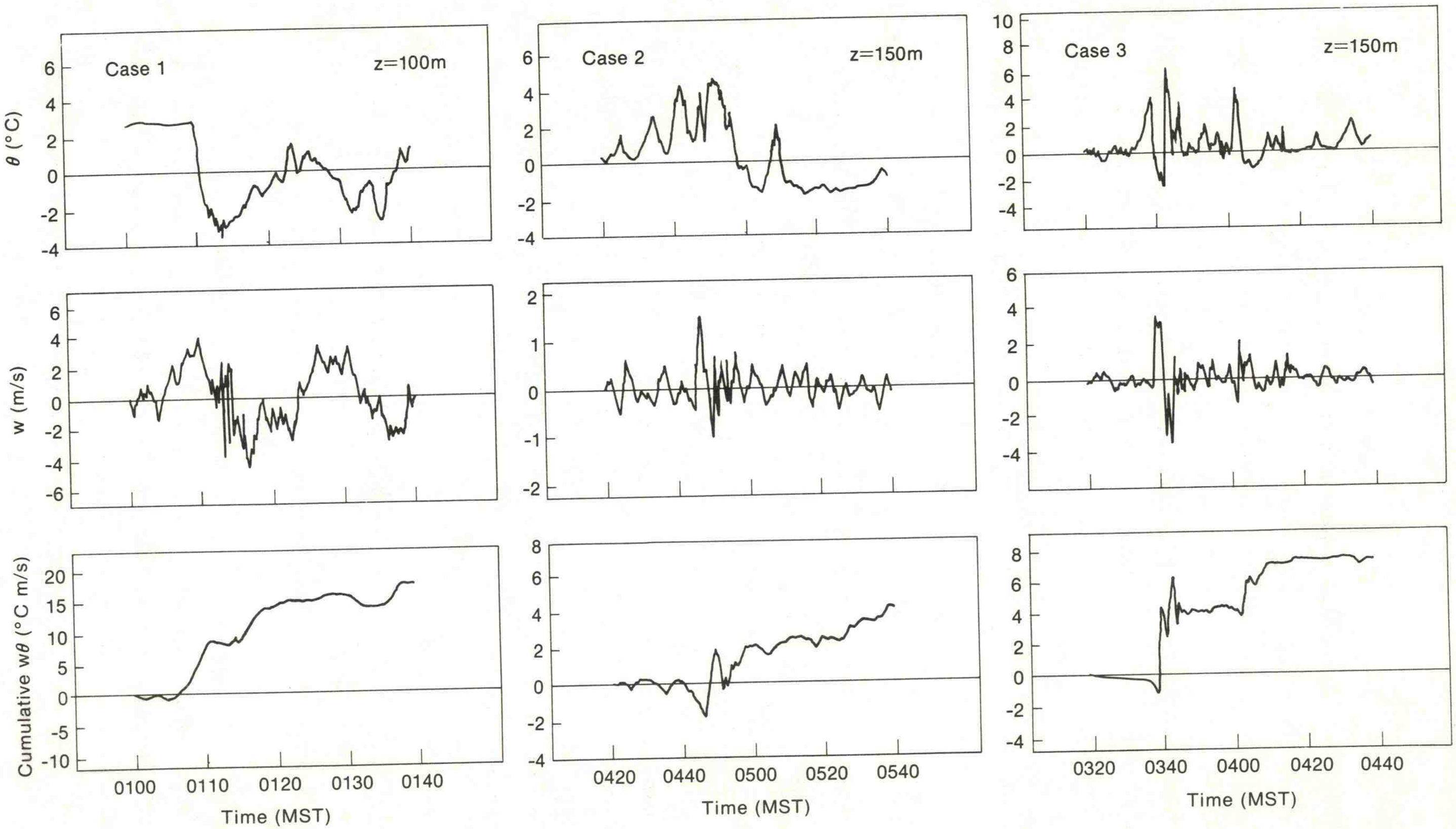


Figure 2.8.--Time series of the cumulative heat flux, w, and θ, for the time periods 0100-0140 MST, 0420-0540 MST, and 0320-0440 MST, which correspond to the record displayed in Fig. 2.1.

2.5.2 Trends/Steps in the Data, 0420-0540 MST

Case 2 shows a similar set of traces for the period after 0500 MST. In this case there is a gradual increase in the net positive flux after an initial step. An inspection of the time series of w, however, shows a downward trend in w, of about 0.25 m/s over 40 min, after the abrupt drop in temperature at 0450 MST. This trend, together with an offset in temperature, contributes the net upward flux. Separate calculations, based on means taken before and after the step, show no positive flux.

2.5.3 Strong Disturbances in the Inversion, 0320-0440 MST

Another anomalous case (Case 3) that we noted earlier occurred between 0320 and 0400 MST. Again, calculating the cumulative contributions to the temperature flux, we see that the contributions occur in discrete steps (Fig. 2.8). However, inspection of the time series shows no steps or trends in either the temperature or vertical velocity data at, for example, 150 m as shown in Fig. 2.8. Returning to Fig. 2.7, it should also be noted that the fluxes at 250 and 300 m due to the same disturbance are downward.

Spectral analysis of w and θ from 150 m reveals several peaks in the range from 0.001 to 0.004 Hz (Fig. 2.9). Use of a linear frequency scale here allows identification of three distinct frequency components common to both w and θ. Of note is that the central peaks match well while the adjacent peaks are shifted in frequency. The cospectrum of w and θ, using standard BAO programs, shows a broad peak in the same region. However, logarithmic smoothing of the spectra by these programs does not allow detailed examination of the cospectrum. Averaging of the cospectra and quadrature spectra over the entire band gives an average phase shift of -62°.

Not shown in Fig. 2.9 is the spectrum of pressure fluctuations at the surface. In this case the pressure spectrum closely followed the w spectrum. From our earlier analysis of microbarograph data, such as that presented in Fig. 2.4, we also found a spectrum of waves propagating opposite in direction to the inversion jet. To correlate surface pressure fluctuations with events

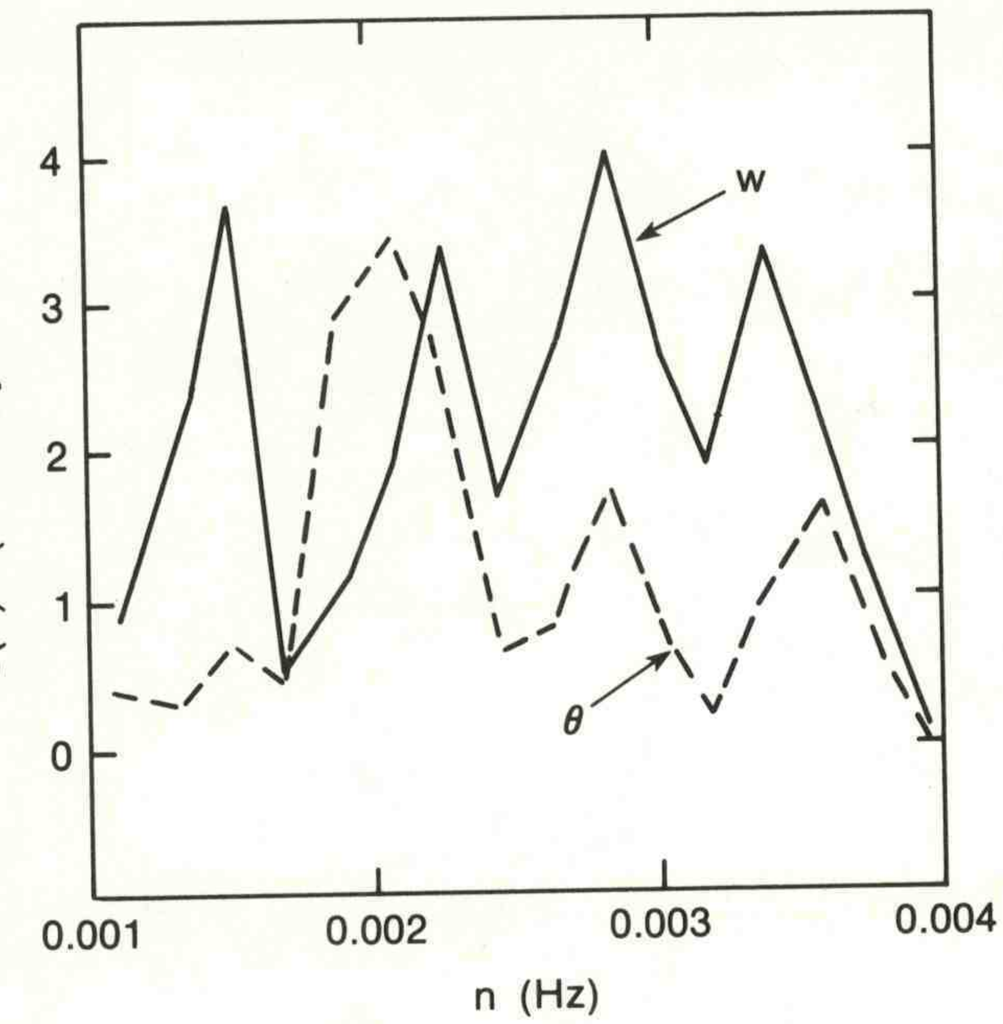


Figure 2.9.--Spectra of w and θ from 150 m in the frequency range 1-4 × 10^{-3} Hz on linear scales, for 0320-0440 MST, 27 March 1981.

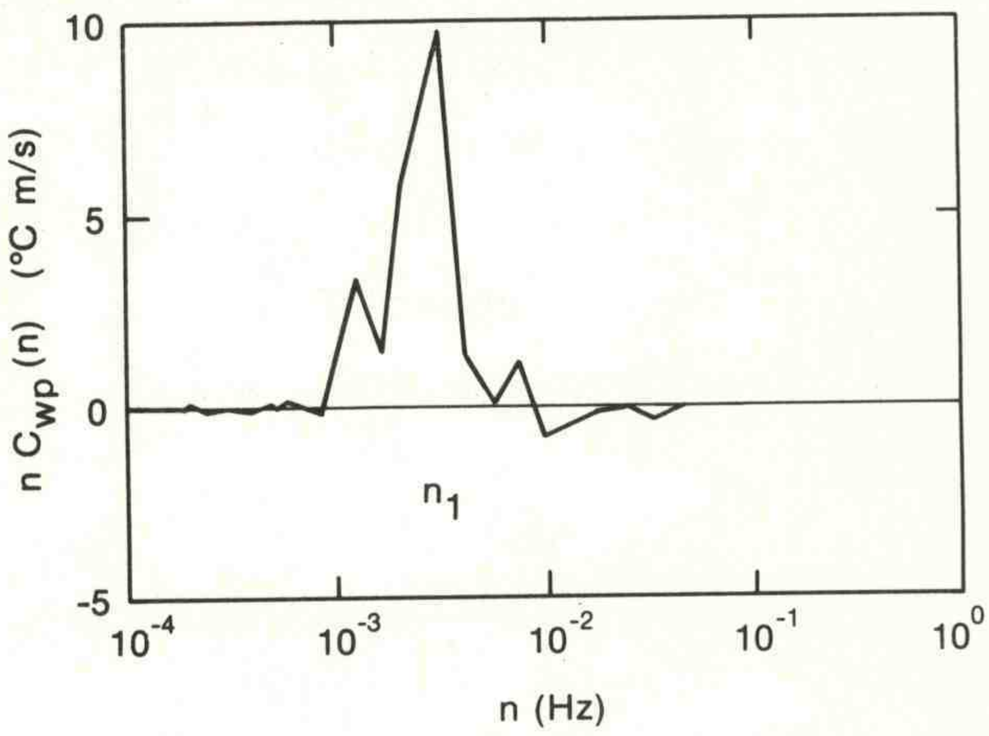


Figure 2.10.--Cospectrum of w and p for the time period in Fig. 2.9.

within the inversion, we computed the cospectrum of w at 150 m with surface pressure at the base of the tower. This is shown in Fig. 2.10 where smoothing of the spectrum has again produced one central peak in the cospectrum. The quadrature spectrum in this case is small compared with the cospectrum. This in-phase relationship may reflect, in part, a phase shift introduced by the slower time constant of the pressure sensor compared with that of the sonic-derived w measurement. The finding that variations in w within the inversion are well correlated with surface pressure fluctuations remains valid. Similar comparisons with temperature are not as clear except in those cases where the temperature sensor happened to be near the top of the elevated inversion (see Fig. 2.3) where temperature fluctuations are more pronounced.

Given the presence of these cospectral peaks, we used our filtering program to produce the time series of w and θ in the frequency range shown in Fig. 2.9. These are shown in Fig. 2.11 together with identifiable phase shifts at each cycle of the wave at heights of 300 and 200 m. The fact that the wave packet centered on the time of the primary disturbance is fairly

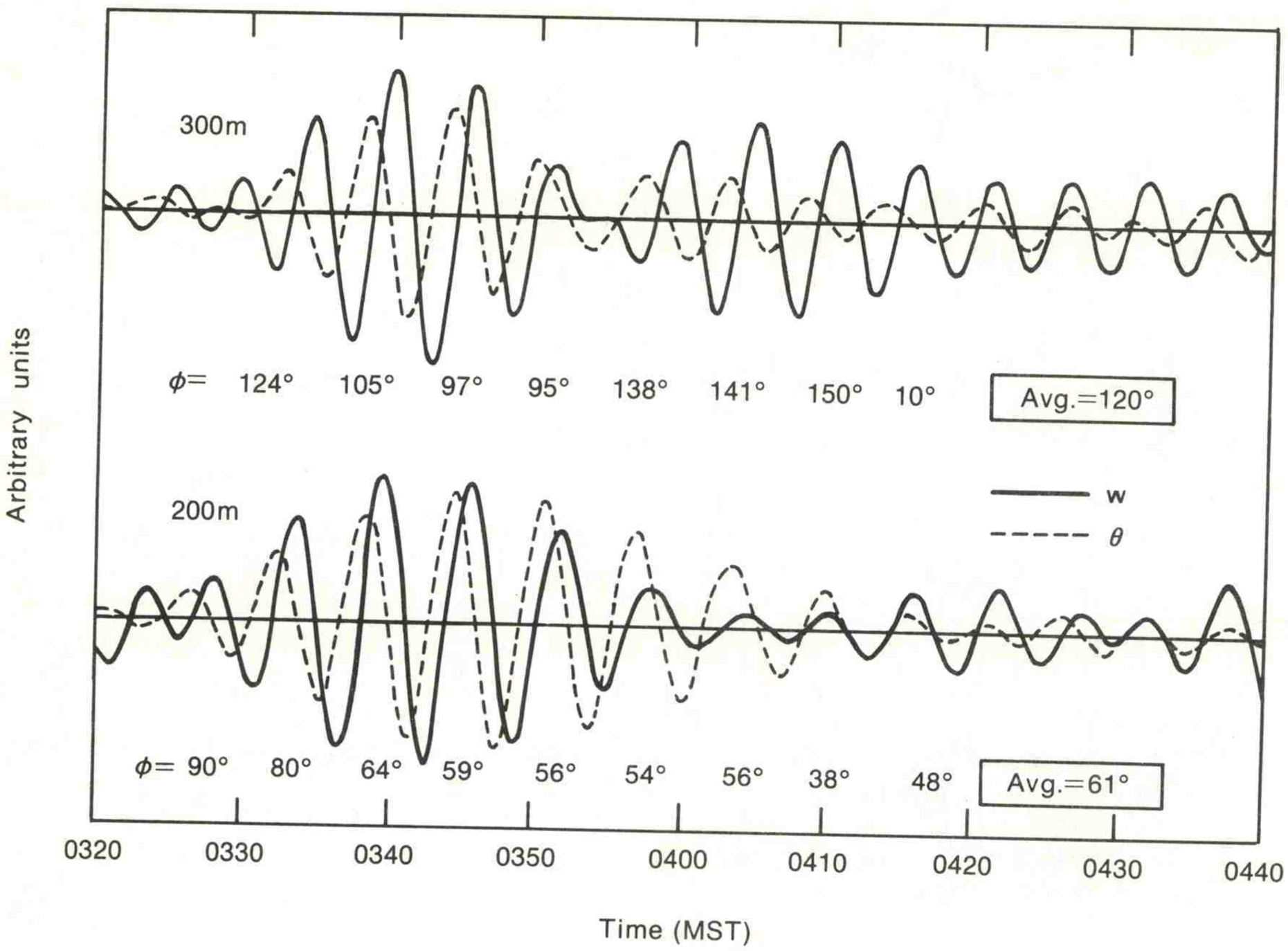


Figure 2.11.--Narrow bandpasses time series of w and θ at two fixed levels for 0320-0440 MST on 27 March 1981 for the frequency range shown in Fig. 2.9. ϕ indicates individual phase shifts.

broad is a consequence of the narrow bandwidth used to filter the original time series. The breadth of the packet, Δt in time, obeys the relation $\Delta f \cdot \Delta t = 1$, where Δf is the bandwidth. For an ordinary internal wave, density variations are 90° out of phase with vertical velocity (e.g., Turner, 1973). As can be seen in comparison with Fig. 2.7, a shift of less than 90° leads to a positive flux, whereas a shift greater than 90° produces a negative flux.

Although these results suggest vertical transfer of heat at wavelike time scales, the actual transfer of heat by a wave seems physically implausible. However, one can imagine a combination of circumstances involving large-amplitude solitary waves acting in conjunction with horizontal temperature advection to produce such isolated fluxes. Profiles at a single location are not, however, sufficient to resolve such questions.

2.6 CONCLUSIONS

The analysis of a nocturnal inversion disturbed by the passage of a shallow cold front shows the dominance of low-frequency motions over turbulence in the calculation of variances and covariances. In addition, the unsteadiness of the flow, with both wave and advective processes present, was shown to create difficulties in standard flux calculations. Such effects are critical in the interpretation of long-term flux data archived from towers such as BAO.

Three cases were presented. The first one showed that anomalous fluxes could occur with the fortuitous superposition of wave motion and the advection of the frontal interface through a fixed tower level. The second revealed a positive flux arising from a combination of a trend in w together with a sharp decrease in temperature. The third, involving a large-amplitude disturbance in the inversion, proved more intriguing. Analysis of this third case motivated the introduction of two additional analysis techniques. The first involved forming a cumulative sum of the product of w and θ. This showed that the apparent wavelike contributions to the upward vertical temperature flux actually occurred in short bursts. Cospectral analysis of w and θ in this case showed equal and opposite phase shifts, away from the 90° expected of internal wave motion, above and below the elevated inversion base. A second technique was introduced to relate events within the inversion to wave motion sensed by the surface microbarograph array. To accomplish this, we formed cospectra of tower variables such as w with the pressure time series at the base of the tower. The cospectrum of w and p showed strong peaks at the same frequencies as those in the spectra of w and θ, suggesting that the large-amplitude disturbances in the inversion layer flow were wave related. Although some of the tower data show that advection may be an important element in the interpretation of such low-frequency effects, sufficient data to resolve the problem do not exist.

2.7 ACKNOWLEDGMENT

We are grateful for the additional map analysis and discussion provided by R. Zamora.

2.8 REFERENCES

Atkinson, B.W., 1981: Meso-scale Atmospheric Circulations. Academic Press, New York, 495 pp.

Axford, D.N., 1971: Spectral analysis of an aircraft observation of gravity waves. Quart. J. Roy. Meteorol. Soc., 97, 313-321.

Caughey, S.J., 1977: Boundary-layer turbulence spectra in stable conditions. Bound.-Layer Meteorol., 11, 3-14.

Caughey, S.J., and C.J. Readings, 1975: An observation of waves and turbulence in the Earth's boundary layer. Bound.-Layer Meteorol., 9, 279-286.

Caughey, S.J., J.C. Wyngaard, and J.C. Kaimal, 1979: Turbulence in the evolving stable boundary layer. J. Atmos. Sci., 36, 1041-1052.

Einaudi, F., and J.J. Finnigan, 1981: The interaction between an internal gravity wave and the planetary boundary layer. Part I: The linear analysis. Quart. J. Roy. Meteorol. Soc., 107, 793-806.

Emmanuel, C.B., B.R. Bean, L.G. McAllister, and J.R. Pollard, 1972: Observations of Helmholtz waves in the lower atmosphere with an acoustic sounder. J. Atmos. Sci., 28, 886-892.

Gossard, E.E., J.H. Richter, and D. Atlas, 1970: Internal waves in atmosphere from high resolution radar measurements. J. Geophys. Res., 75, 903-913.

Kaimal, J.C., 1973: Turbulence spectra, length scales, and structure parameters in the stable surface layer. Bound.-Layer Meteorol., 4, 289-309.

Kaimal, J.C., and J.E. Gaynor, 1983: The Boulder Atmospheric Observatory. J. Clim. Appl. Meteorol. (accepted).

Kaimal, J.C., R.A. Eversole, D.H. Lenshow, B.B. Stankov, P.H. Kahn, and J.A. Businger, 1982: Spectral characteristics of the convective boundary layer over uneven terrain. J. Atmos. Sci., 39, 1098-1114.

Keliher, T.E., 1975: The occurrence of microbarograph-detected gravity waves compared with the existence of dynamically unstable wind shear layers. J. Geophys. Res., 80, 2967-2976.

Merrill, J.T., 1977: Observational and theoretical study of shear instability in the airflow near the ground. J. Atmos. Sci., 34, 911-921.

Neff, W.D., 1980: An observational and numerical study of the atmospheric boundary layer overlying the east Antarctic ice sheet. Ph.D. Thesis, University of Colorado, Boulder, Colo., 272 pp.

Steward, R.W., 1969: Turbulence and waves in a stratified atmosphere. Radio Sci., 4, 1269-1278.

Turner, J.S., 1973: Buoyancy Effects in Fluids. Cambridge Univ. Press, Cambridge, England, 367 pp.

Wyngaard, J.C., and O.R. Coté, 1972: Cospectra similarity in the atmospheric surface layer. Quart. J. Roy. Meteorol. Soc., 98, 590-603.

Zhou Ming-yu, Lu Nai-ping, and Qu Shaohou, 1980: Applications of sodar data in weather analysis and local weather forecasting. Kexue Tongbao, 25, 328-331.

3. A STUDY OF MULTIPLE STABLE LAYERS IN THE NOCTURNAL LOWER ATMOSPHERE

Li Xing-sheng
Institute of Atmospheric Physics
Academia Sinica
Beijing, China

J.E. Gaynor and J.C. Kaimal
NOAA/ERL/Wave Propagation Laboratory
Boulder, Colorado 80303

ABSTRACT. The structure of nocturnal inversions in the first 300 m of the atmosphere is analyzed using the observational data from the Boulder Atmospheric Observatory from March through June 1981. The temperature profiles show more than one inversion layer 41% of the time during the observational period. The vertical distributions of wind speed and moisture also show evidence of stratification during these multiple-layer events. The relation between the radiative cooling rate in time and height, including moisture, and the vertical structure of the multiple layers is calculated. The vertical distribution of eddy kinetic energy and the turbulent vertical fluxes of heat and momentum are also calculated. Turbulent structure in the elevated inversion layers is more complicated than that in the single-layer, stable nocturnal boundary layer. The total heat budget for a multiple-layer case is calculated, and turbulent cooling is found to be negligible relative to radiative cooling and to horizontal advection and/or horizontal divergence of heat flux.

3.1 INTRODUCTION

In recent years, the study of the nocturnal stable boundary layer has received much attention. Many nocturnal boundary layer models have been developed (Delage, 1974; Businger and Arya, 1974; Wyngaard, 1975; Blackadar, 1976; Brost and Wyngaard, 1978; André et al., 1978; Zeman, 1979; Li et al., 1982a), and many studies have been made of the parameterization of the nocturnal boundary layer as well as of the basic vertical structure of the stably stratified atmospheric boundary layer (Rao and Snodgrass, 1979; Sundararajan, 1979; Mahrt et al., 1979). However, observational studies of the nocturnal lower atmosphere, of which the boundary layer is only a part, are rather incomplete. Its description has been restricted because of the

lack of detailed turbulence and mean field measurements with height. The Boulder Atmospheric Observatory (BAO) tower provides such information.

An experiment directed toward the study of the nocturnal lower atmosphere was conducted at BAO between March and June 1981. Measurements taken during this intense observational period included, in addition to standard data from the 300-m BAO tower, profiles of wind, temperature, and humidity using instruments attached to a movable carriage on the tower, and facsimile records of echo intensities from an acoustic sounder located near the tower.

The sensors on the tower and data acquisition procedures have been discussed by Kaimal and Gaynor (1983). The carriage sensors were mounted on two horizontal booms separated 10.3 m vertically. The lower boom supported a sonic anemometer measuring the mean and fluctuating components of the wind along three orthogonal axes, a quartz thermometer measuring mean temperature, a platinum-wire thermometer measuring temperature fluctuations, a Lyman-alpha hygrometer measuring fluctuations in specific humidity, and a propeller vane anemometer measuring mean wind speed and direction. For gradient measurements across the 10.3-m vertical spacing, the upper boom supported another quartz thermometer, Lyman-alpha hygrometer, and propeller-vane anemometer. The movable carriage ascends the full tower length in about 8.8 min and descends in about 8.5 min.

3.2 FORMATION OF MULTIPLE LAYERS

Measurements made with the acoustic sounder and with sensors mounted on the tower indicate that the structure of the nocturnal lower atmosphere is very complex. The inversion structure is often correlated with isolated echo layers in the facsimile records. The statistical results in Fig. 3.1 show that of the 87 nights examined (25 March-22 June 1981), 35 had at least one occurrence of multiple layers. The probability of occurrence of multiple layers on any one night, therefore seems reasonably high. The starting time of such events is variable, but Fig. 3.1 shows a high concentration (86% of the cases) between 2000 and 0200 mountain standard time (MST). The duration of a multiple-layer event varies from 3 to 12 h.

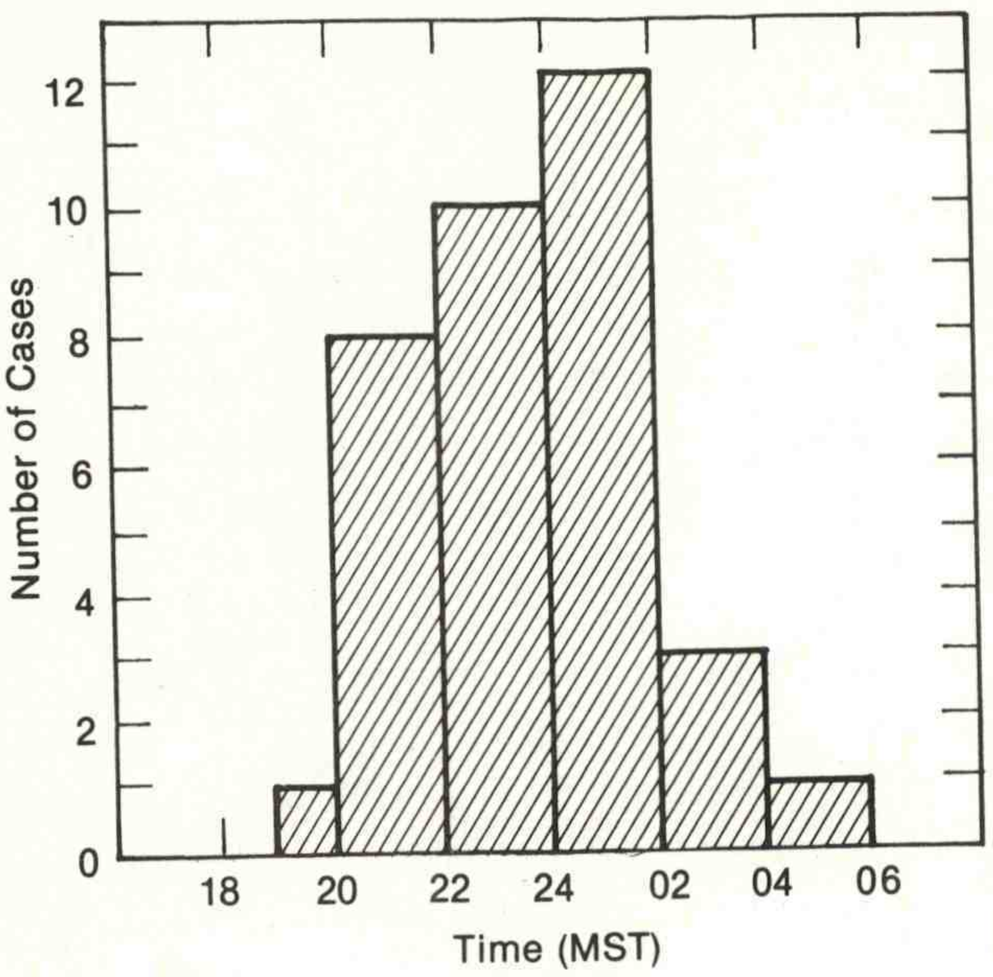


Figure 3.1.--Frequency distribution of times when multiple inversion layers initially occurred between 25 March and 22 June 1981.

The formation of multiple layers is almost always associated with certain atmospheric conditions and/or local topographical features. Following are some of the conditions that favor such formation:

(1) Subsidence and advection associated with the passage of a cold front in uniform and complex terrain (Neff, 1980).

(2) Cold-air outflows from local thunderstorms (Goff, 1976).

(3) Drainage winds in the vicinity of mountain ranges, as observed often at BAO (Hootman and Blumen, 1981).

Li et al. (1982b) have discussed a multiple-layer event caused by advection. This study will focus on a more typical event at BAO, one caused by drainage flow from the Rocky Mountains 60 km to the west.

3.3 A CASE STUDY

The event under consideration occurred between 0100 and 0530 MST, 24 April 1981. One carriage profile (either ascending or descending) was

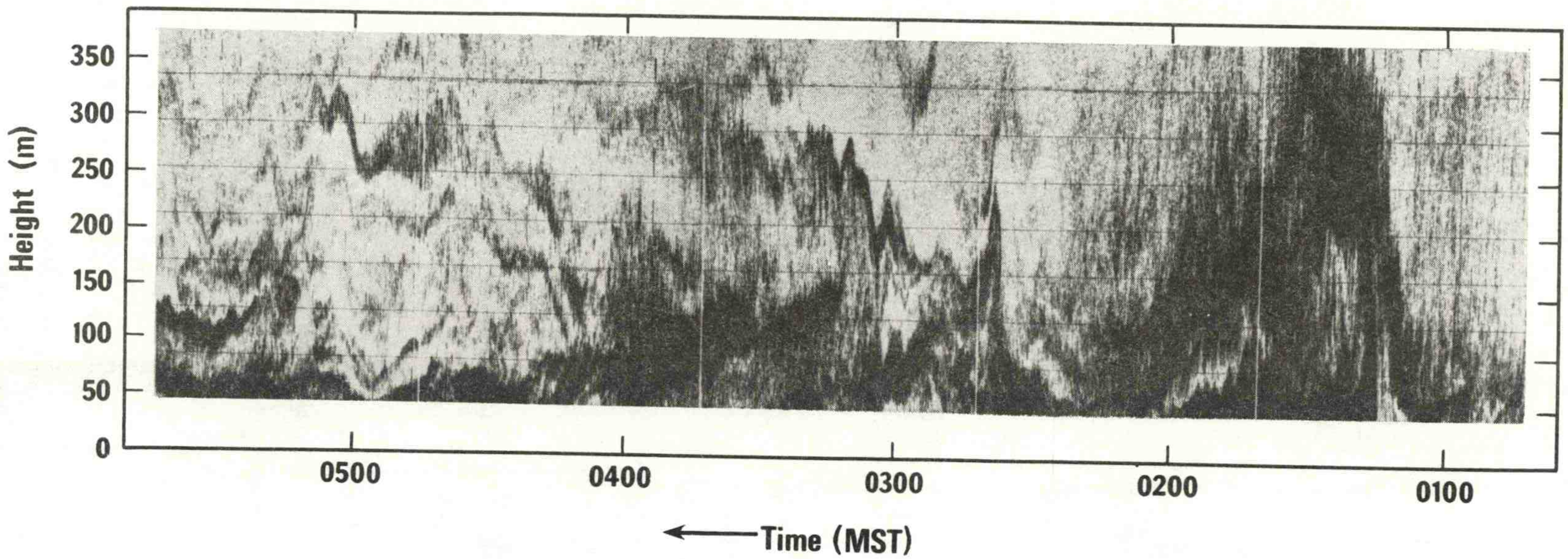


Figure 3.2.--The acoustic record of multiple inversion layers on 24 April 1981.

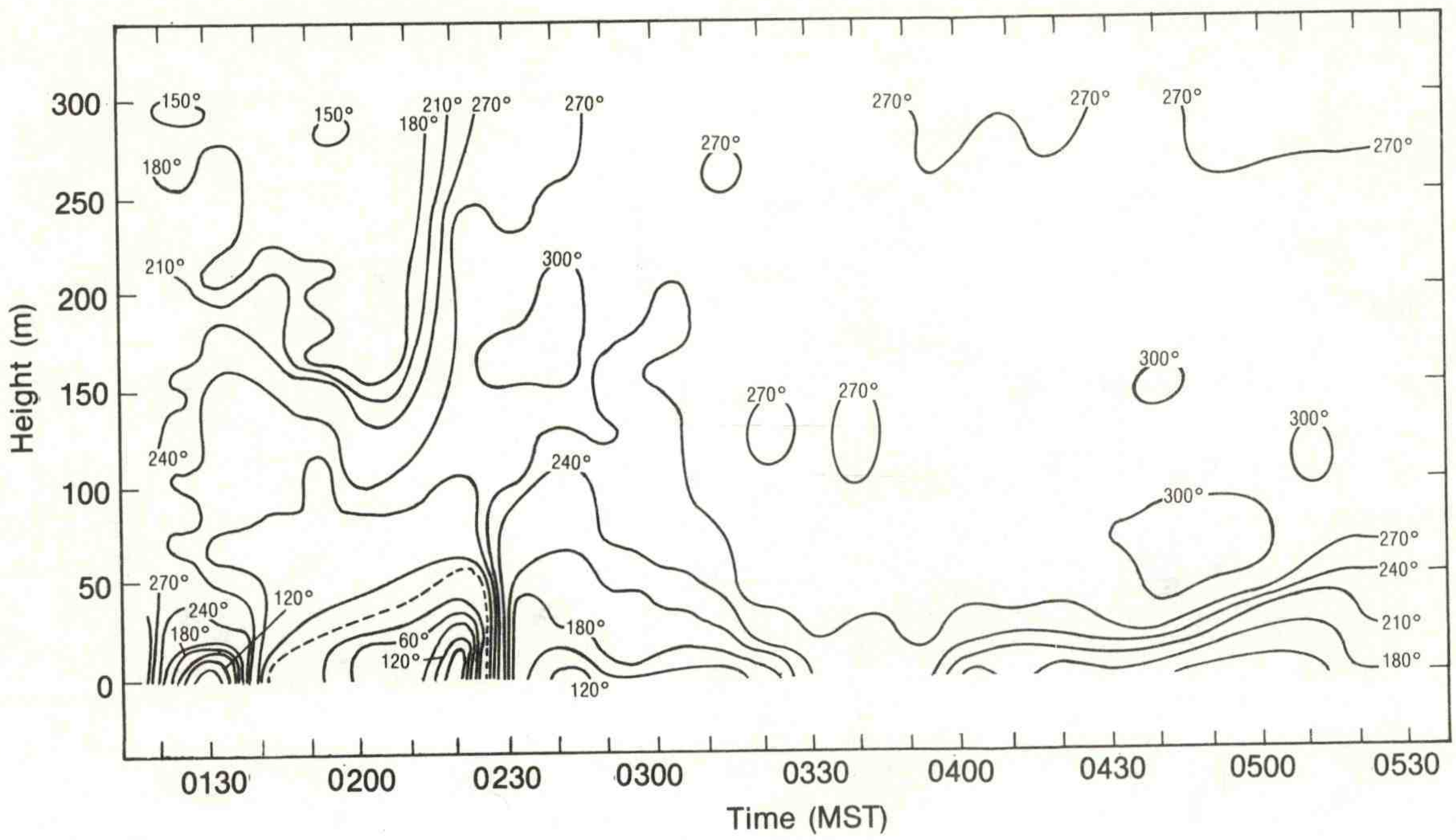


Figure 3.3.--The time-height cross section of the wind direction on 24 April 1981. Isolines are at 30° intervals.

recorded every 10 min during that period. The observed time series on all the data channels were block-averaged over consecutive 10-s blocks. This averaging corresponds to a 6-m spatial averaging in the vertical and is clearly more useful for detection of elevated layers than the 50-m spacing between the fixed levels on the tower. These smoothed vertical profiles from the carriage sensors were used to construct time-height cross sections of the measured variables.

The acoustic record (Fig. 3.2) indicates that multiple-layer structures started to form between 0100 and 0200 MST and between 0230 and 0330 MST. The time-height cross section of wind direction between 0120 and 0530 MST on 24 April 1981 is shown in Fig. 3.3. Before 0230 MST, the wind direction was essentially southerly above 150 m, northwesterly between 150 and 50 m, and quite variable below 50 m. After 0230 MST, a significant change in wind direction occurred within the tower height. The wind direction became generally northwesterly above 50 m and southeasterly below 50 m.

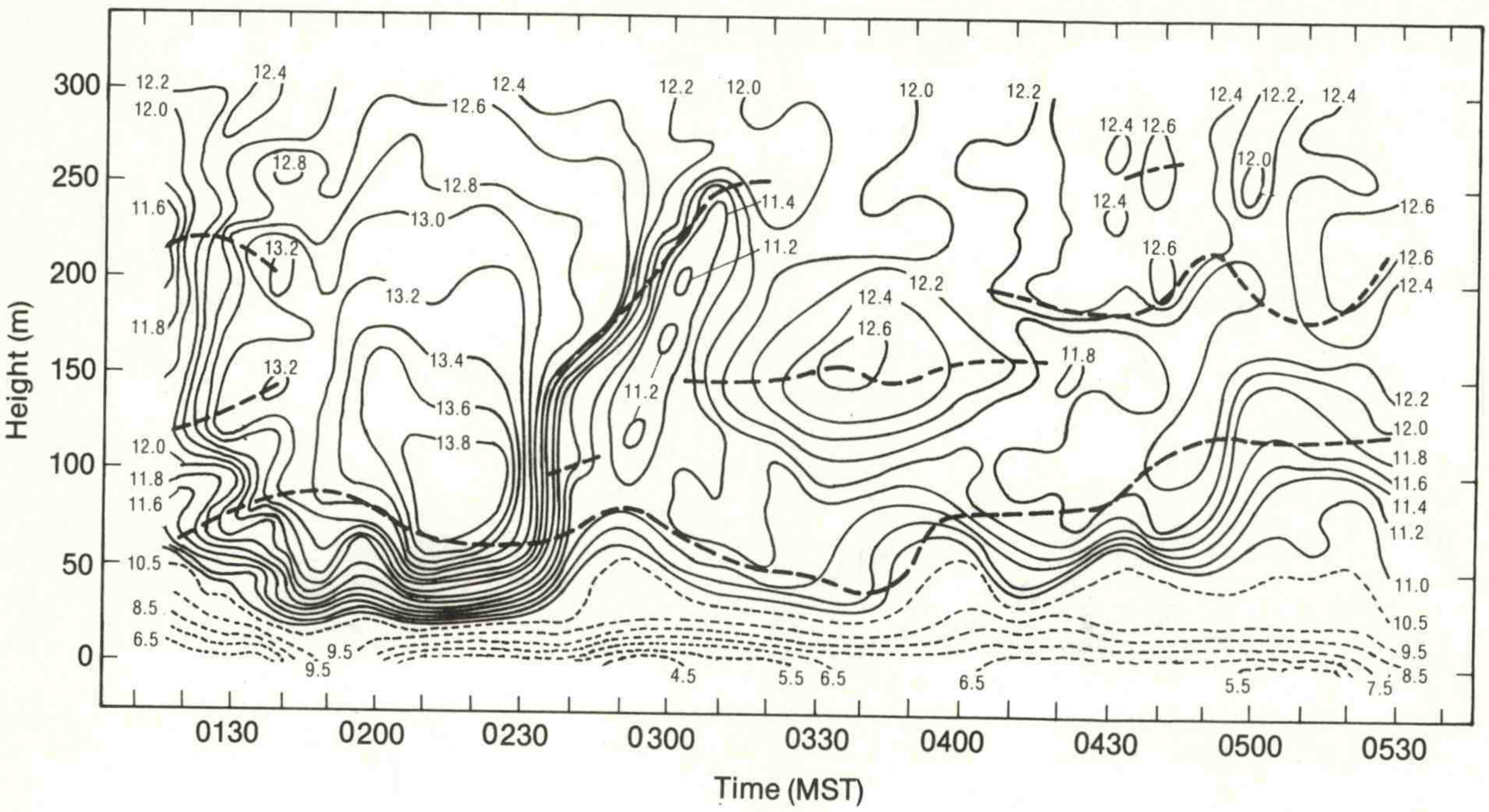


Figure 3.4.--The time-height cross section of the temperature on 24 April 1981. Solid lines are isotherms at 0.2°C intervals; thin dashed lines are at 0.5°C intervals; thick dashed lines indicate tops of the inversions.

The time-height cross section of temperature for the same case is shown in Fig. 3.4. The thick dashed lines indicate tops of the inversions ($\frac{\partial T}{\partial z} > 0$ below the thick dashed lines). The temperature field shows multiple inversion layers between 0120 and 0200 MST, in agreement with the multiple echo layers on the acoustic record (Fig. 3.2). After 0230 MST, there was an inflow of cold air within the middle and lower tower levels. The inversion then divided into two parts, the lower part continuing to exist as a radiation inversion at 50 m, the upper part lifting to 250 m by 0300 MST. The temperature within the upper inversion increased about 1°C with height in a 20- to 30-m thickness. These layers correspond to strong echo layers in the acoustic record of Fig. 3.2. The thermal stratification between the two inversions was nearly isothermal. After 0300 MST an elevated inversion seems to hover around 150 and 200 m as seen in Fig. 3.4. Although Fig. 3.4 shows only two inversion layers, the acoustic sounder record in Fig. 3.2 displays at least four echo layers above 50 m. The multiple echo layers may represent the top and bottom of each inversion layer, or they may represent a smaller scale structure in the temperature profile not easily resolvable in Fig. 3.4.

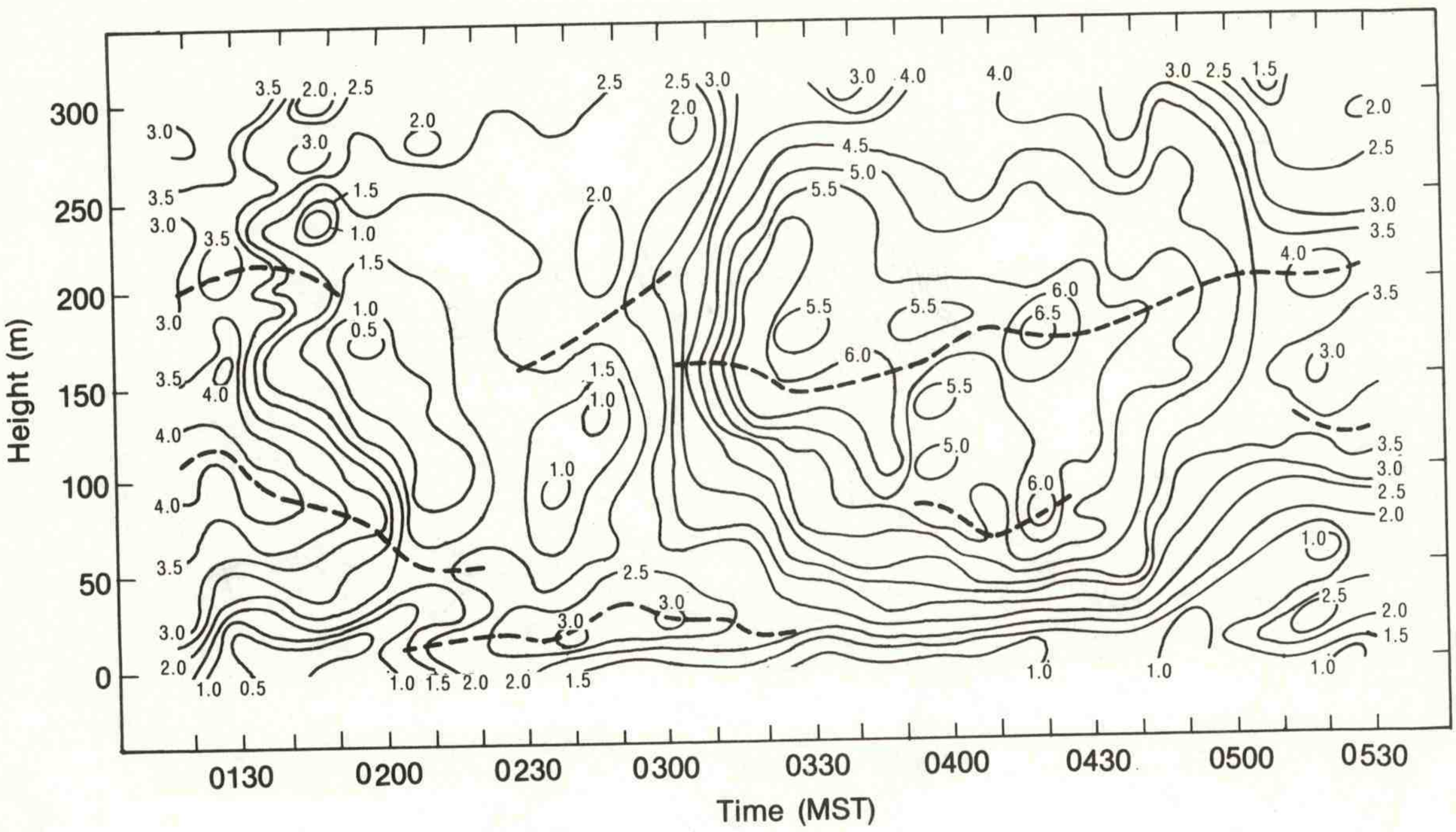


Figure 3.5.--The time-height cross section of the wind speed on 24 April 1981. Solid lines are isotacks at 0.5-m/s intervals; thick dashed lines indicate maximum values of wind speed, i.e., the axes of the low-level jets.

The time-height cross section of wind speed for this case is shown in Fig. 3.5. The wind field shows multiple wind speed maxima from 0120 to 0200 and 0230 to 0330 MST. Their height levels nearly coincide with the stratifications in temperature (Fig. 3.4). After 0330 MST, the low-level jet centered at mid-tower level expanded to a broad maximum as values of wind speed near the surface diminished gradually. After 0500 MST, there were two wind speed maximas at 100 and 200 m, at nearly the same levels as the inversions. These observations are in agreement with the statistical results of Li et al. (1982b), which indicate a strong relationship between multiple wind speed maxima and the existence of multiple inversion layers. The heights of the wind speed maxima roughly coincide with the tops of the inversions.

Figure 3.6 shows the time-height cross section of specific humidity for the same time as the temperature field in Fig. 3.5. It is worth noting that the distribution of the isolines of specific humidity is similar to the distribution of isotherms (Fig. 3.4). After 0230 MST, the moisture field also developed multiple layers. However, the height level of the maximum

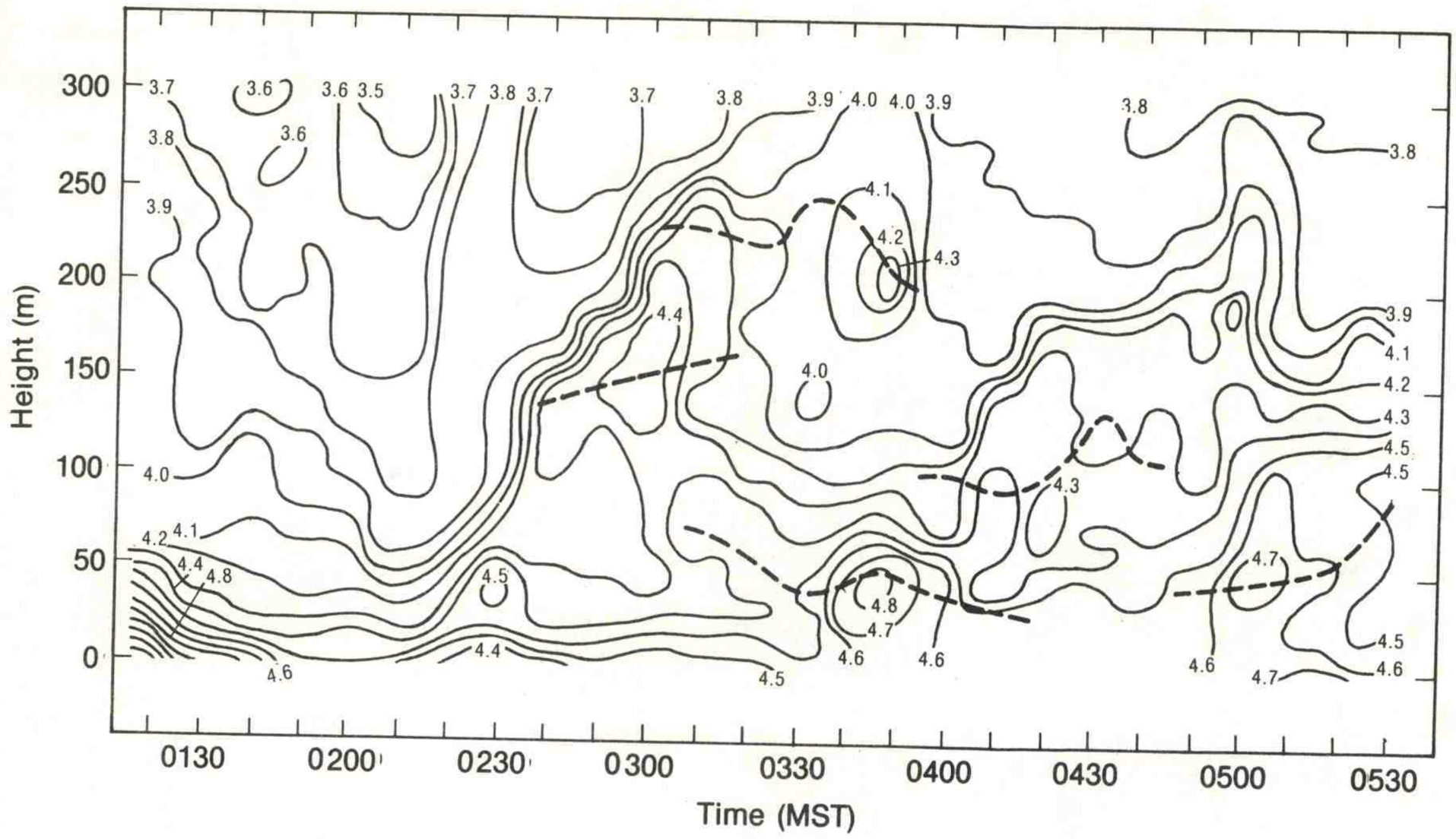


Figure 3.6.--The time-height cross section of humidity on 24 April 1981. Solid lines are isolines of specific humidity at 0.1-g/kg intervals; thick dashed lines indicate maximum values of specific humidity.

value of moisture is below the top of the inversion. The locations of the strong moisture gradients, on the other hand, very nearly correspond to those of the temperature gradients. Radiative-transfer relations show that the greater the moisture content in the inversion layer near the surface, the stronger the radiative cooling at the top of the inversion. Cooling rates in the presence of moisture will be discussed in Sec. 3.5.

3.4 EDDY KINETIC ENERGY AND THE DISTRIBUTION OF TURBULENT FLUXES OF HEAT AND MOMENTUM

The vertical distributions of Richardson number (Ri), horizontal eddy kinetic energy ($\bar{e}_h$), variances ($\overline{w^2}$ and $\overline{\theta^2}$), and fluxes ($\overline{wu}$, $\overline{wv}$, and $\overline{w\theta}$) for the 10-min period from 0250 to 0300 MST are calculated using the observational data at eight fixed levels on the BAO tower. [Overbars indicate time average (10 min); u, v, and w are the longitudinal, lateral, and vertical fluctuations of the wind; and θ is the temperature fluctuation.]

The turbulent fluxes and energy were calculated by integrating spectral and cospectral estimates in the frequency band 0.02-5 Hz. The results are presented in Fig. 3.7 and in Table 3.1. Ri and e_h were calculated using the following relations:

$$e_h = 1/2(\overline{u^2} + \overline{v^2}) \ ,$$

and

$$Ri = \frac{g}{\bar{\theta}_v} \frac{\Delta\bar{\theta}_v}{\Delta z} \Big/ \left[\left(\frac{\Delta U}{\Delta z}\right)^2 + \left(\frac{\Delta V}{\Delta z}\right)^2\right] \ ,$$

where g is the acceleration of gravity, $\bar{\theta}_v$ is the mean virtual temperature, U and V are the mean horizontal wind components along the E-W and N-S axes, and Δ denotes an increment over a finite height interval Δz.

The Richardson number achieves its maximum value at approximately the jet level and has another maximum near the center of the inversion (Fig. 3.7). Therefore, the Richardson number also has a two-layer structure. Its structure is in agreement with the acoustic record of Fig. 3.2. The observations of Mahrt et al. (1979), based on aircraft soundings at Buckley Field, Colo., in September 1975, also show that Richardson numbers reach a maximum and turbulence levels a minimum near the core of a jet. The profiles of e_h and Ri in Fig. 3.7 show the same behavior. Between 50 and 150 m the values of Ri

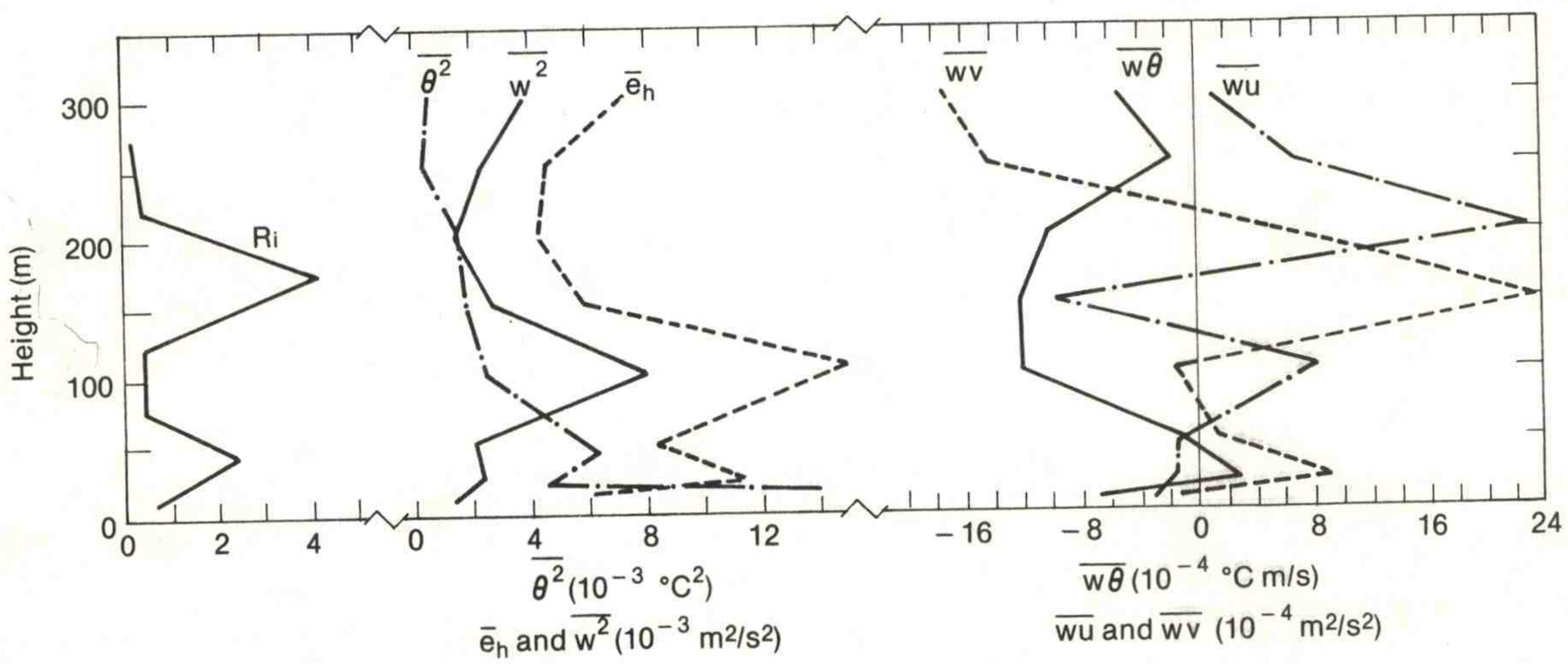


Figure 3.7.--The distributions of Ri, $\overline{\theta^2}$, $\overline{w^2}$, $\bar{e}_h$, $\overline{wv}$, $\overline{w\theta}$, and $\overline{wu}$ with height at 0250 MST on 24 April 1981.

Table 3.1.--Profiles of the turbulent fluxes and energy in the frequency band 0.02-5 Hz

z (m)	$\bar{e}_h$ (10^{-3} m^2/s^2)	$\overline{\theta^2}$ (10^{-3} $°C^2$)	$\overline{w^2}$ (10^{-3} m^2/s^2)	$\overline{wu}$ (10^{-4} m^2/s^2)	$\overline{wv}$ (10^{-4} m^2/s^2)	$\overline{w\theta}$ (10^{-4} °C m/s)
10	6.2	23.0	1.3	-2.7	-1.2	-6.8
22	11.7	4.6	2.2	-1.6	9.5	3.2
50	8.2	6.4	2.1	-1.3	1.6	-0.6
100	15.1	2.5	8.2	8.5	-1.4	-12.0
150	5.9	1.8	2.8	-9.6	24.0	-12.0
200	4.4	1.6	1.5	23.0	6.0	-10.0
250	4.6	0.4	2.4	7.0	-14.2	-1.6
300	7.4	0.6	3.9	1.0	-17.0	-5.3

are close to its subcritical value (Ri = 0.25); between 250 and 300 m, Ri < 0.25. These regions have large $\bar{e}_h$ values. That the temperature field is uniform between the two inversion layers, combined with the low Ri and high $\bar{e}_h$ values between the layers, indicates that this region is well mixed in the vertical. The distribution of $\overline{w^2}$ is similar to that of $\bar{e}_h$. André et al. (1978) gave the following interpretation for the vertical structure of nocturnal turbulence: the horizontal components $\overline{u^2}$ and $\overline{v^2}$ are generated by wind shear, $\partial\bar{u}/\partial z$ and $\partial\bar{v}/\partial z$; their transformation into the vertical component $\overline{w^2}$ by pressure fluctuations would tend to give rise to a strong negative heat flux.

The results in Fig. 3.7 indicate that $\overline{wu}$ is maximum and positive near the jet core. Therefore, the vertical flux of longitudinal momentum is upward. This profile is consistent with the upward movement of the jet core between 0250 and 0300 MST indicated in the wind speed cross section in Fig. 3.5. However, $\overline{wv}$ is negative above the jet core and positive below, so that the vertical transport of the lateral momentum is into the jet. Figure 3.7 shows that there is a general tendency for the temperature variance $\overline{\theta^2}$ to decrease slightly with height above about 50 m.

3.5 TEMPERATURE BUDGET PROFILE

To help understand the maintenance or breakup of multiple layers in the stable nocturnal atmosphere, it is important to study the different factors contributing to variations in the temperature profile. The factors include radiative flux divergence, turbulence heat flux divergence, advection, and subsidence.

The profile of nocturnal radiative cooling with height is complex when temperature and humidity vary with height. To evaluate this, the Brooks (1950) tabular method is used to calculate nocturnal radiative cooling rates with the BAO profile data. The derived formula is the following:

$$\frac{\partial T_A}{\partial t} = \frac{q\kappa}{C_p}\left[\int_o^{\omega_1} \frac{\partial(\sigma T_A{}^4)}{\partial\omega} \frac{\partial\varepsilon\downarrow}{\partial\omega}\, d\omega + \sigma T_A{}^4 \frac{\partial\varepsilon_E}{\partial\omega}\right.$$

$$\left. - \int_o^{\infty} \frac{\partial(\sigma T_A{}^4)}{\partial\omega} \frac{\partial\varepsilon\uparrow}{\partial\omega}\, d\omega\right], \qquad (3.1)$$

where q is the specific humidity; κ the pressure correction factor; C_p the specific heat of air at constant pressure; ω the optical thickness of the radiating substance; σ the Stefan's constant; T_A the absolute temperature; ε the emissivity; ω_1 the upper boundary of the radiating substance; and the arrows indicate the direction from which radiation reaches the reference level. Subscript E denotes the value at the top of the radiating layer.

If the integrals are simplified by considering $\partial(\sigma T_A{}^4)/\partial\omega$ constant within each integration interval and written approximately as $\Delta(\sigma T_A{}^4)/\Delta\omega$, (3.1) can be written as

$$\frac{\partial T}{\partial t} = \frac{q\kappa}{C_p}\left[\sum_{n=1}^{N} \Delta(\sigma T_A{}^4)_n \left(\overline{\frac{\partial\varepsilon}{\partial\omega}}\right)_n + \frac{\partial S_E}{\partial\omega} - \sum_{m=1}^{\infty} \Delta(\sigma T_A{}^4)_m \left(\overline{\frac{\partial\varepsilon}{\partial\omega}}\right)_m\right], \qquad (3.2)$$

where $\partial S_E/\partial\omega = \sigma T_A{}^4(\partial\varepsilon_E/\partial\omega)$ is computed at 700 mb. The summation over n is for layers above the reference level into which the atmosphere has been divided, and the summation over m is for layers below the reference level. $\Delta(\sigma T_A{}^4)$ is zero at the ground surface.

The emissivity curve $\overline{\partial\varepsilon/\partial\omega}$ was taken from Brooks (1950, Table C), which ignores CO_2 absorption (assumed negligible). Brooks calculates the water vapor absorption from laboratory measurements using isothermal radiation and small path lengths. The vertical integration of (3.2) begins at the 2-m level.

The variation of radiative cooling rate with height has been calculated using (3.2). Figure 3.8 shows the results computed from the carriage profile that began at 0250 MST. Because the surface inversion below 22 m is very strong and moist, the radiative cooling rate is very strong (-0.47°C/10 min) at the top of this layer. This distribution of temperature and humidity also

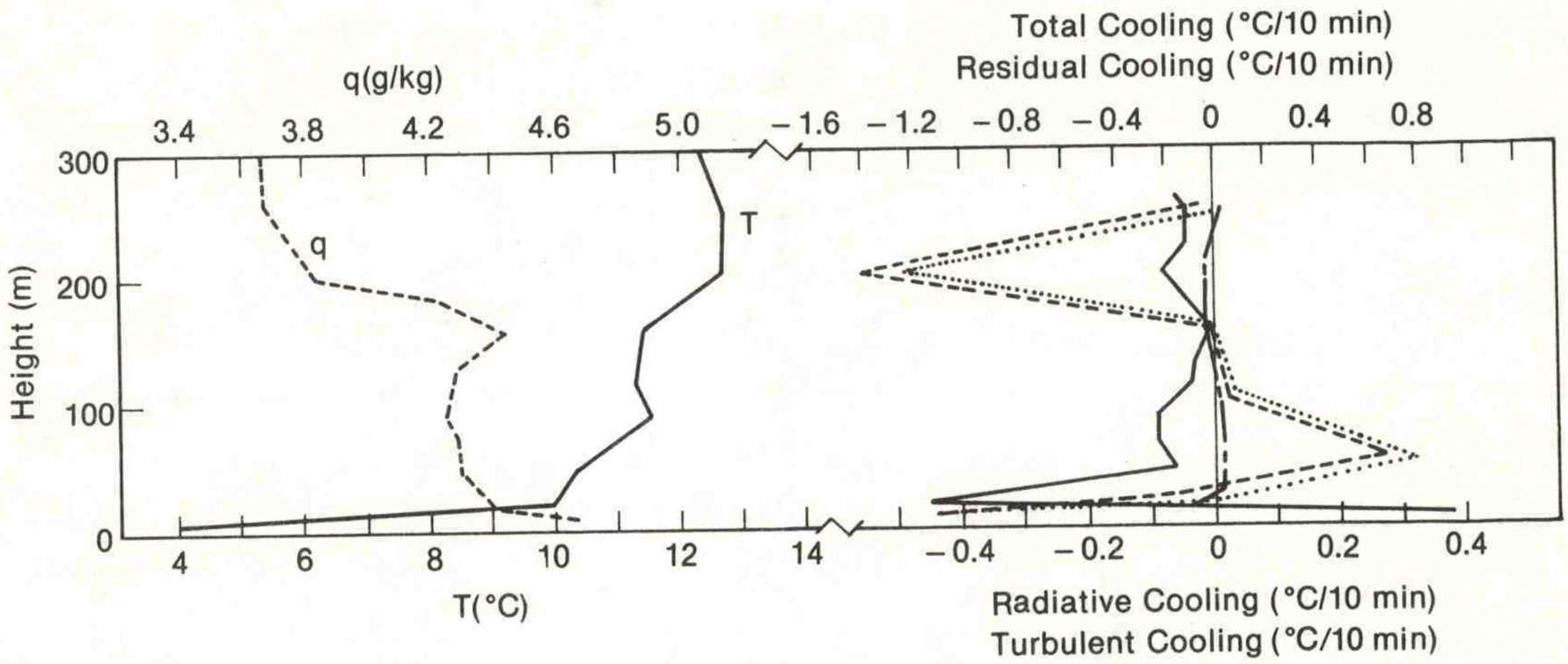


Figure 3.8.--Profiles of specific humidity (q), temperature (T), total cooling (---), radiative cooling (——), residual cooling (••••), and turbulent cooling (— - —) for the case on 24 April 1981.

accounts for the strong warming in the layer nearest the surface. In addition, the cooling rate is larger at the levels of the temperature maxima. The cooling rate maximum at the top of the surface inversion will cause the inversion strength below to weaken with time, and the temperature gradient above to strengthen. The net effect of such cooling may be to maintain any elevated inversion present (Staley, 1965).

We can study the relative importance of radiative cooling in the temperature budget profile for this case using the relation

$$\frac{\Delta T_A}{\Delta t} = (\text{Radiative cooling}) - \frac{\Delta \overline{w\theta}}{\Delta z} + (\text{Residual cooling}) \quad . \tag{3.3}$$

$\Delta T_A/\Delta t$ is the total temperature change during the 10-min interval; the radiative cooling is calculated from (3.2); the turbulent cooling rates $-\Delta\overline{w\theta}/\Delta z$ are calculated from the results in Table 3.1; and the residual term contains the horizontal advection of temperature and subsidence. The divergence of the horizontal heat flux is presumed to be small.

Table 3.2 presents the results for height intervals between successive tower levels, and Fig. 3.8 the plots of profiles of all the terms in the heat

Table 3.2.--Temperature budget (°C/10 min) for the case of 24 April 1981

z (m)	Ri	$\frac{\Delta T}{\Delta t}$ (interpolated)	Turbulent cooling $-\Delta\overline{w\theta}/\Delta z$ ($\times 10^{-1}$)	Radiative cooling	Residual cooling
16	0.98	-1.10	-0.50	-0.17	-0.88
36	2.24	-0.28	+0.08	-0.35	+0.06
75	0.38	+0.70	+0.14	-0.08	+0.77
125	0.49	+0.02	0	-0.06	+0.08
175	4.37	0	-0.02	0	0
225	0.36	-1.43	-0.10	-0.09	-1.33
275	0.15	-0.60	+0.04	-0.05	-0.55

budget. We see that the terms for radiative and turbulent cooling are much smaller than the term for residual cooling at all levels. The horizontal advection dominates the residual term, which is very likely a result of the rapid change in the height of the inversion seen in Fig. 3.4.

The relatively small turbulent cooling rates presented in Table 3.2 agree with the model results of André et al. (1978) and Yamada and Mellor (1975). Other researchers have calculated layer-averaged temperature budgets in the nocturnal boundary layer for single-layer cases (Garratt and Brost, 1981; André and Mahrt, 1982). However, their calculations were performed in the nocturnal boundary layer, which is only a part of the nocturnal lower atmosphere. Within the boundary layer the temperature fluxes were more than an order of magnitude larger than the case presented here. Therefore, it is difficult to compare their results with those in Table 3.2.

The importance of advection and/or horizontal divergence of heat flux is clearly shown by the large values of the residual cooling listed in Table 3.2. The two-dimensional models cited above certainly do not apply to this fairly typical case studied at the BAO, which is located in rolling terrain. Realistic predictions for stable boundary layers must come from detailed three-dimensional models.

3.6 CONCLUSIONS

The above analysis indicates that the development and the structure of the stable nocturnal lower atmosphere are fairly complicated. Multiple layers are observed over both uniform and complex terrain and are most readily apparent in acoustic sounder records. They are also apparent in plots of the wind field, the temperature field, and the moisture field. Atmospheric and topographical factors contributing to such layering are many, but horizontal advection is involved in some way in their formation.

Because the Richardson number achieves its maximum value near the center of a low-level jet, there appears to be a rough correspondence between the profiles of Richardson number and mean wind speed. In the region between its maxima, Ri tends to be subcritical and $\bar{e}_h$ to be maximum. In the same region, the temperature field is fairly uniform, suggesting the region between two elevated layers is well mixed. The turbulent vertical fluxes of heat within elevated layers and near the ground surface are negative, but the vertical distribution of momentum flux is very complex.

The vertical distribution of radiative cooling rate in a nocturnal lower atmosphere shows warming nearest the surface and cooling aloft. Cooling was most pronounced at the top of the strong inversion layer near the surface ($z \approx 22$ m). The total heat budget for the multiple-layer case showed that the turbulent cooling rates were negligible compared with the radiative cooling, and both were much smaller than horizontal advection and/or subsidence.

3.7 ACKNOWLEDGMENTS

The authors appreciate the helpful suggestions received from W.D. Neff, D.H. Lenschow, and R.A. Brost in the preparation of this paper.

3.8 REFERENCES

André, J.C., G. DeMoor, P. Lacarrere, G. Therry, and R. Du Vachat, 1978: Modeling the 24-hour evolution of the mean and turbulent structures of the planetary boundary layer. J. Atmos. Sci., 35, 1861-1883.

André, J.C., and L. Mahrt, 1982: The nocturnal surface inversion and influence of clear-air radiative cooling. J. Atmos. Sci., 39, 864-878.

Blackadar, A.K., 1976: Modeling the nocturnal boundary layer. Preprints, 3rd Symposium Atmospheric Turbulence, Diffusion and Air Quality, Raleigh, N.C., 19-22 October 1976, American Meteorological Society, Boston, Mass., 46-49.

Brooks, D.L., 1950: A tabular method for the computation of temperature change by infrared radiation in the free atmospheres. J. Meteorol., 7, 313-321.

Brost, R.A., and J.C. Wyngaard, 1978: A model study of the stably stratified planetary boundary layer. J. Atmos. Sci., 35, 1427-1440.

Businger, J., and S.P.S. Arya, 1974: Heights of the mixed layer in the stably stratified planetary boundary layer. Advances in Geophysics, 18A, Academic Press, New York, 73-92.

Delage, Y., 1974: A numerical study of the nocturnal atmospheric boundary layer. Quart. J. Roy. Meteorol. Soc., 100, 351-364.

Garratt, J.R., and R.A. Brost, 1981: Long-wave radiation fluxes and the nocturnal boundary layer. J. Atmos. Sci., 38, 2730-2746.

Goff, R.C., 1976: Vertical structure of thunderstorm outflows. Mon. Wea. Rev., 104, 1429-1440.

Hootman, B., and W. Blumen, 1981: Observations of nighttime drainage flows in Boulder, Colorado during 1980. Preprints, 2nd Conference on Mountain Meteorology, Steamboat Springs, Colo., 9-12 November 1981, American Meteorological Society, Boston, Mass., 222-224.

Kaimal, J.C., and J.E. Gaynor, 1983: The Boulder Atmospheric Observatory. J. Clim. Appl. Meteorol. (accepted).

Li Xing-sheng, Liu Lin-gin, and Zheng Ai-ying, 1982a: Numerical studies of the development of the nocturnal boundary layer. Sci. Atmos. Sin. (accepted).

Li Xing-sheng, Zhu Cui-juan, Liu Lin-gin, Zheng Ai-ying, and Zhou Ming-yu, 1982b: A study on multiple layers wind speed profile in the planetary boundary layer. Sci. Atmos. Sin. (accepted).

Mahrt, L., R.C. Heald, D.H. Lenschow, B.B. Stankov, 1979: An observational study of the structure of the nocturnal boundary layer. Bound.-Layer Meteorol., 17, 247-264.

Neff, W.D., 1980: An observational and numerical study of the atmospheric boundary layer overlying the east Antarctic ice sheet. Ph.D. Thesis, University of Colorado, Boulder, Colo., 272 pp.

Rao, K.S. and H.F. Snodgrass, 1979: Some parameterizations of the nocturnal boundary layer. Bound.-Layer Meteorol., 17, 15-28.

Staley, D.O., 1965: Radiative cooling in the vicinity of inversions and the tropopause. Quart. J. Roy. Meteorol. Soc., 91, 282-301.

Sundararajan, A., 1979: Some aspects of the structure of the stably stratified atmospheric boundary layer. Bound.-Layer Meteorol., 17, 133-139.

Wyngaard, J.C., 1975: Modeling the planetary boundary layer--extension to the stable case. Bound.-Layer Meteorol., 9, 441-460.

Yamada, T., and G. Mellor, 1975: A simulation of the Wangara atmospheric boundary layer data. J. Atmos. Sci., 32, 2309-2329.

Zeman, O., 1979: Parameterization of the dynamics of stable boundary layers and nocturnal jets. J. Atmos. Sci., 36, 792-804.

4. A METHOD FOR MEASURING THE PHASE SPEED AND AZIMUTH OF GRAVITY WAVES IN THE BOUNDARY LAYER USING AN OPTICAL TRIANGLE

Li Xing-sheng and Lu Nai-ping
Institute of Atmospheric Physics
Academia Sinica
Beijing, China

J.E. Gaynor and J.C. Kaimal
NOAA/ERL/Wave Propagation Laboratory
Boulder, Colorado 80303

ABSTRACT. The phase speed and azimuth of gravity waves in the planetary boundary layer are calculated using an optical triangle. The results are compared with those calculated using a microbarograph array. The two methods are in essential agreement.

4.1 INTRODUCTION

Gravity waves, which are often synoptically generated, are frequently observed in the nocturnal stable boundary layer. Because of the rapid development of atmospheric remote sensing techniques in recent years, the temporal and spatial structure of gravity waves can be displayed and studied. Gossard and Richter (1970), Emmanuel et al. (1972), and Hooke et al. (1973), among others, have used sodars and FM-CW radars to monitor the physical characteristics of gravity waves and to study the interaction between the waves and turbulence. These authors have also studied the relationship between internal gravity waves and synoptic and mesoscale phenomena. The studies have considered the causes and the effects of the waves on mesoscale activity. The phase speed and the azimuth of gravity waves are very important to help understand their source. In these studies, the phase speed and the azimuth of gravity waves generally were measured using the time series data of three or more microbarographs. In addition, Gossard and Munk (1954) used single-point data for pressure and wind speed to compute the phase speed. Recently, Eymard and Weill (1979) have measured the phase speed and the azimuth of gravity waves (along with other characteristics) using a three-antenna Doppler sodar.

The following describes the calculations of some basic characteristics of the gravity waves utilizing an optical triangular array surrounding the 300-m meteorological tower at the Boulder Atmospheric Observatory (BAO) in Colorado. The wind speed measured by the optical systems is an average along the path (Lawrence et al., 1972). Therefore, high frequencies are automatically filtered. Because gravity waves are low-frequency phenomena by atmospheric boundary layer standards, the low pass filtering of the optical sensors may improve phase speed and direction estimations when compared with an array of microbarograph sensors. Measuring the horizontal divergence of the wind speed with an optical triangle (Kjelaas and Ochs, 1974; Tsay et al., 1980) has proved effective. With this information in mind, measuring the phase speed and azimuth of gravity waves with optical methods appears to be a reasonable approach.

4.2 MEASUREMENTS AND COMPUTATIONS

Three optical systems have been operating at BAO. The optical paths form an equilateral triangle, 450 m on a side (Fig. 4.1). Because the optical sensors measure the mean wind perpendicular to each path and positive outward from the triangle center (Lawrence et al., 1972), the sum of the readings of all three paths represents the average horizontal wind speed out from the triangle. The individual wind readings for each optical path, smoothed with a 10-s running average along with the scalar sum of all three, were recorded on digital tape. For the three optical systems, the horizontal area-average wind speed and the wind direction can be expressed as

$$\overline{V} = \left(\overline{V_E^2} + \overline{V_N^2} \right)^{1/2} \tag{4.1}$$

and

$$\theta = \tan^{-1} \frac{V_E}{V_N} + 180° + 4°, \tag{4.2}$$

where $\overline{V}_E$ and $\overline{V}_N$ are the wind components oriented to the east and north respectively, $\overline{V}_E = \frac{1}{\sqrt{3}} (V_{SE} - V_{SW})$, and $\overline{V}_N = \frac{2}{3} V_N - \frac{1}{3} (V_{SE} + V_{SW})$. V_N, V_{SE}, and V_{SW} are the wind components, transverse to the north, southeast, and southwest triangle sides repectively. In Eq. (4.2), adding 180° makes the northerly winds

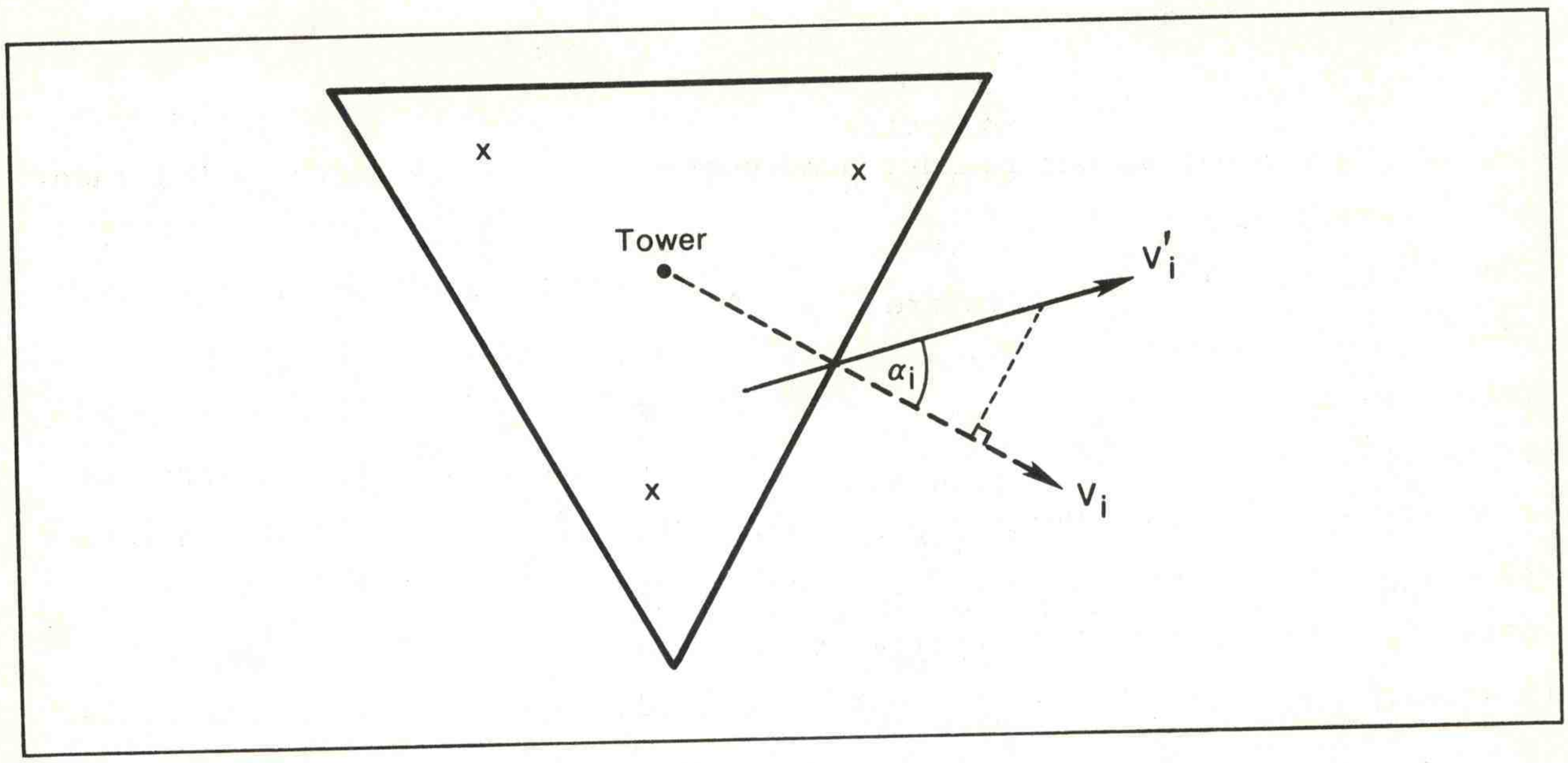


Figure 4.1.--Schematic of the optical triangle, the three microbarographs used in this analysis (x), and the BAO tower (•). V_i = wind component transverse to the triangle sides; V'_i = actual wind speed for each triangle side; α_i = angle between V_i and V'_i.

represent a 0° direction, and the 4° is an adjustment for the difference between the north path of the optical triangle and the true east-west direction. The wind directions θ correspond to the standard meteorological definition.

The theoretical wind-weighting function for a circular transmitter and receiver with circular apertures, 3.0 and 1.95 Fresnel zones in diameter, respectively, has its peak at the center of the path as shown in Fig. 4.2 (Ochs et al., 1976). The curve of the wind-weighting function also shows the minimum value near the transmitter and receiver along the optical path. Therefore, the average wind speed measured by optical systems is strongly weighted toward the center of the path, and it is assumed that a new triangle can be constructed by joining the center points of each optical path.

For each optical path, the actual wind speed at the center point of the path (Fig. 4.1) can be written

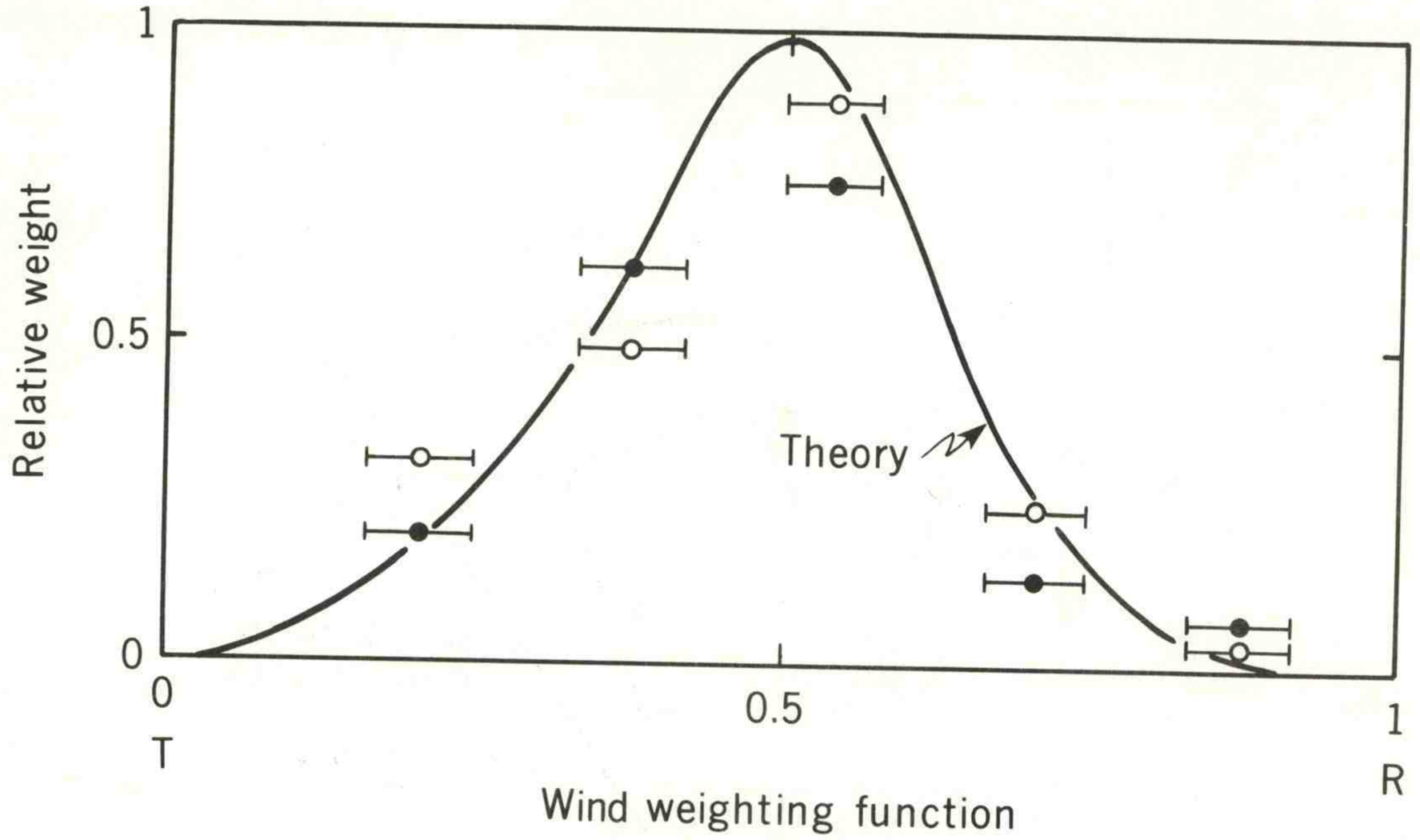


Figure 4.2.--Experimental wind-weighting function obtained by comparison of the optical measurement over a 500-m path with five pairs of anemometers arranged to measure the horizontal cross-wind component (from Ochs et al., 1976). T = transmitter; R = receiver.

$$V_i' = V_i/\cos\alpha_i \ , \qquad (4.3)$$

where V_i is the wind component transverse to the triangle sides, V_i' is the actual wind speed for each triangle side, the subscript i (= 1,2,3) represents the index of each side of the optical triangle, and α_i is the angle between the average wind direction and the wind component transverse to each triangle side. Because the average wind speed and wind direction change with time, the angle α_i is also time variable. The angles made with each side of the optical triangle may be instantaneously different. Therefore, with gravity wave propagation, the phase speed and direction appear as a variation in the time series of the actual wind speed for the three sides. The propagation of a wave across the three separate optical systems can be distinguished by the time delays between the three time series of wind speeds for pairs of optical stations. We can then obtain the phase difference between the pairs of optical stations for each frequency.

If the phase speed and the propagation direction of gravity waves are represented as c and γ respectively, then

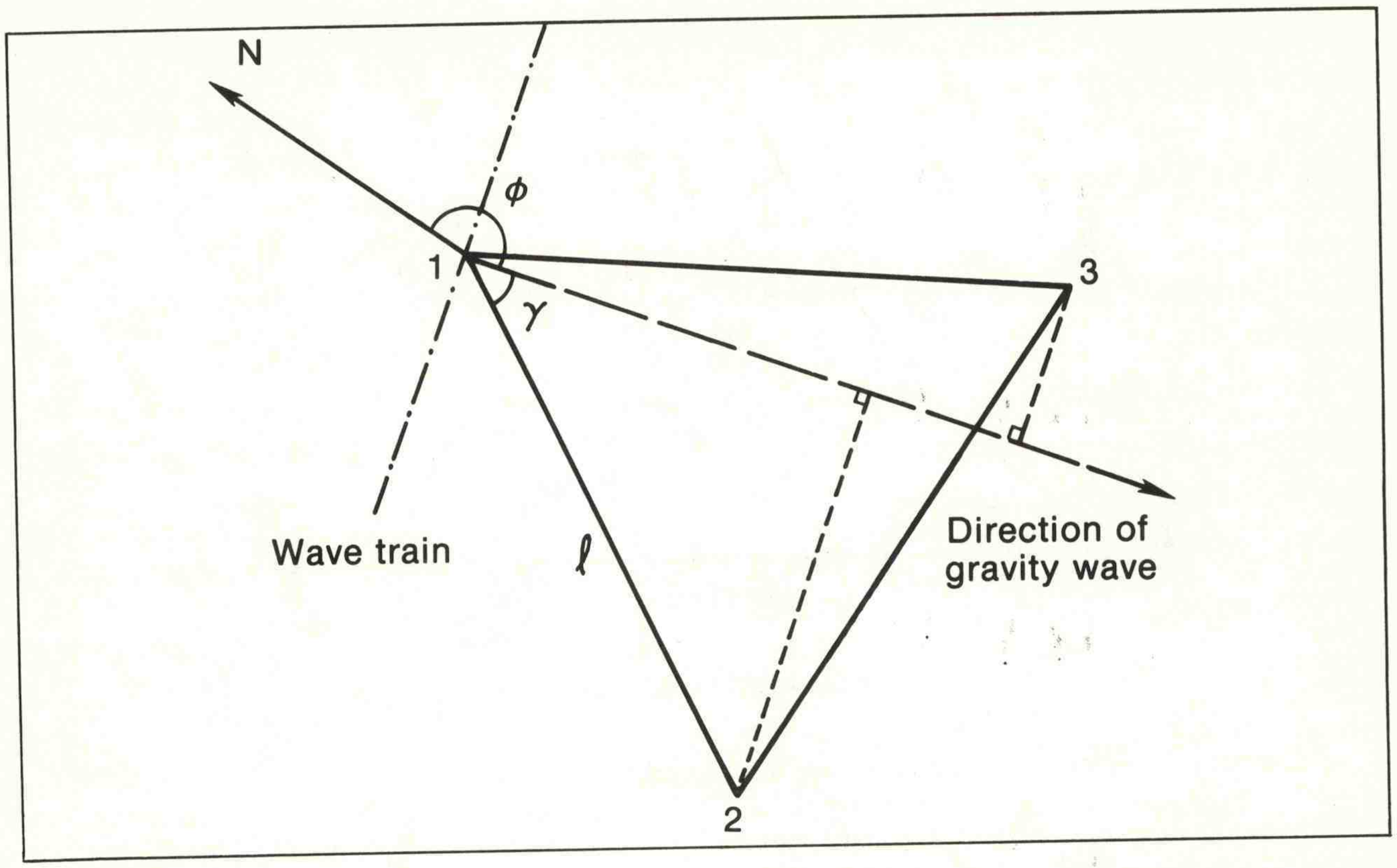


Figure 4.3.--Schematic of the geometry to determine the time delay with the three separate optical systems. γ = propagation direction of gravity waves; ϕ = azimuth; ℓ = length between the central points of the sides of the optical triangle.

$$\cos\gamma = c\ t_{12}/\ell \tag{4.4}$$

and

$$\cos(60° - \gamma) = c\ t_{13}/\ell, \tag{4.5}$$

where ℓ is the length between the central points of the sides of the optical triangle and t_{12} and t_{13} are the time delays from vertex 1 to vertex 2 and to vertex 3 respectively (Fig. 4.3). The corners of the triangle in Fig. 4.3 are at the center points of each optical path.

From Eqs. (4.4) and (4.5), c and γ can then be written

$$c = (\ell/t_{12})\ \sqrt{1 + \tan^2\gamma} \tag{4.6}$$

$$\gamma = \tan^{-1}\left[\frac{1}{\sqrt{3}}\left(\frac{2t_{13}}{t_{12}} - 1\right)\right], \tag{4.7}$$

with

$$\phi = 210° - \gamma \ , \tag{4.8}$$

where ϕ is the azimuth.

To calculate c and ϕ, we must derive the time delays t_{12} and t_{13}. If the time series of the wind speed is $V_1'(t)$ for vertex 1 and $V_2'(t)$ for vertex 2, the power spectrum is obtained by Fourier-transforming the auto-covariance function, and the cross spectrum is obtained by transforming the cross-covariance function between the two time series (Gossard and Hooke, 1975; Brigham, 1974). Therefore, the form of the cross-power spectrum for $V_1'(t)$, $V_2'(t)$ can be written as

$$E(\omega) = \int_{-\infty}^{\infty} \left[\int_{-\infty} V_1'(t)\ V_2'(t + \tau)\ dt \right] e^{-i\omega\tau}\ d\tau \ , \tag{4.9}$$

where τ is the time delay between time series, and $\omega = 2\pi f$, with f the frequency.

If $\sigma = t + \tau$, (4.9) becomes

$$E(\omega) = \int_{-\infty}^{\infty} V_1'(t)\ e^{i\omega t}\ H(\omega)\ dt \ , \tag{4.10}$$

where

$$H(\omega) = \int_{-\infty}^{\infty} V_2'(\sigma)\ e^{-i\omega\sigma}\ d\sigma \ . \tag{4.11}$$

Finally, from Eq. (4.10), the form of the cross-power spectrum can be written as

$$E(\omega) = H(\omega)\ [R(\omega) + iI(\omega)] \ , \tag{4.12}$$

where

$$R(\omega) = \int_{-\infty}^{\infty} V_1'(t)\ \cos(\omega t)\ dt \tag{4.13}$$

and

$$I(\omega) = \int_{-\infty}^{\infty} V_1'(t)\ \sin(\omega t)\ dt \ . \tag{4.14}$$

The phase relationship between frequencies for two cross-spectral analyzed time series is given by

$$\tan \omega\tau = I(\omega)/R(\omega) \ , \tag{4.15}$$

where $\tau = t_{12}$, in this case. The time delay t_{13} can be similarly calculated. The phase speed and direction of the gravity wave can be obtained by Fourier-transforming the auto-covariance function (from the time series of the wind speed) using Eqs. (4.12), (4.13), and (4.14) and solving Eqs. (4.6), (4.8), and (4.15).

4.3 RESULTS

Four gravity wave cases are presented. The first, between 0000 and 0700 MST on 13 November 1981 was embedded in strong stable stratification at the lower levels. The gravity wave train is shown in the acoustic record presented in Fig. 4.4. The phase speed and azimuth of the gravity waves have been calculated from 0210 to 0330 and from 0530 to 0650 MST. We first discuss the gravity wave occurring between 0210 and 0330 MST. The optical wind sensor was operating with a five-microbarograph array near the BAO tower. The three microbarographs closest to the tower were used for the analysis. Their locations relative to the optical triangle are presented in Fig. 4.1. The time series of the three microbarographs are shown in Fig. 4.5a. The coherence of the traces is quite high. The time series of the three optical systems are shown in Fig. 4.5b. Similarly, their coherence is very good. The mean spectrum of the three optical wind measurements is presented in Fig. 4.6a. The major peak is at a 34.1-min period. Two minor peaks are at 19- and 14.2-min periods. The phase speed and azimuth are 14.4 m/s and 200° respectively. The mean spectrum is also calculated for the same time period (Fig. 4.6b) using the three microbarographs. The major peak appears at a 28.4-min period with minor peaks at 19- and 14.2-min periods. The phase speed and azimuth of the major peak are 17.7 m/s and 225° respectively.

For the 0530 to 0650 MST time period (Fig. 4.4), the two sets of three time series (not shown) are also very coherent. Figures 4.7a,b indicate a similarity between the optical wind and microbarograph mean spectra with

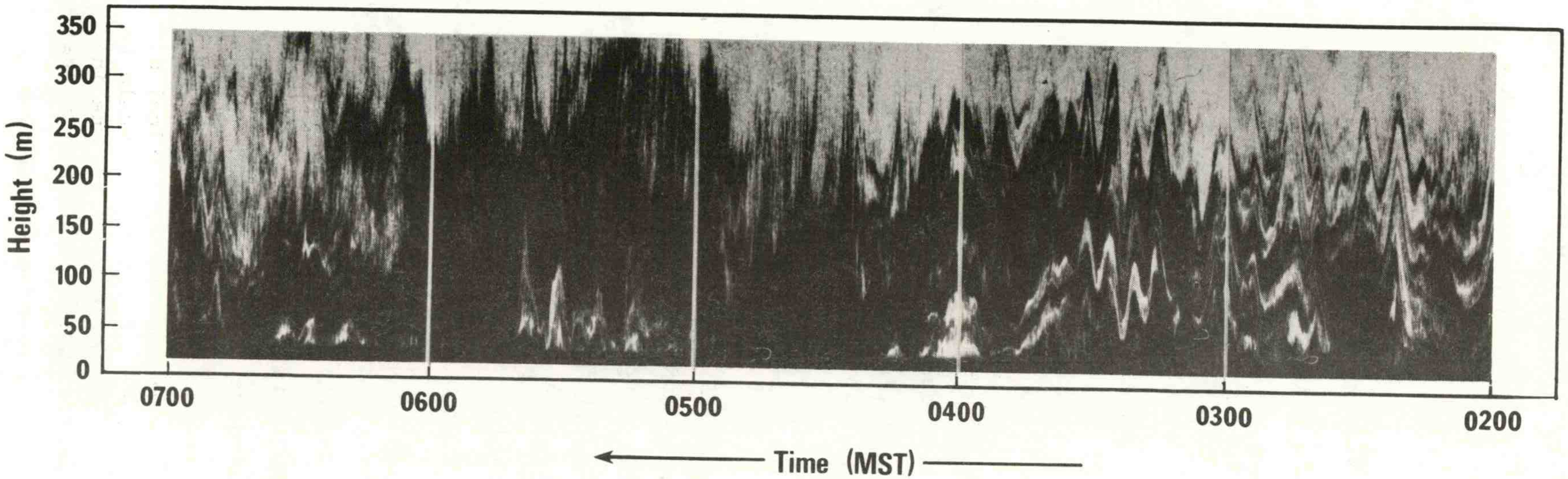


Figure 4.4.--Acoustic record between 0200 and 0700 MST on 13 November 1981.

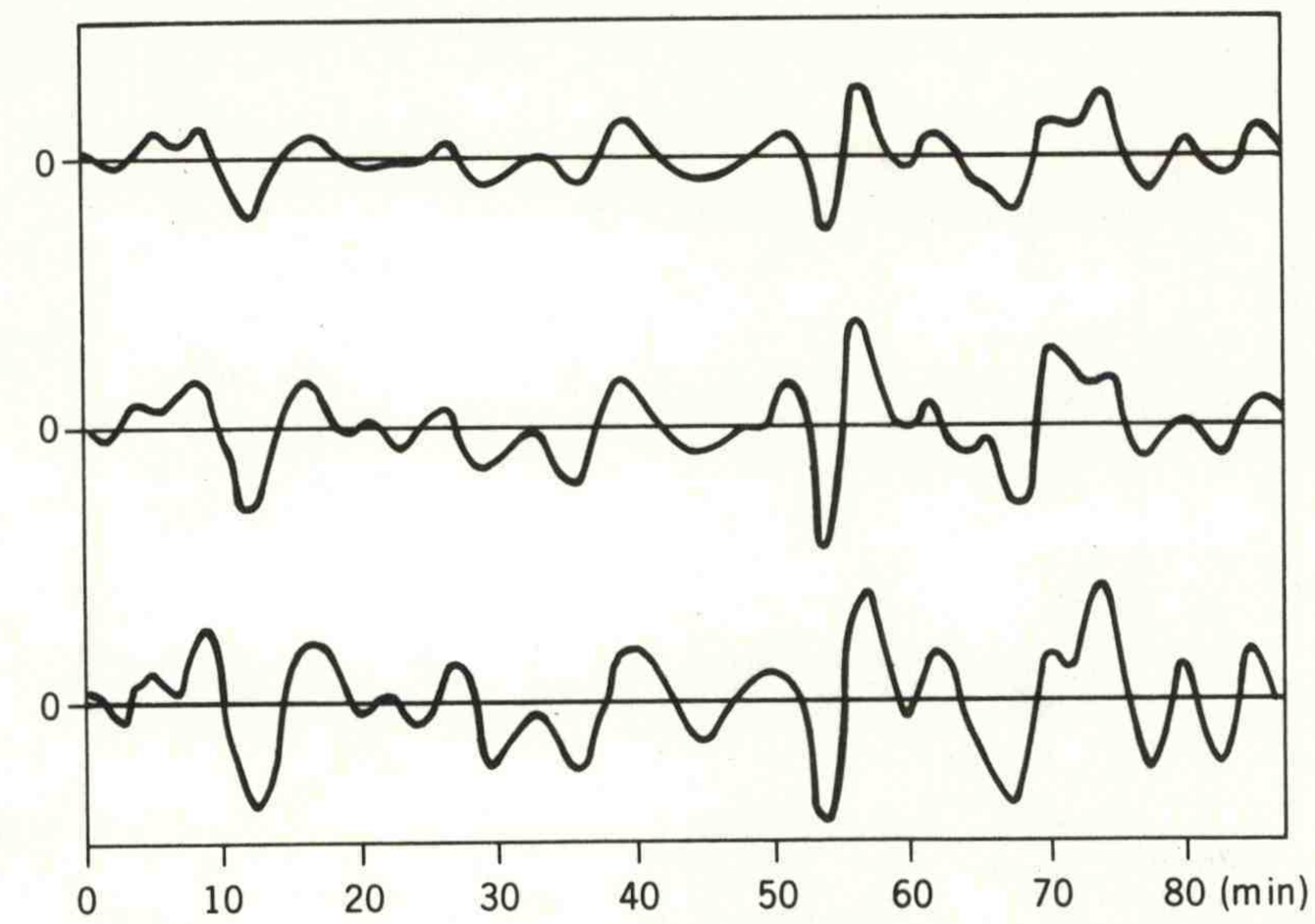


Figure 4.5a.--The time series of the three microbarographs between 0210 and 0335 MST on 13 November 1981. The vertical scale between two lines is 80 μb/s, and the curves are relative to a zero mean.

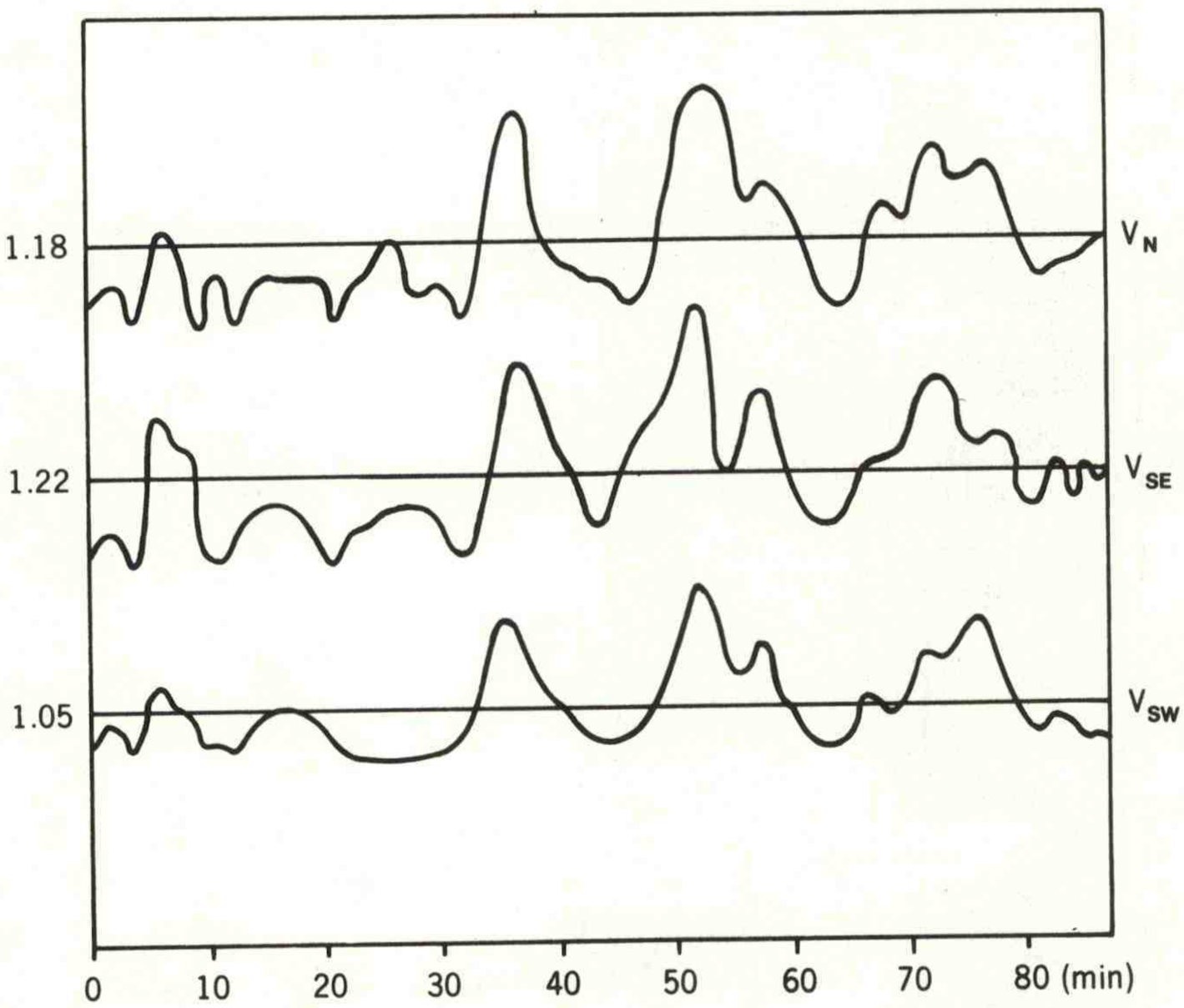


Figure 4.5b.--The time series for three separate optical systems from 0210 to 0335 MST on 13 November 1981. The vertical scale between two lines is 3 m/s, and the numbers on the far left are the individual means. V_N, V_{SE}, and V_{SW} are the wind components, transverse to the north, southeast, and southwest triangle sides, respectively.

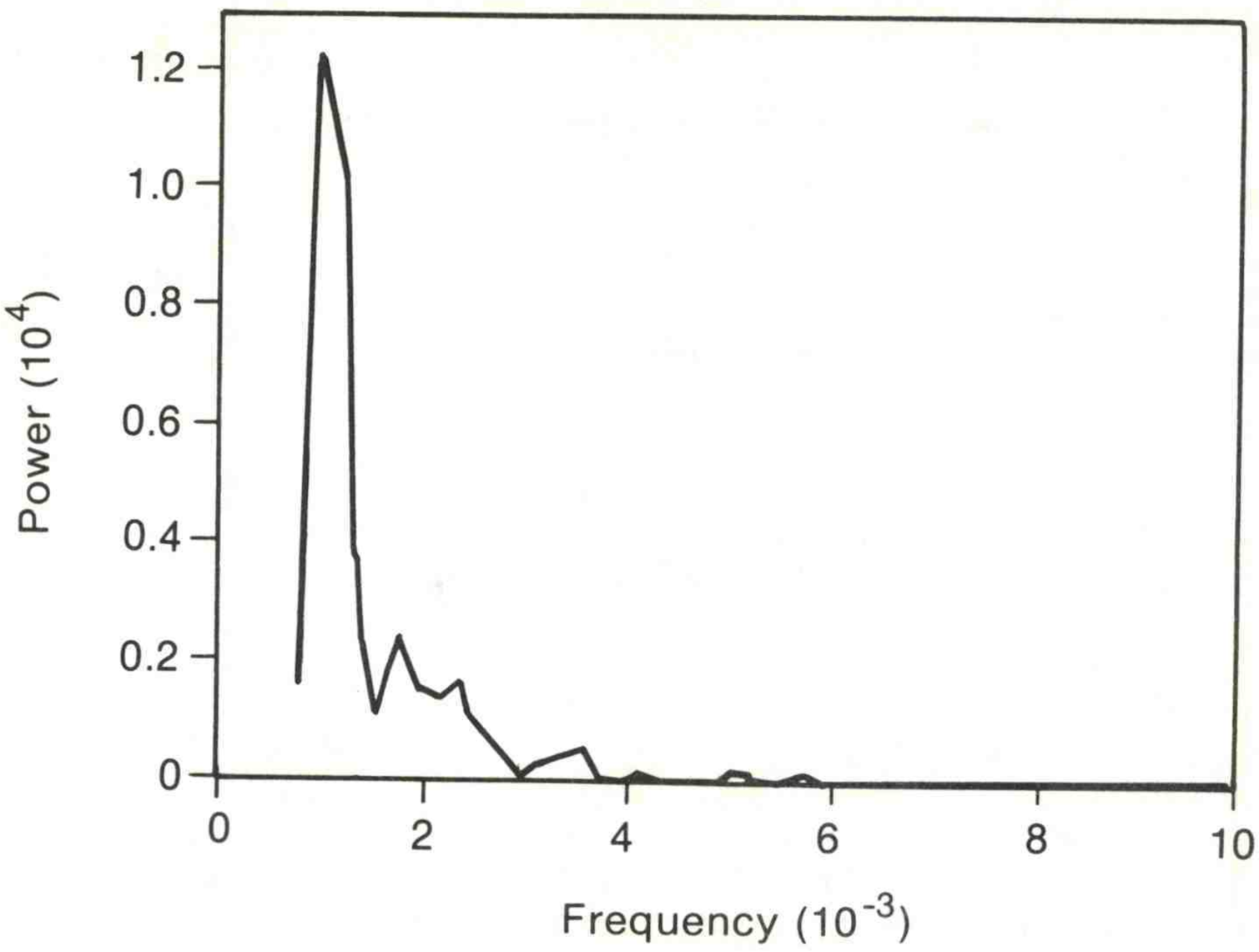


Figure 4.6a.--The mean spectrum calculated from the optical triangle data from 0210 to 0330 MST on 13 November 1981.

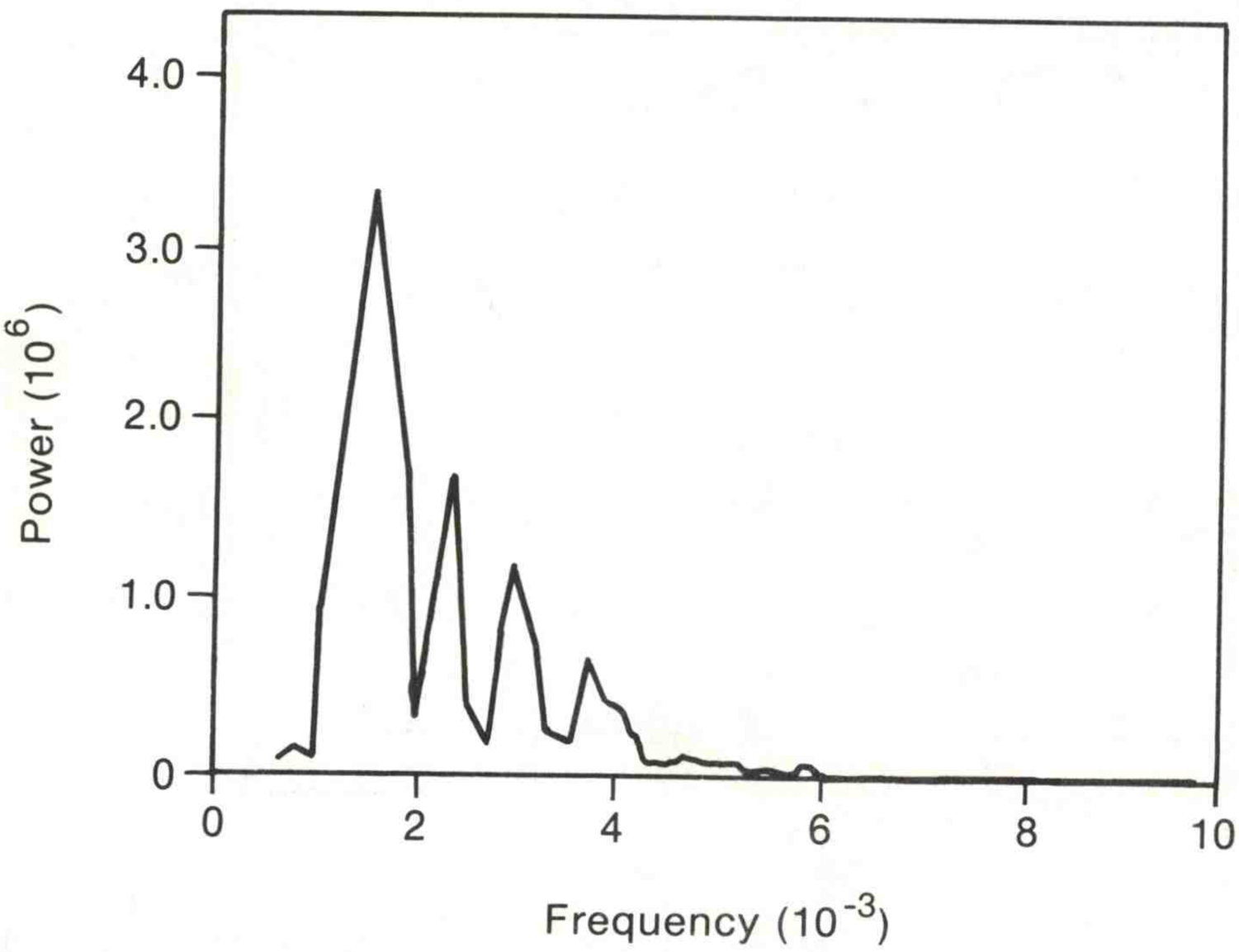


Figure 4.6b.--The mean spectrum calculated from the three microbarographs from 0210 to 0330 MST on 13 November 1981.

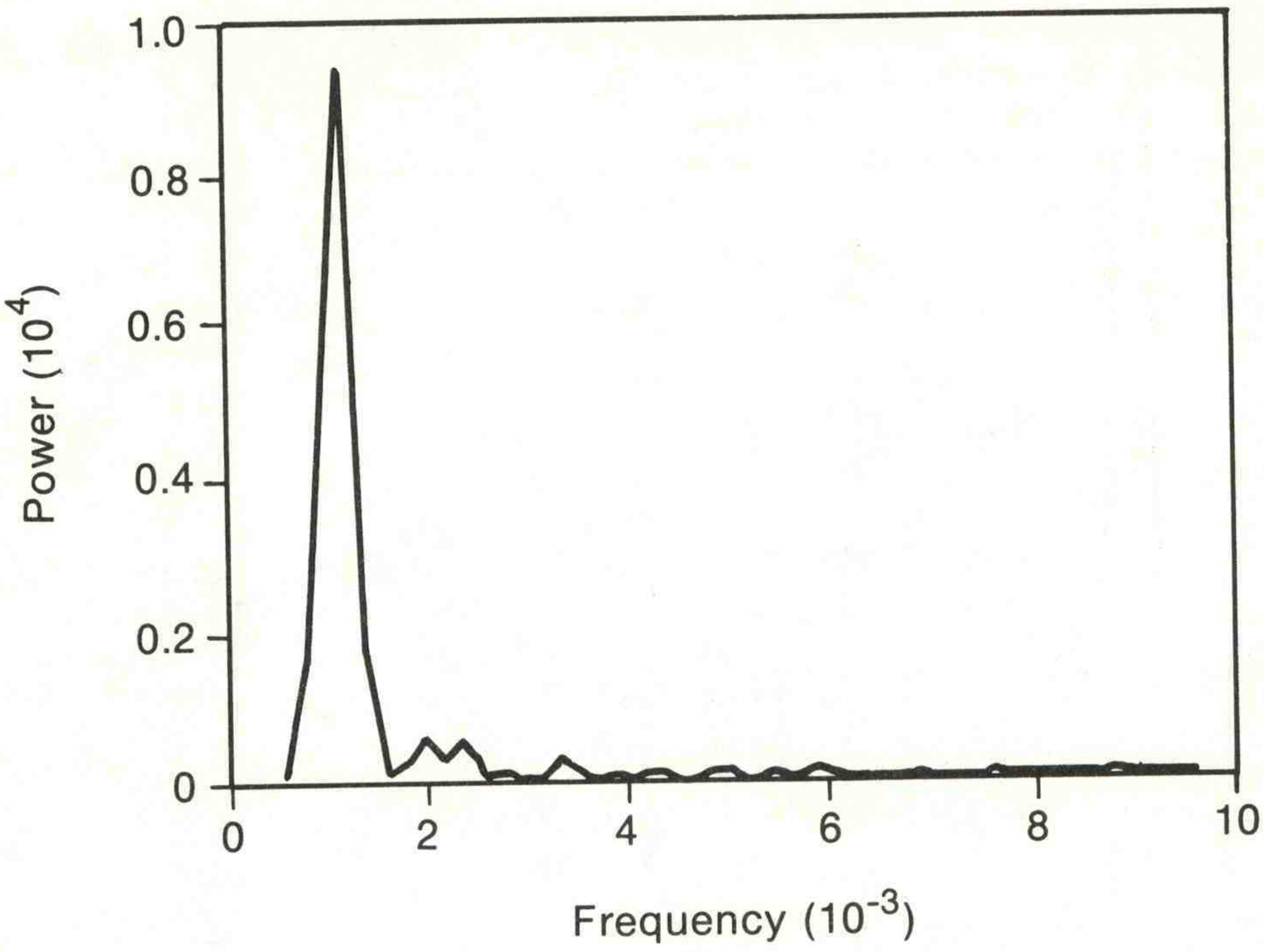


Figure 4.7a.--The mean spectrum calculated from the optical triangle data from 0530 to 0650 MST on 13 November 1981.

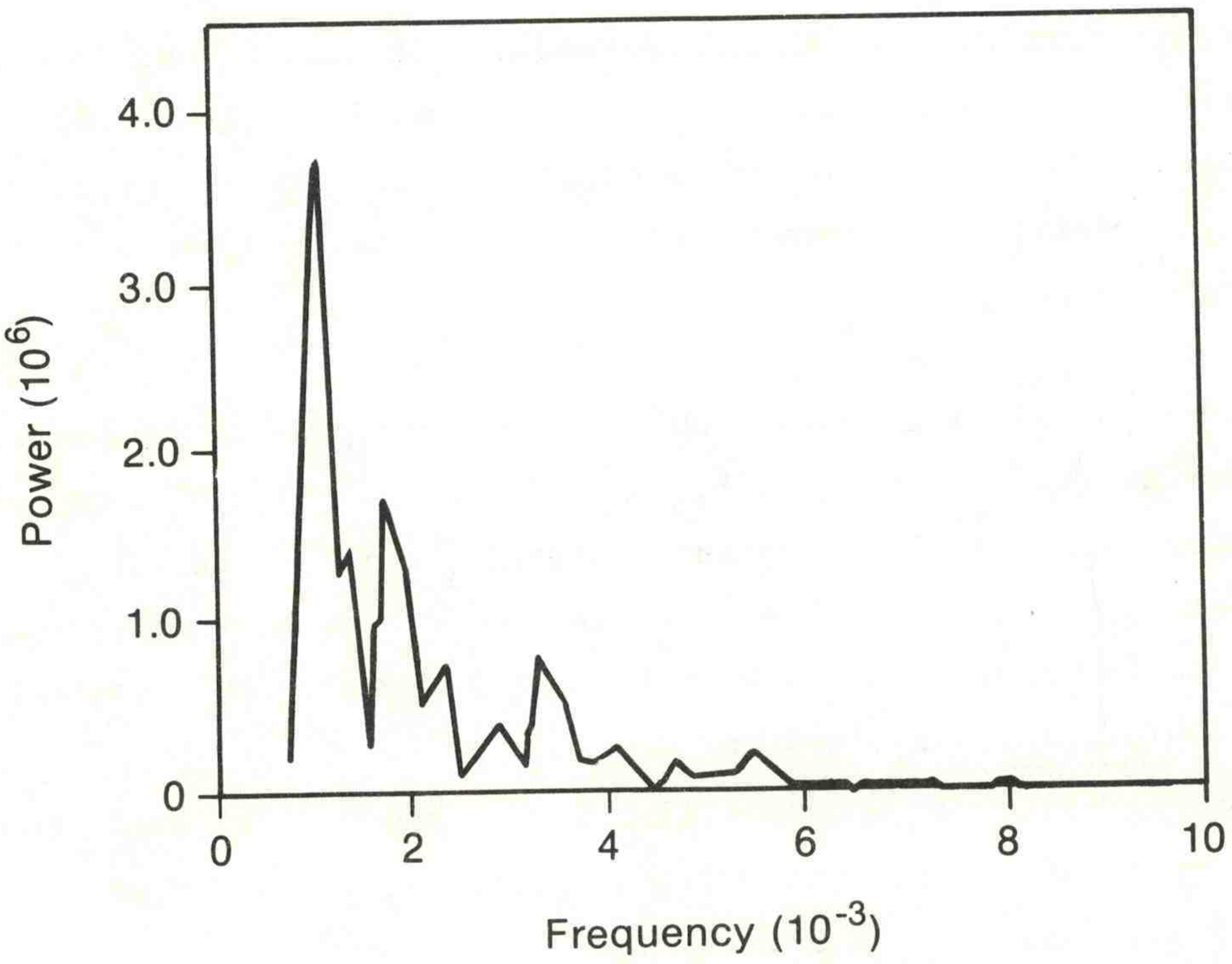


Figure 4.7b.--The mean spectrum calculated from the three micorbarographs from 0530 to 0650 MST on 13 November 1981.

Table 4.1.--Periods of spectral peaks, phase speeds, and azimuths calculated from the optical triangle (O) and microbarographs (M) for the four cases discussed

Date and time (MST)	Array	Periods of peaks (min)	Bandwidth of wave analysis (min)	Phase speed (m/s)	Azimuth (deg)
13 Nov. 1981	O	34.1, 19, 14.2	3.4-85.3	14.4	200
0210-0330	M	28.4, 19, 14.2	3.4-85.3	17.7	225
13 Nov. 1981	O	28.4, 21.3	3.4-34.1	10.0	254
0530-0650	M	24.4, 17.1	3.4-34.1	10.0	270
27 Oct. 1981	O	34.1, 24.4, 17.1	3.4-85.3	12.0	360
1940-2100	M	34.1, 24.4, 13.1	3.4-85.3	10.0	360
28 Oct. 1981	O	21.3, 14.2	3.4-85.3	11.6	296
0530-0650	M	21.3, 14.2, 12.2	3.4-85.3	10.0	270

respect to the major peaks. The phase speed from both the optical array and microbarograph is 10 m/s, and the azimuths are 254° and 270° respectively.

The two other gravity wave events analyzed occurred on 27 and 28 October 1981. A summary of results for these periods is given in Table 4.1 along with results for events of 13 November described above. The table indicates that the agreement of the phase speeds and directions between the two methods is quite good.

One disadvantage in using the optical triangle for gravity wave studies can be seen from Eq. (4.3) and Fig. 4.1. When the actual wind V_i' approaches a parallel direction with one of the optical paths ($\alpha_i \rightarrow 90°$), the wind becomes indeterminate for that path. In this situation, a data spike will appear in the V_i' data stream for that path. The spikes can be removed by interpolation using the acceptable points on either side.

As mentioned earlier, the spatial filtering of the optical array can be an advantage. One advantage to this built-in filtering is in the use of the impedance relation (Gossard and Munk, 1954),

$$\frac{\omega}{k} = \frac{p'(z)}{\rho_o(z)u'(z)} - U_{ok}(z) \ , \qquad (4.16)$$

where both the background wind U_{ok} and the wave-associated departure of the wind u' can be measured with the optical triangle. In Eq. (4.16), p' is the wave-perturbed pressure, ρ_o the mean density, and k the wave number. Often, using a time series of the wind from a single point sensor presents a difficult filtering problem in ascertaining a proper u'. The optical triangle winds alleviate many of the filtering problems (E.E. Gossard; NOAA/ERL/WPL; private communication).

However, the spatial filtering of the optical winds can also present a limitation not associated with the microbarograph technique. Waves with wave lengths equal to or smaller than the averaging distance (450 m) will be filtered out completely using the optical technique. Wave lengths slightly longer than 450 m will be filtered considerably depending on the filter function of the unit. For the major peaks analyzed in this study, all of the wavelengths are significantly longer than 450 m. A comparison of the optical wind and microbarograph spectra in Figs. 4.6 and 4.7 shows how the spatial filtering with the optical triangle affects the higher frequencies.

4.4 CONCLUSIONS

The phase speeds and directions of gravity waves are possible to calculate, within the limits of the spatial averaging and nonparallel wind directions, using an optical triangle wind-measuring system. The results agree quite well with those from a microbarograph array. Some of the differences between the optical wind spectra and microbarograph spectra can be explained by optical wind spatial filtering. The advantages of the optical triangle over a microbarograph array include the inherent spatial averaging of the optical triangle. The spatial filtering can be a disadvantage for wavelengths near the pathlength.

A discussion of the connection between wave-induced pressure fluctuations and wave-induced wind fluctuations near the ground under statically stable conditions is beyond the scope of this work. However, consideration of such a connection is important to assess the ultimate applicability of optical wind sensing to atmospheric gravity wave measurement.

4.5 ACKNOWLEDGMENTS

The authors wish to thank E.E. Gossard and W.D. Neff for their helpful suggestions during preparation of this paper.

4.6 REFERENCES

Brigham, E.O., 1974: The Fast Fourier Transform. Prentice-Hall, Englewood Cliffs, N.J., 252 pp.

Emmanuel, C.B., B.R. Bean, L.G. McAllister, and J.R. Pollard, 1972: Observations of Helmholtz waves in the lower atmosphere with an acoustic sounder. J. Atmos. Sci., 29, 889-892.

Eymard, L., and A. Weill, 1979: A study of gravity waves in the planetary boundary layer by acoustic sounding. Bound.-Layer Meteorol., 17, 231-245.

Gossard, E.E., and W.H. Hooke, 1975: Waves in the Atmosphere. Elsevier, New York, 456 pp.

Gossard, E.E., and J.H. Richter, 1970: Internal waves in the atmosphere from high-resolution radar measurements. J. Geophys. Res., 75, 3523-3536.

Gossard, E.E., and W.H. Munk, 1954: On gravity waves in the atmosphere. J. Meteorol., 11, 259-269.

Hooke, W.H., F.F. Hall, and E.E. Gossard, 1973: Observed generation of an atmospheric gravity wave by shear instability in the mean flow of the planetary boundary layer. Bound.-Layer Meteorol., 4, 511-523.

Kjelaas, A.G., and G.R. Ochs, 1974: Study of divergence in the boundary layer using optical propagation techniques. J. Appl. Meteorol., 13, 242-248.

Lawrence, R.S., G.R. Ochs, and S.F. Clifford, 1972: The use of scintillations to measure average wind across a light beam. Appl. Opt., 11, 239-243.

Ochs, G.R., S.F. Clifford, and Ting-i Wang, 1976: Laser wind sensing: the effects of saturation of scintillation. Appl. Opt., 15, 403-408.

Tsay, M.K., Ting-i Wang, R.S. Lawrence, G.R. Ochs, and R.B. Fritz, 1980: Wind velocity and convergence measurements at the Boulder Atmospheric Observatory using path-averaged optical wind sensors. J. Appl. Meteorol., 19, 826-833.

5. RICHARDSON NUMBER COMPUTATIONS IN THE PLANETARY BOUNDARY LAYER

R.J. Zamora*
Department of Meteorology
Metropolitan State College
Denver, Colorado 80204

ABSTRACT. This paper focuses on a method of calculating the gradient Richardson number Ri using data gathered at the Boulder Atmospheric Observatory, a 300-m meteorological tower located 30 km north of Denver, Colorado, and presents a case study of Richardson number (Ri) behavior at the 75-m level of the tower during an active acoustic-gravity wave event. Ri is found to be modulated by the gravity wave activity in addition to longer period oscillations that might be a result of inertial wave activity.

5.1 INTRODUCTION

Recent experiments conducted by NOAA/ERL/WPL have focused on the structure of the stable planetary boundary layer (PBL). One of the more important parameters used to quantitatively estimate the dynamic stability of such a fluid environment is the gradient Richardson number Ri. This has long been regarded as an important criterion for the onset of turbulence in a stably stratified fluid. Fluid parcels can be moved vertically against the force of gravity if sufficient kinetic energy is available in the velocity field.

Ri represents the ratio of work needed to bring about the exchange to the kinetic energy present to do the work. In general if Ri > 0.25 through the fluid, the fluid is assured to be stable everywhere. These results were obtained by Miles (1961) and Howard (1961) for incompressible fluids, and the proof was later extended to compressible fluids by Chimonas (1970).

Although the Richardson number is of great theoretical importance, it is a difficult parameter to calculate. In its usual form for atmospheric applications (Gossard and Hooke, 1975),

---

* Present affiliation: NOAA/ERL/Wave Propagation Laboratory, Boulder, Colorado 80303.

$$Ri = \frac{N^2}{(\frac{\partial \vec{U}}{\partial z})^2} \quad , \tag{5.1}$$

with

$$N^2 = \frac{g}{\theta} \frac{\partial \theta}{\partial z} \quad , \tag{5.2}$$

where g is the gravitational acceleration, N the Brunt-Väisälä frequency, θ the potential temperature, z the vertical Cartesian coordinate, $\vec{U}$ the horizontal wind vector, and $\bar{\theta}$ the mean potential temperature over the gradient.

To fully appreciate the difficulty in calculating Ri, assume Ri = 0.25, a typical value in a stable layer with shear, and $(\partial \vec{U}/\partial z)^2 = 0.004$, a moderate value. Then

$$\frac{\partial \theta}{\partial z} = 1.5 \times 10^{-3} \ ^\circ C/m \ .$$

These correspond to differences of approximately 0.05°C and 0.2 m/s over 50-m Δz. Although it is possible to measure these differences with present BAO instrumentation, it must be noted that absolute calibration errors can bias the calculations, and aliasing due to the finite difference scheme can yield poor results. Thus, in cases where the wind shears and temperature gradients are weak, the limitations of instrumentation are most likely to be apparent in the calculations.

In calculating Ri it is commonly assumed that the atmosphere is dry. If the gradient of θ in the layer over which the Richardson number is calculated is less than zero, the atmosphere is statically unstable and any perturbation in the atmosphere will grow. In this case the Richardson number is of little significance since the energy contained in the velocity field is not necessary for vertical parcel exchange. If the gradient of potential temperature is greater than zero, a restoring force exists and a displaced parcel will oscillate about its equilibrium position with a frequency equal to N in the absence of viscous damping. Since the potential temperature of a parcel depends only on pressure and temperature, errors can be introduced into Ri computations if the density of the parcel is assumed to depend only on the dry air pressure and temperature of the parcel.

In an attempt to relax the assumption of a dry atmosphere, the virtual temperature of a parcel can be substituted into the potential temperature equation, and in turn this virtual potential temperature can be used to calculate a density-adjusted static stability term and thus adjust Ri for the effect of moisture in the atmosphere.

The preceding stability analysis remains valid until the atmosphere reaches saturation, at which time the parcel cools at the moist adiabatic lapse rate. It has been demonstrated (Lalas and Einaudi, 1973) that at this point a new Brunt-Väisälä frequency must be used to describe parcel buoyancy adequately. This paper does not address the problem of dynamic stability in a saturated atmosphere, or after condensation has occurred.

To examine the behavior of the Richardson number in the lower atmosphere a data set was chosen from a period of active acoustic-gravity wave propagation beginning on the evening of 6 November 1981 at about 2000 MST and ending on 7 November 1981 at 0400 MST at the Boulder Atmospheric Observatory (BAO). BAO is located 20 km east of Boulder on gently rolling terrain.

5.2 GOVERNING EQUATIONS

5.2.1 Dry Atmosphere

The gradient Richardson number is given by (5.1), where (5.2) represents the static stability of the atmosphere, and

$$\left|\frac{\partial \vec{U}}{\partial z}\right|^2 = \left(\frac{du}{dz}\right)^2 + \left(\frac{dv}{dz}\right)^2 \quad . \tag{5.3}$$

This expression for the change in wind shear with height takes into account both the directional and speed shears of the wind vector:

$$\vec{U} = u\hat{i} + v\hat{j} \quad . \tag{5.4}$$

The parcel potential temperature θ is given by

$$\theta = T\left(\frac{1000}{p}\right)^{\kappa} \quad , \tag{5.5}$$

where $\kappa = 0.286$, T is the Kelvin temperature of the parcel, and p is the atmospheric pressure in millibars.

5.2.2 Moist Atmosphere

The density-adjusted Richardson number Ri_v is

$$Ri_v = \frac{N_v^2}{\left(\frac{\partial \vec{U}}{\partial z}\right)^2} \quad , \tag{5.6}$$

where

$$N_v^2 = \frac{g}{\overline{\theta}_v} \frac{\partial \theta_v}{\partial z} \quad , \tag{5.7}$$

$$\overline{\theta}_v = \frac{\theta_{v_1} + \theta_{v_2}}{2} \quad ,$$

and virtual potential temperature θ_v is given by Fleagle and Businger (1980) as

$$\theta_v = T^* \left(\frac{1000}{p}\right)^{\kappa} \quad . \tag{5.8}$$

T^* is given by Hess (1959) as

$$T^* = T \frac{1 + q/\varepsilon}{1 + q} \quad , \tag{5.9}$$

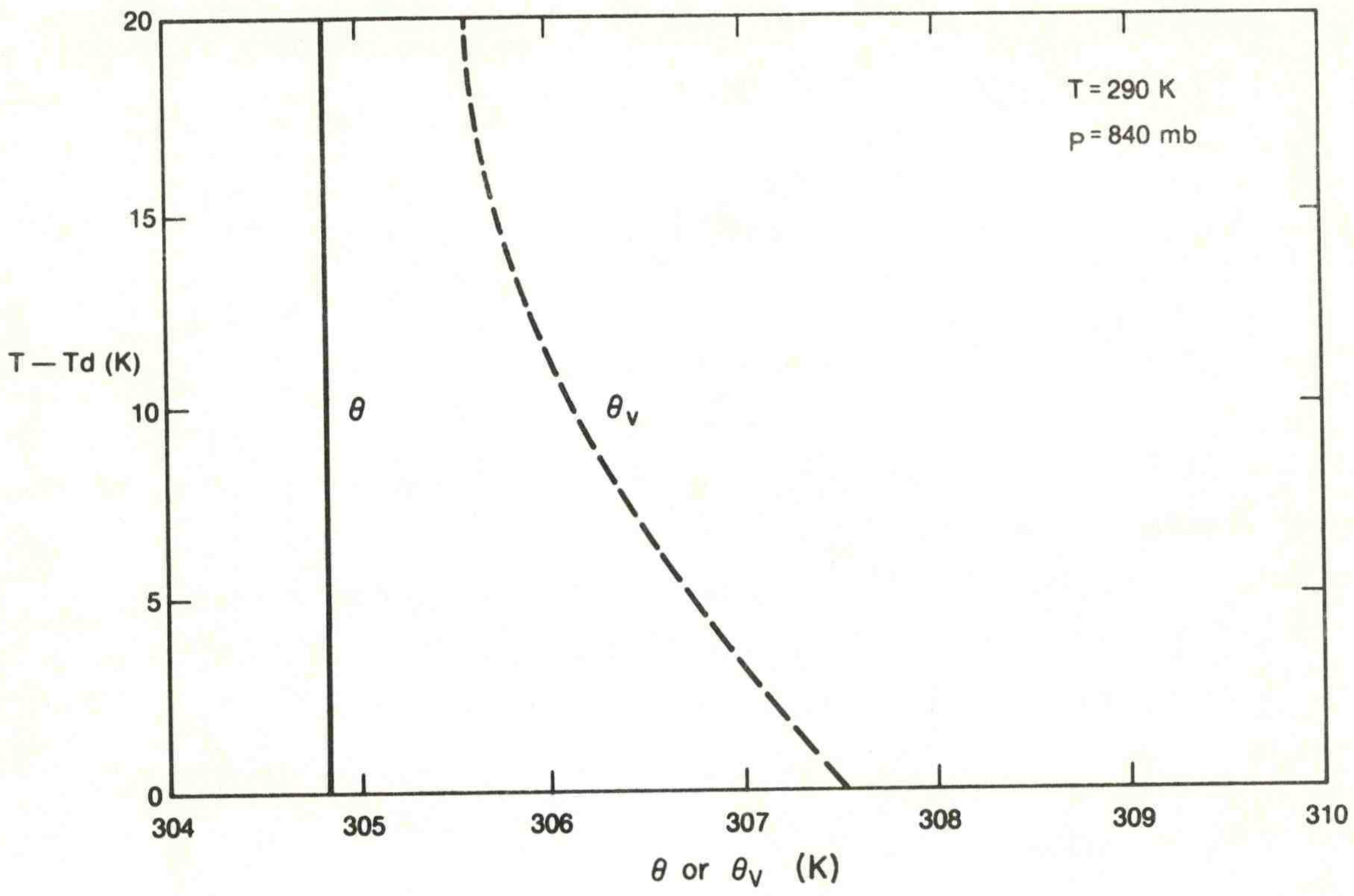
where q, the mixing ratio, is

$$q = \varepsilon \frac{e}{p - \varepsilon} \quad , \tag{5.10}$$

with $\varepsilon = 0.622$.

The vapor pressure e of the parcel is given by Murray (1967) as

$$e = 6.1078 \exp\left[\frac{a(T_d - 273.16)}{T_d - b}\right] \quad , \tag{5.11}$$



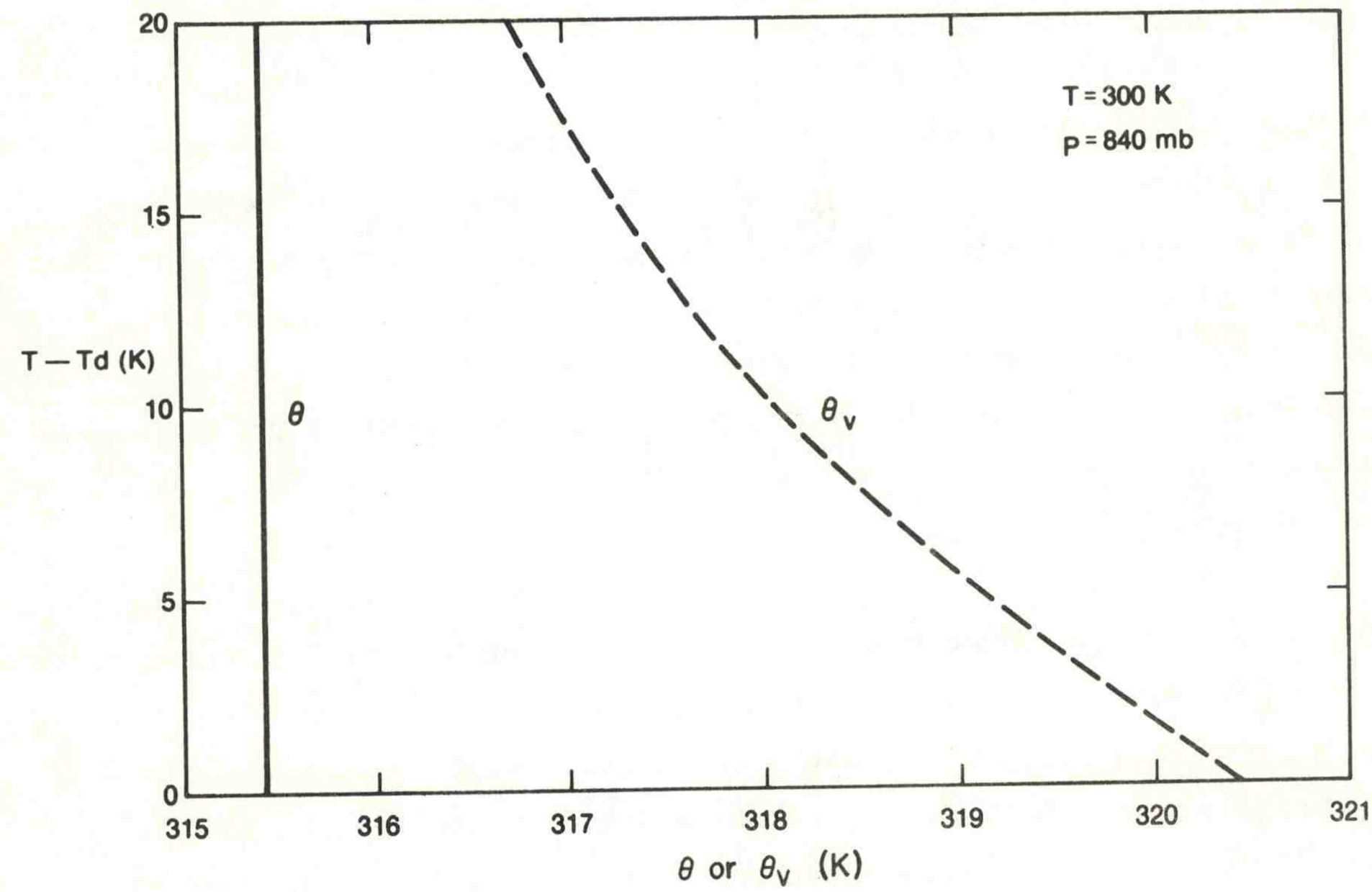


Figure 5.1.--θ and θ_v vs. $T-T_d$ for constant values of p and T.

where

$$\left.\begin{aligned} a &= 21.8745584 \\ b &= 7.66 \end{aligned}\right\} \text{ over ice,}$$

$$\left.\begin{aligned} a &= 17.2693882 \\ b &= 35.86 \end{aligned}\right\} \text{ over water,}$$

T_d is the parcel dewpoint.

The use of θ_v in (5.7) allows the computation of a more realistic Richardson number because the static stability of the atmosphere is no longer assumed to be a function of p and T only. Figure 5.1 illustrates the differences between θ and θ_v for increasing T_d at constant values of p and T. This adjustment is negligible at low temperatures because e is typically small.

5.3 COMPUTATIONAL SCHEME

5.3.1 Instrumentation and Calibration

The BAO facility includes a 300-m meteorological tower instrumented at eight levels as shown in Fig. 5.2. Standard instrumentation at each level includes fast-response wind measurements by sonic anemometers, slow-response wind measurements using R.M. Young propeller-vane (propvane) anemometers, mean temperatures using Hewlett-Packard quartz thermometers in an aspirated shield, mean dewpoints using EG&G 110 Dewpoint Hygrometers, and fast-response temperatures using platinum wire thermometers. A full description of BAO is given by Kaimal and Gaynor (1983).

For the purpose of Richardson number calculation the propvane anemometers were chosen for velocity field measurements, and the mean temperature and dewpoint sensors were chosen to measure the thermodynamic variables. These choices were made for operational reasons. Since Ri involves the gradients $\partial\theta/\partial z$ and $\partial\vec{U}/\partial z$, the absolute calibrations must be as accurate as possible. The propvane anemometers, and mean-temperature and mean dewpoint sensors, offered the most accurate absolute calibration. The mean-temperature sensors are periodically placed in a precision temperature bath and intercompared. The dewpoint hygrometers are calibrated with precision resistors and are

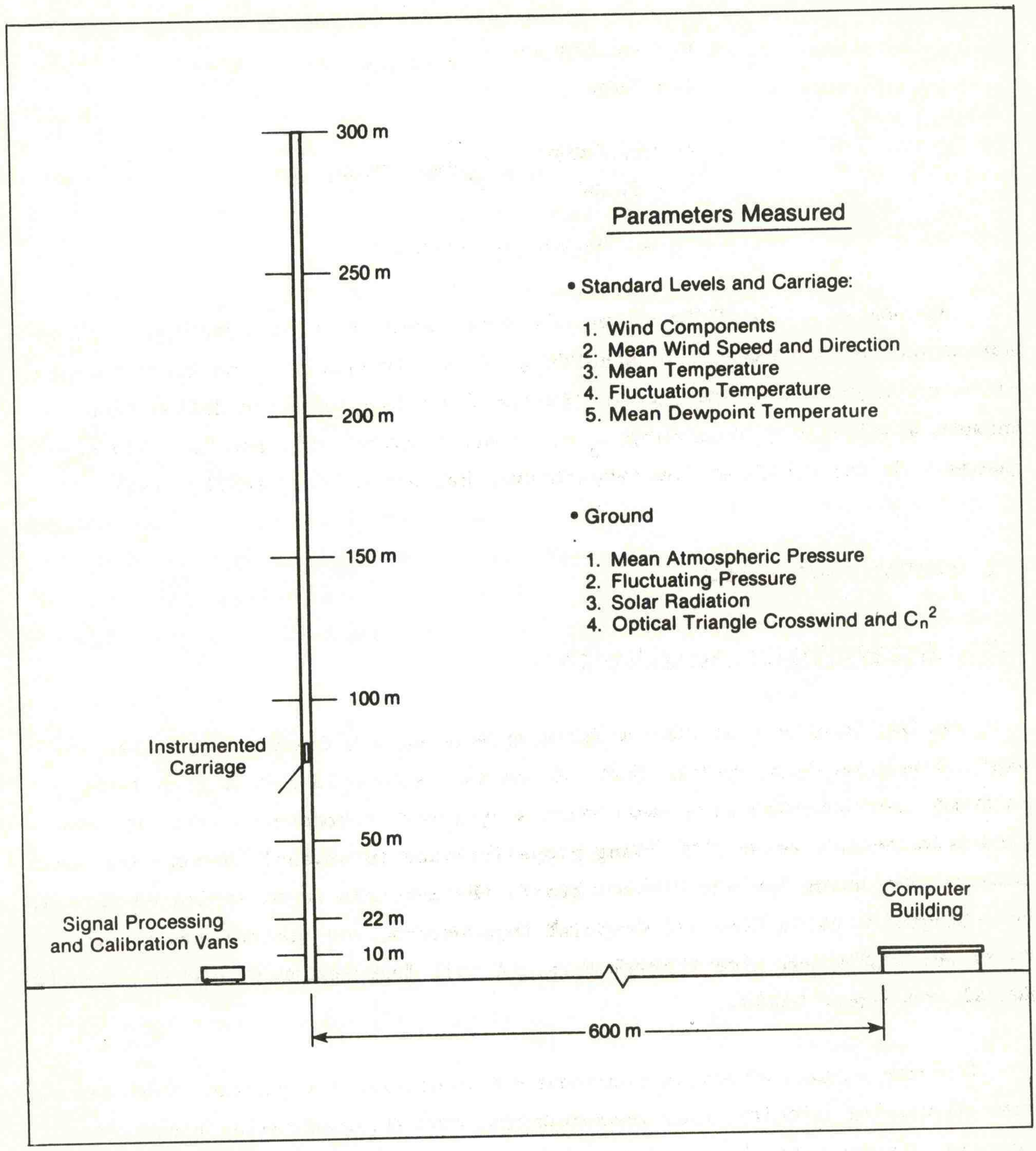


Figure 5.2.--BAO tower, showing the location of fixed levels and the parameters measured.

cleaned periodically to maintain precision. The propvane anemometers are calibrated using a constant rpm motor for speed and are oriented with respect to the supporting boom for azimuth.

The accuracies for the respective measurements are

$\pm$ 0.05°C for temperature,

$\pm$ 0.5°C for dewpoint,

$\pm$ 0.1 m/s for speed,

$\pm$ 1° for azimuth.

5.3.2 The Algorithm

To calculate the Richardson number, an interactive program, which resides in the permanent library of the BAO PDP 11/70 computer, was written by the author. The source code is written in Fortran IV. The program allows the input quantities to be averaged over variable increments of time and allows the option of calculating Ri or Ri_v.

Calculation of q, θ, and θ_v requires knowledge of p at each tower level, but p is measured only at the surface. Thus, the hypsometric equation (Hess, 1959) is solved in the form

$$p_2 = \exp \left\{ \left[- \frac{0.034}{\bar{T}^*} (z_2 - z_1) \right] + \ell n \, p_1 \right\}, \qquad (5.12)$$

where $\bar{T}^* = (T_1^* + T_2^*)/2$, z_2 and z_1 are the tower levels chosen, and p_1 = surface pressure. Because T^* also requires knowledge of p at each level, (5.12) cannot be solved directly.

Instead, the mean temperature $\bar{T}$ is substituted for $\bar{T}^*$ in (5.12) and this approximate equation is solved for p at each tower level. This first guess is then used to compute q and T^* for the tower levels.

After this step is completed, (5.12) is then solved again obtaining a corrected p for levels one through eight. This p is then used in successive calculations.

The partial derivatives $\partial\theta/\partial z$, $\partial\theta_v/\partial z$, and $\partial\vec{U}/\partial z$ are approximated by centered differences as

$$\frac{\partial\theta}{\partial z} \doteq \frac{\theta_2 - \theta_1}{z_2 - z_1} ,$$

$$\frac{\partial\theta_v}{\partial z} \doteq \frac{\theta_{v_2} - \theta_{v_1}}{z_2 - z_1} \qquad (5.13)$$

and

$$\left|\frac{\partial\vec{U}}{\partial z}\right|^2 \doteq \left[\frac{(u_2 - u_1)^2}{(z_2 - z_1)^2} + \frac{(v_2 - v_1)^2}{(z_2 - z_1)^2}\right] . \qquad (5.14)$$

5.4 ERROR ANALYSIS

To test the sensitivity of the algorithm to experimental and truncation error, a separate version of the program was created in which the errors given in Sec. 5.3.1 were added to the measured quantities. The differences between the two computer runs are as follows:

$$\Delta Ri_v = 0.007$$
$$\Delta Ri = 0.008 .$$

Hence, the estimates of Ri_v and Ri are accurate to $\pm$ 0.007 and $\pm$ 0.008 respectively. Much larger errors are possible if the differences in wind velocity and temperature over the layer in question exceed the limits of the sensor.

5.5 ANALYSIS

The echo patterns from an acoustic sounder located near the tower (Fig. 5.3) were used to determine the onset of wave activity, and the Richardson number was computed between the 50- and 100-m levels of the tower starting at 2000 MST on 6 November 1981 and ending at 0420 on 7 November 1981, for an averaging period of 5 min using the algorithm of Sec. 5.3.2. A histogram of the distribution of Ri_v for the period is shown in Fig. 5.4.

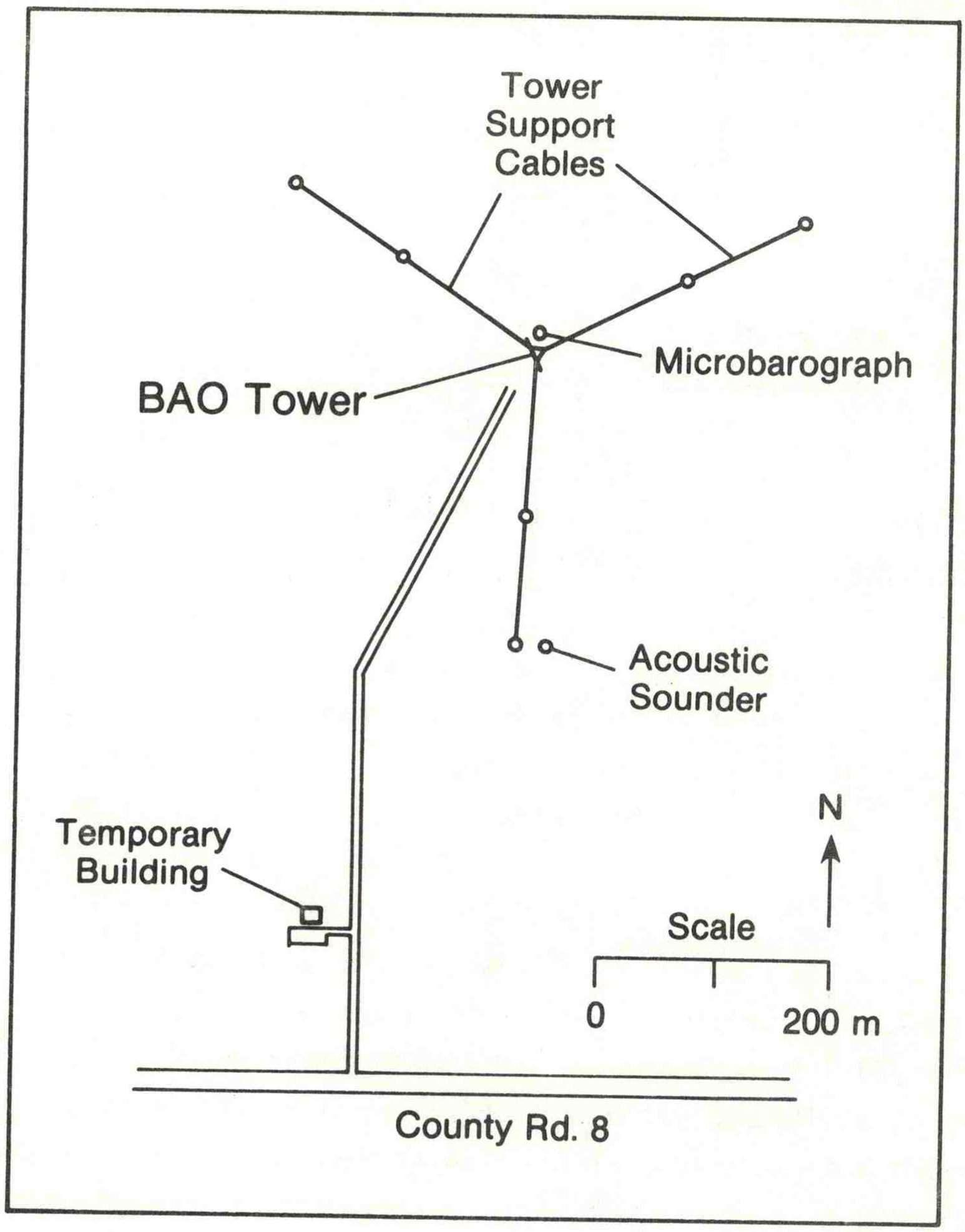


Figure 5.3.--BAO facility showing the location of the acoustic sounder and microbarograph.

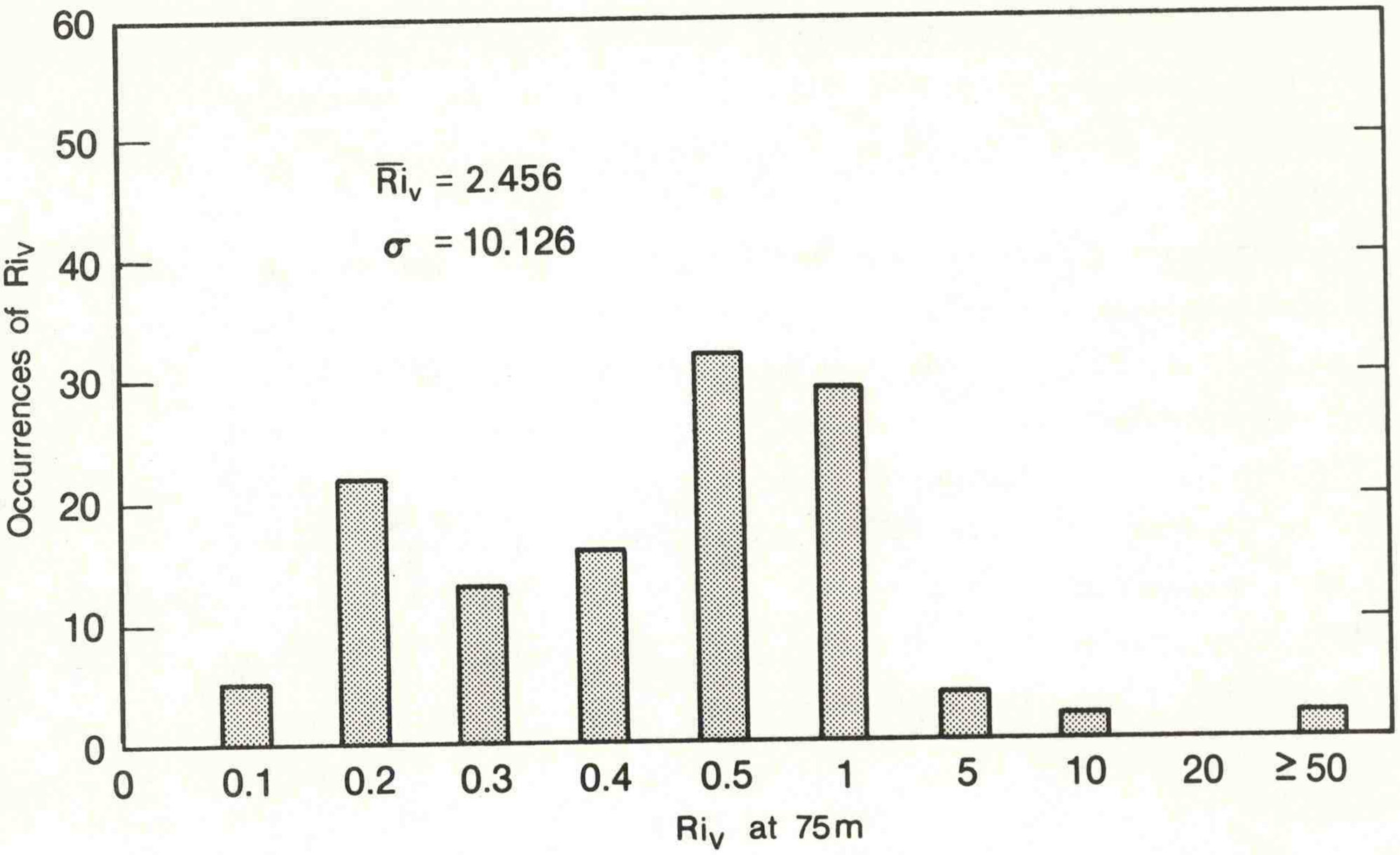


Figure 5.4.--Histogram of Ri_v at 75 m.

It was hoped that since an acoustic-gravity wave represents the response of the atmosphere to accelerations caused by deviations from geostrophic balance, one would observe a periodicity in Ri_v that would represent the attempt of the atmosphere to gain geostrophic balance by transfering momentum into the lower regions of the PBL through mechanical turbulence. Since the gradient Richardson number relates the mean field gradients of temperature and velocity to the dynamic stability of the atmosphere and the onset of mechanical turbulence, any changes in the mean fields of velocity and temperature should be reflected in the turbulence distribution (Neff, 1980).

As the wave propagates through the tower, parcels of differing θ_v will alternately move past the sensors, and thus $\partial\theta_v/\partial z$ should vary with the frequency of the wave. Since the vertical momentum distribution is changing,

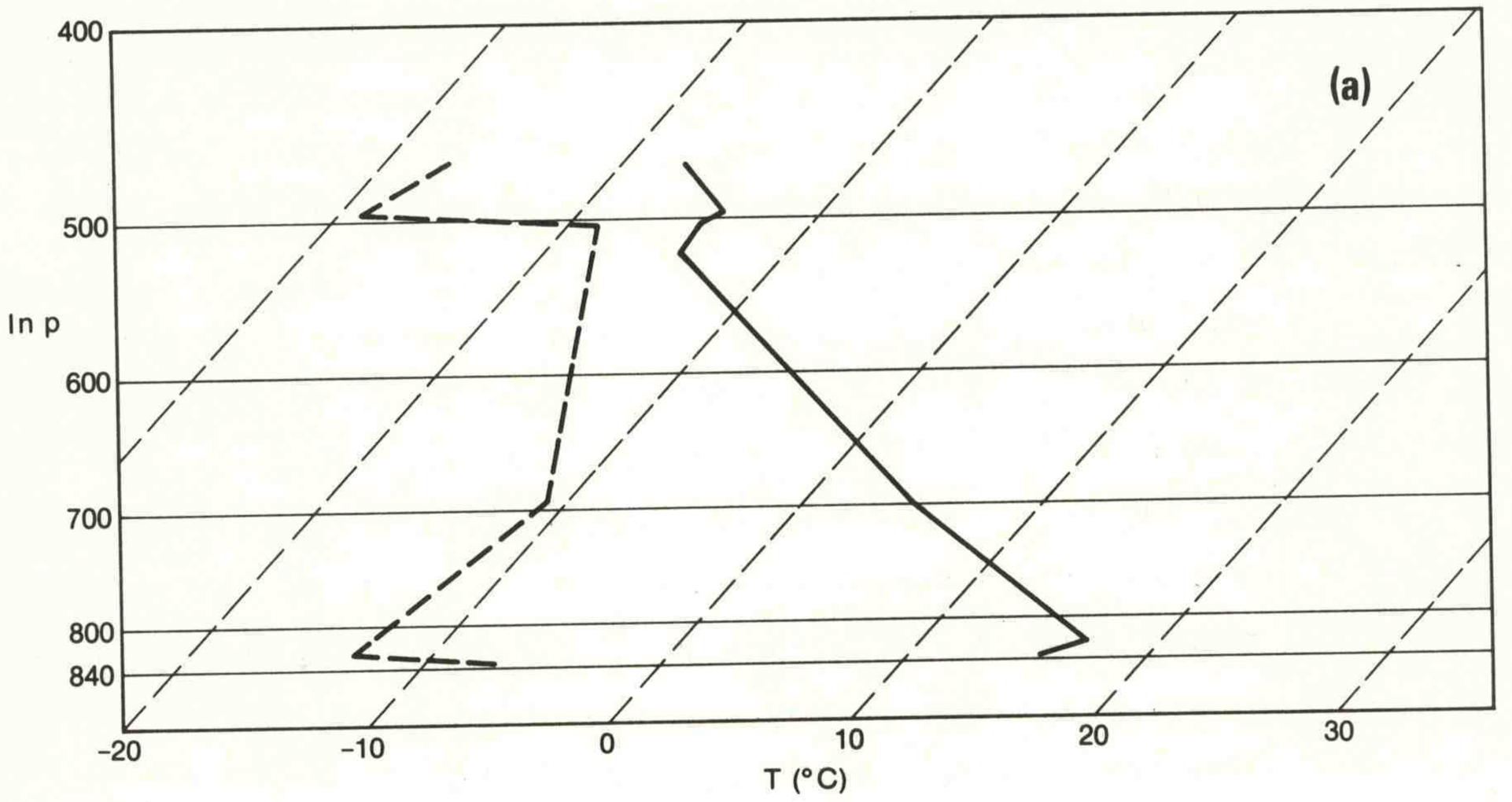
continuity requires that the horizontal momentum distribution must also change. Thus, not only should $\partial\theta_v/\partial z$ vary with time, but also $(\partial\vec{U}/\partial z)^2$ must vary. Also, $\partial p/\partial t$, at the ground, should reflect the wave propagation.

The evening of 6 November and early morning of 7 November are characterized by moderate static stability as shown by the National Weather Service soundings taken at Stapleton Airport near Denver, Colo. (Fig. 5.5). In addition the evening wind observation (Fig. 5.6) shows a weak shear zone in the lower kilometer of the atmosphere with the peak wind of 3 m/s at 200 m dropping off to less than 0.5 m/s at 800 m. Although these conditions are not particularly strong, the basic conditions for shear-generated instability are concluded to be present. The distance from the upper-air observation and the tower might also reduce the representativeness of the rawinsonde observations.

Figure 5.7 shows the time series of Ri_v, $\partial p/\partial t$, $(\partial\vec{U}/\partial z)^2$, and N_v^2. The time series of $\partial p/\partial t$ documents the wave activity well, and the acoustic sounder records in Figs. 5.8a,b provide another look at the height distribution of the wave activity.

Yet the only clear evidence of wave propagation in the Richardson number begins at 2220 and ends at 2330 MST. It is interesting to note that whereas the shear term $(\partial\vec{U}/\partial z)^2$ appears to be modulated by the wave, the N_v^2 term does not. It appears that the dominant factor in Richardson number reduction is the wind shear. Further investigation by decomposing the shear into its azimuthal and speed parts (Fig. 5.9) and comparing with Ri, shows that early in the evening the azimuthal shear is large and seeks to drive the Richardson number lower (Fig. 5.10). Later, after the Richardson number falls below 0.25, the speed shear increases.

If we assume that the onset of turbulence begins at $Ri < 0.25$, then the increase in wind speed might be a result of the momentum transfer into the lower boundary layer by the turbulence, while the azimuthal shear reflects the ageostrophic conditions that created the imbalance.



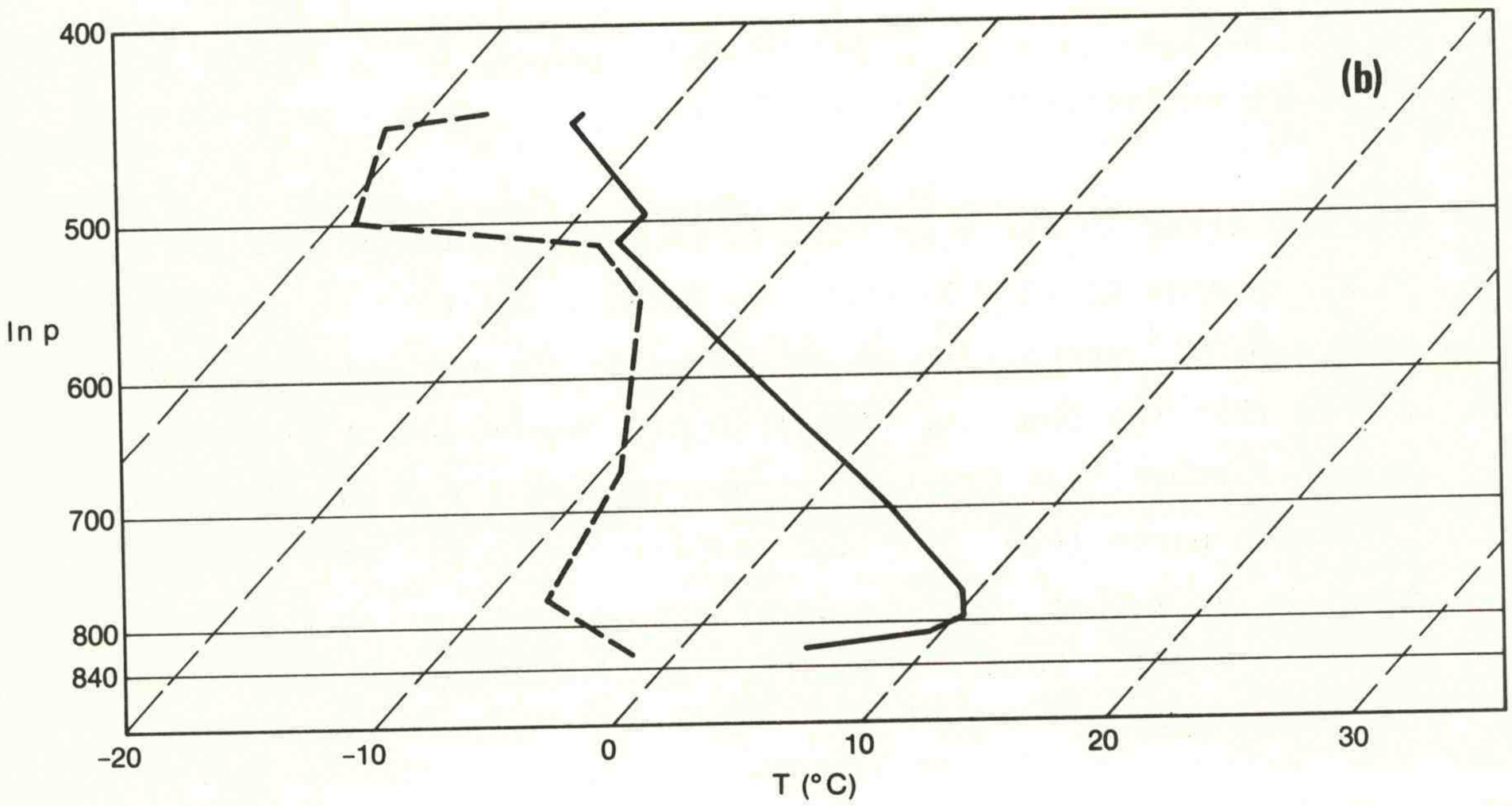


Figure 5.5.--Rawinsonde observations taken by the National Weather Service at Stapleton Airport, Denver, Colo., at (a) 1700 MST, 6 November 1981, and (b) 0500 MST, 7 November 1981.

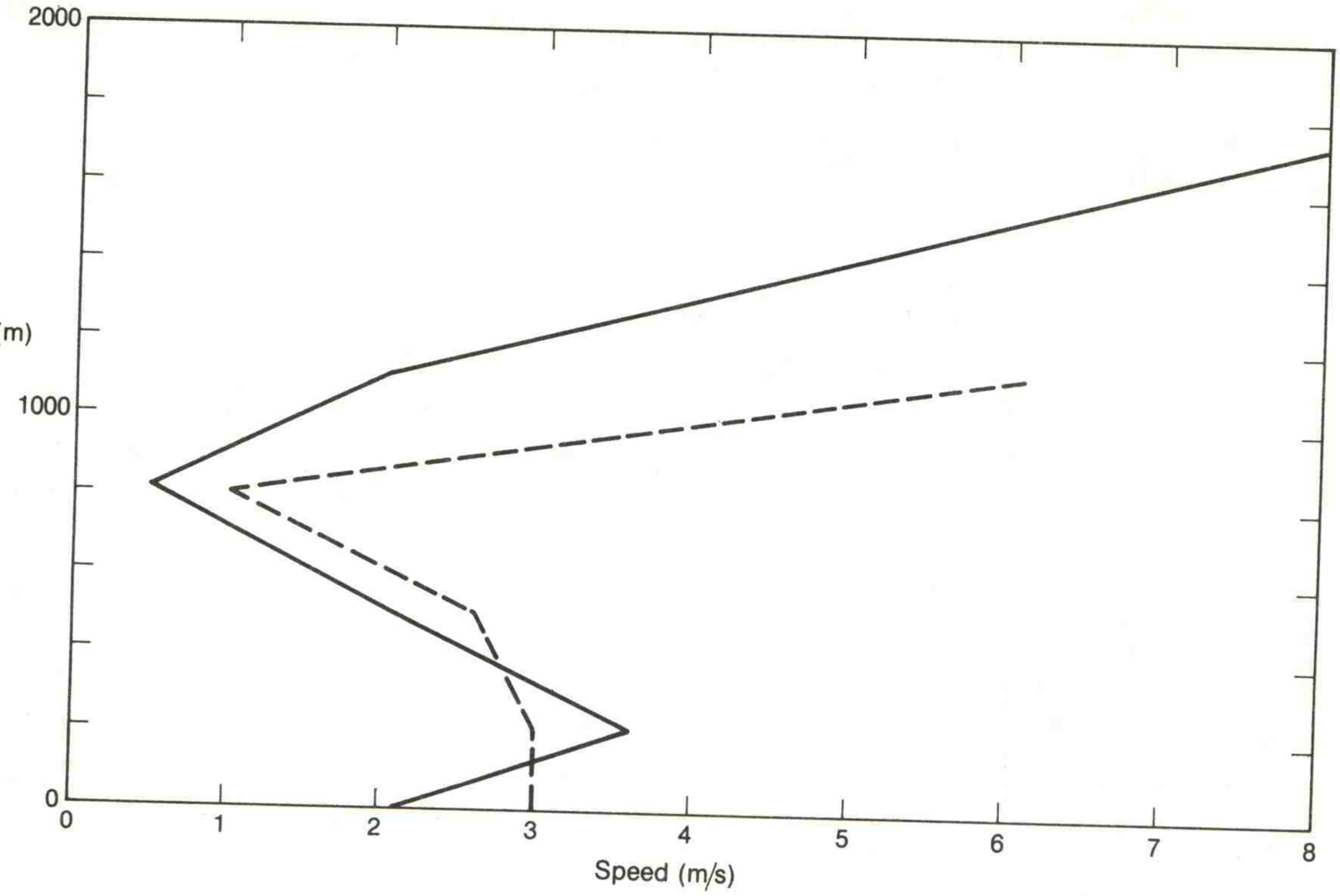


Figure 5.6.--Wind speed vs. height for rawinsonde observations at 1700 MST, 6 November 1981 (solid line), and 0500 MST, 7 November 1981 (dashed line).

The lack of modulation in N_v^2 might be an instrumentation problem. During calibrations the slow-response temperature probes were found to respond at differing rates to changes in ambient air temperature. This will result in smoothing the potential temperature gradient. The poor correlation between $\partial p/\partial t$ and Ri_v could be due to this factor. But the overall behavior of Ri_v through the period shows evidence that it can be tied to the inertial oscillations of the wind (Dutton, 1976) on a much longer period than that of acoustic-gravity waves (Fig. 5.10).

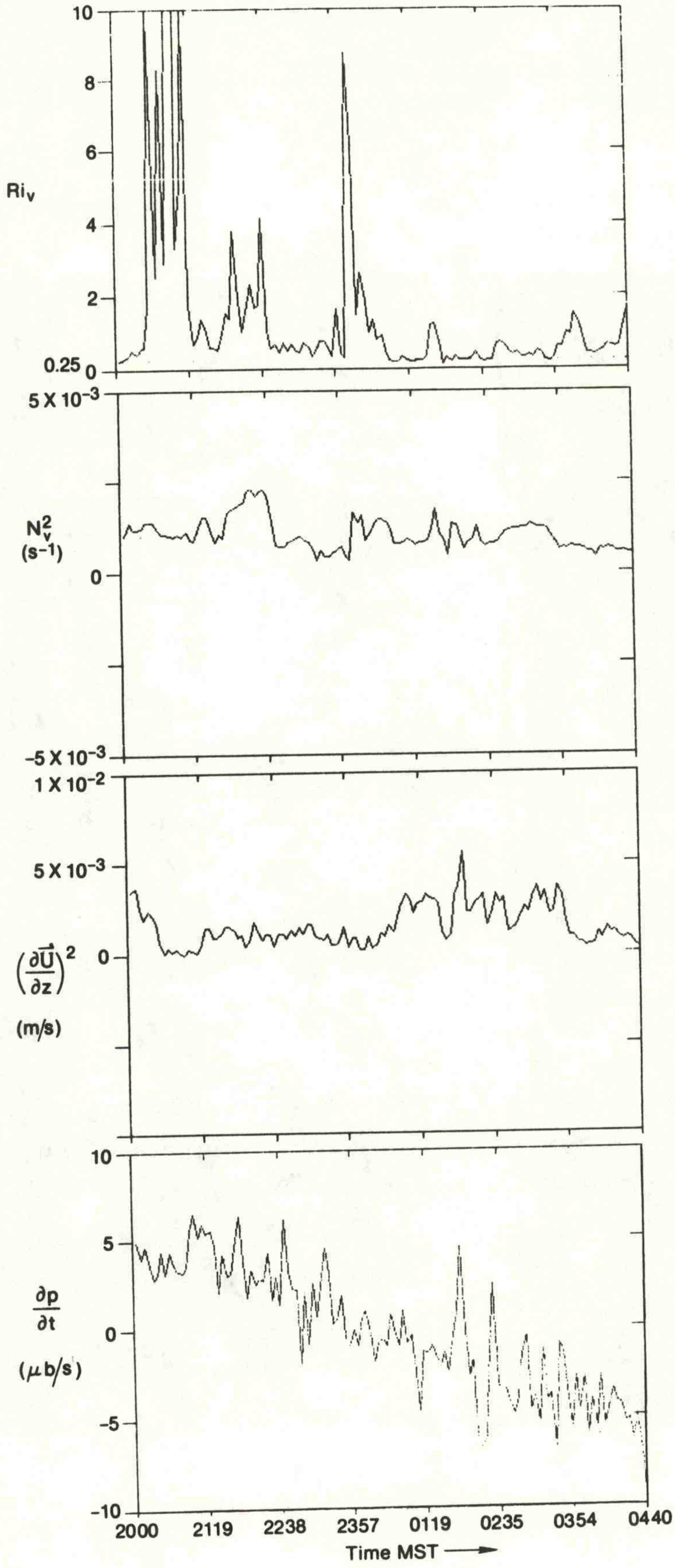


Figure 5.7.--Time series of Ri_v, N_v^2, and $(\partial \vec{U}/\partial z)^2$ at 75 m, and $\partial p/\partial t$ measured at the ground.

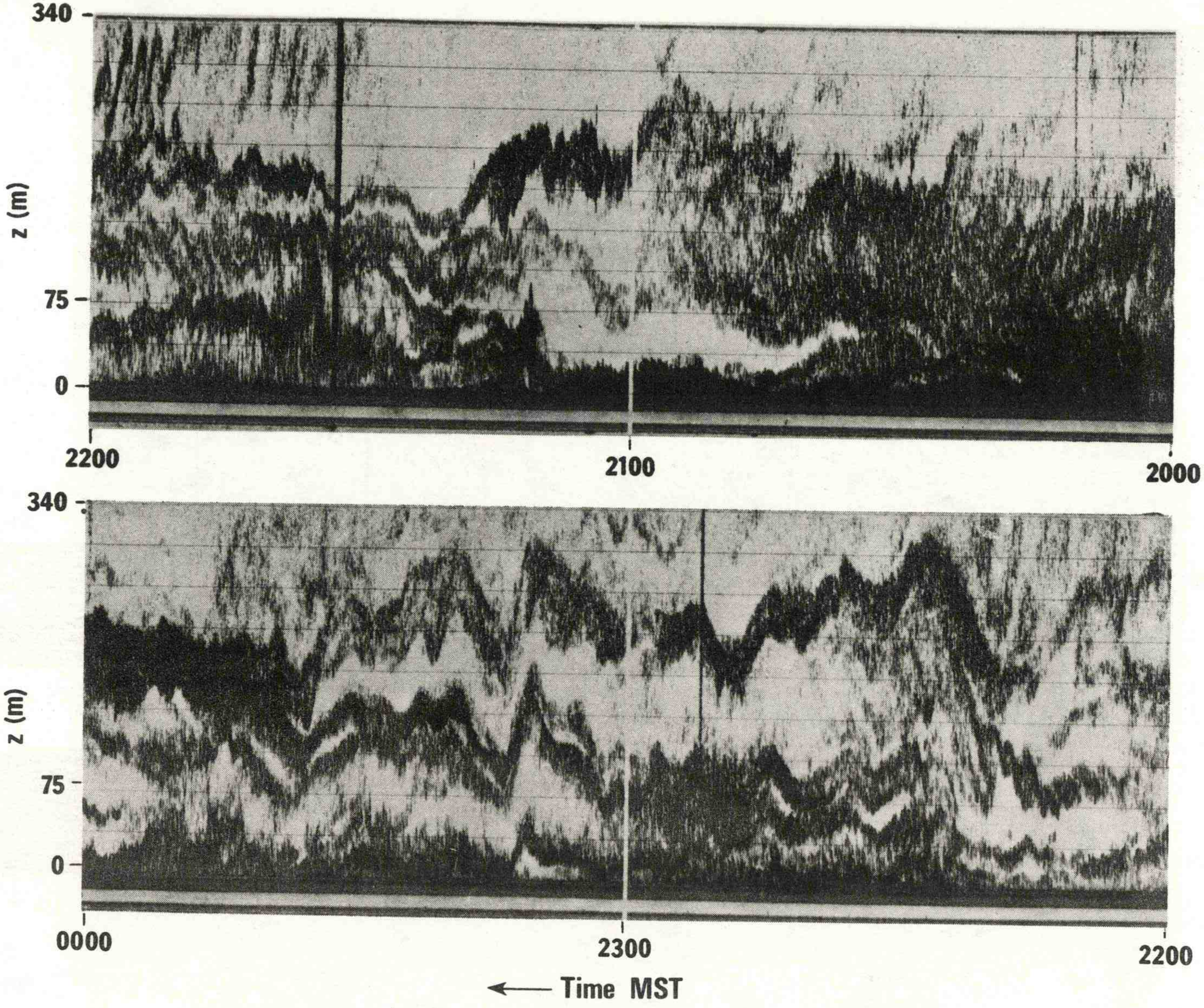


Figure 5.8a.--Acoustic sounder record beginning at 2000 MST, 6 November 1981.

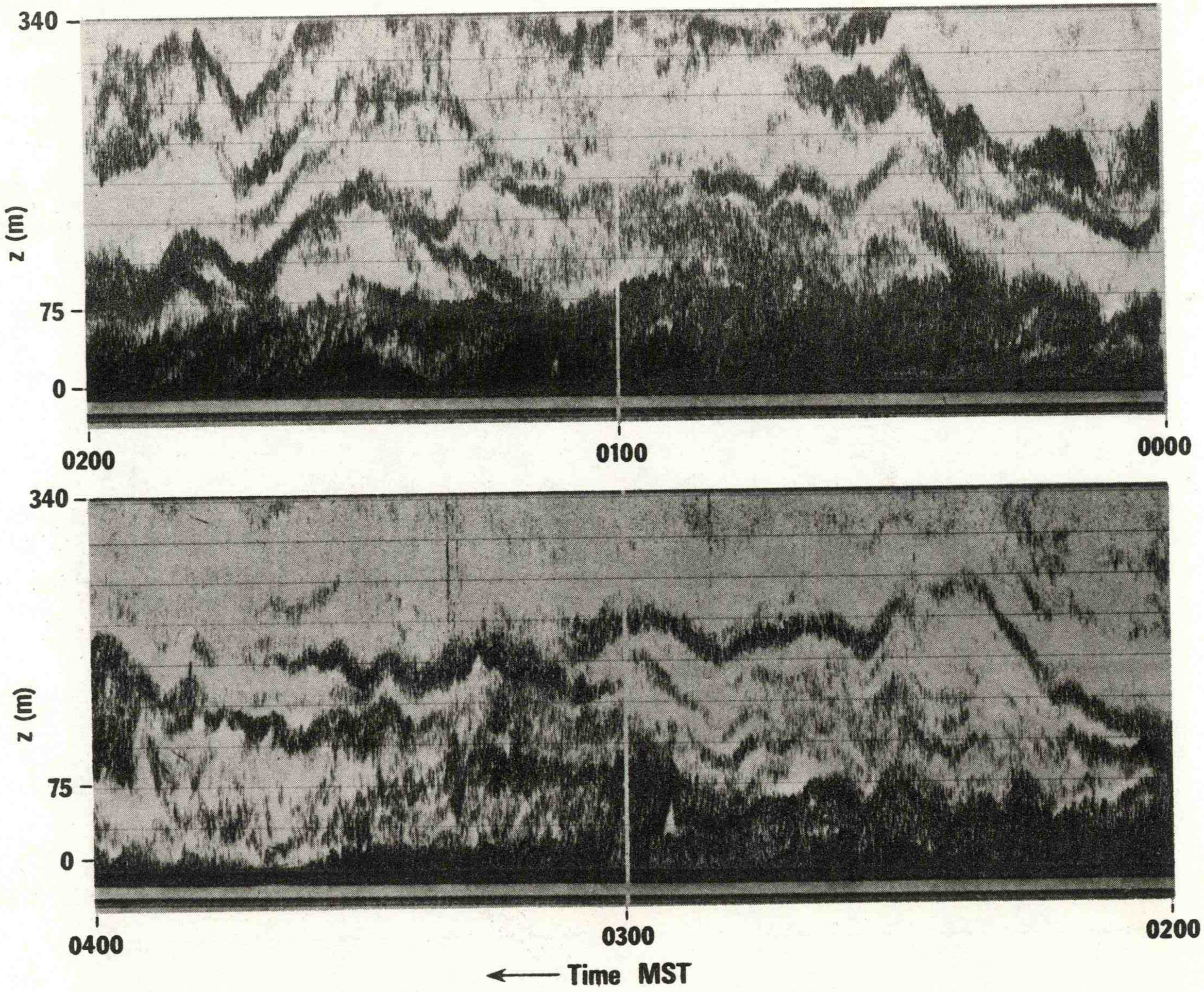


Figure 5.8b.--Acoustic sounder record beginning at 0000 MST, 7 November 1981.

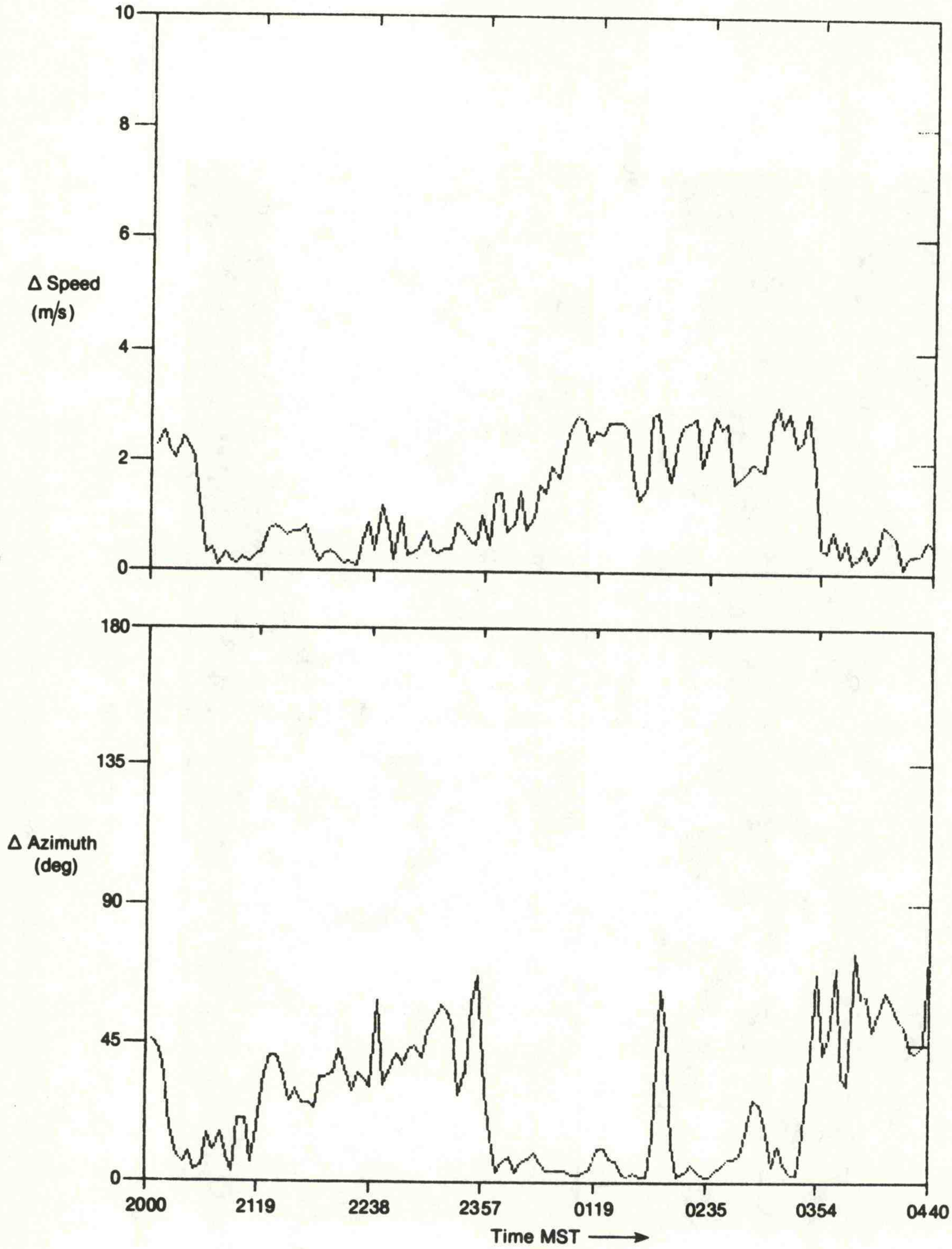


Figure 5.9.--Δ azimuth and Δ speed over the 50- to 100-m level of the tower.

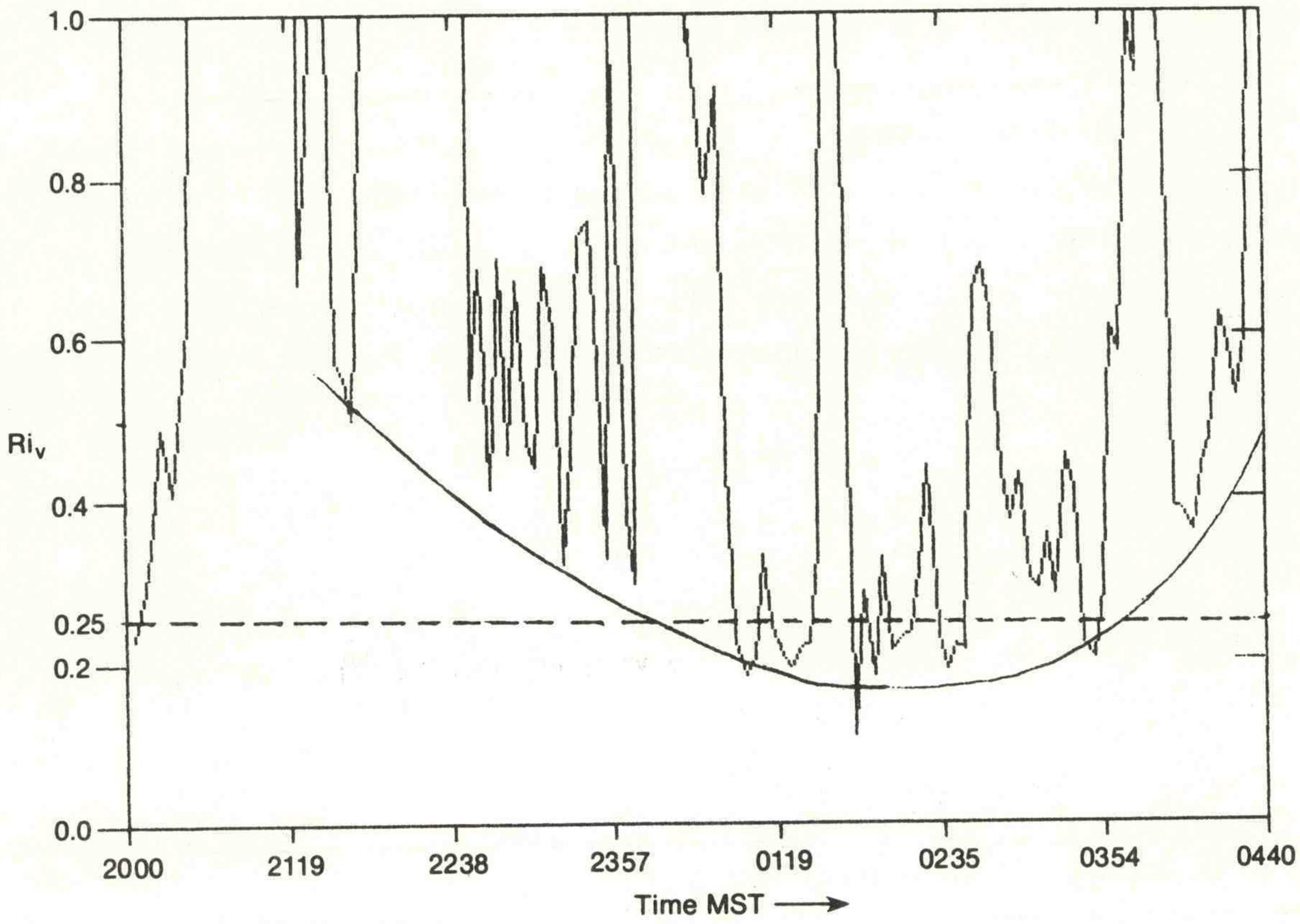


Figure 5.10.--Time series of Ri_v on an expanded scale showing long-period oscillation about the critical Richardson number.

5.6 CONCLUSIONS

The ability to calculate the gradient Richardson number using data from a boundary layer tower is demonstrated. It is concluded that the shear term plays an important role in the magnitude of the Richardson number and is in fact modulated by wave activity. It is also shown that the behavior of the shear term and the magnitude of Ri_v could be a result of inertial oscillations in the wind field in addition to higher frequency wave activity.

5.7 ACKNOWLEDGMENTS

The author wishes to thank J.E. Gaynor, E.E. Gossard, and W.D. Neff for their guidance, patience, and criticism during the preparation of this work and the creation and debugging of the software. I would also like to thank J. Hart for her help in the software effort, the BAO tower crew, J. Newman and N. Szczepczynski, who provided me with their expert knowledge of the instrumentation.

5.8 REFERENCES

Chimonas, G., 1970: The extension of the Miles-Howard theorem to compressible fluids. J. Fluid Mech., 43, 833-836.

Dutton, J., 1976: The Ceaseless Wind--An Introduction to the Theory of Atmospheric Motion. McGraw-Hill, New York, 579 pp.

Fleagle, R.G., and J.A. Businger, 1980: An Introduction to Atmospheric Physics, 2nd ed. Academic Press, New York, 432 pp.

Gossard, E.E., and W.H. Hooke, 1975: Waves in the Atmosphere, Atmospheric Infrasound and Gravity Waves--Their Generation and Propagation. Elsevier, New York, 442 pp.

Hess, S.L., 1959: Introduction to Dynamic Meteorology. Holt, Rinehart and Winston, New York, 362 pp.

Howard, L.N., 1961: Note on a paper of J.W. Miles. J. Fluid Mech., 10, 509-512.

Kaimal, J.C., and J.E. Gaynor, 1983: The Boulder Atmospheric Observatory. J. Clim. Appl. Meteorol. (accepted).

Lalas, D.P., and F. Einaudi, 1973: On the stability of a moist atmosphere in the presence of a background wind. J. Atmos. Sci., 30, 795-800.

Miles, J.W., 1961: On the stability of heterogeneous shear flows. J. Fluid Mech., 10, 496-508.

Murray, F.W., 1967: On the computation of saturation vapor pressure. J. Appl. Meteorol., 6, 203-204.

Neff, W.D., 1980: An observational and numerical study of the atmospheric boundary layer overlying the east Antarctic ice sheet. Ph.D. Thesis, University of Colorado, Boulder, Colo., 272 pp.

☆ U.S. Government Printing Office 1983 - 676-001/1216 Reg. 8

NOAA CENTRAL LIBRARY
CIRC QC851 .B6 no.4
Studies of nocturnal stabl
3 8398 0004 0904 9

DEPARTMENT OF COMMERCE • UNITED STATES

BAO

BAO